DOCTOR OF PHILOSOPHY

Thermocline Mixing in a Seasonally Stratified Shelf Sea

Lincoln, Ben

Award date:
2012

Awarding institution:
Bangor University

Thermocline Mixing in a Seasonally Stratified Shelf Sea

Author:

Ben Lincoln

Supervisors:

Dr. Tom Rippeth

Professor. John Simpson

Dr. Mattias Green

Ph.D. 2012

Abstract

Vertical mixing at the thermocline determines transport pathways for heat, nutrients and carbon dioxide, which are crucial to ecosystems and to the Earths climate. Current models are unable to predict the correct levels of mixing in the thermocline region, falling short by orders of magnitude. This thesis examines two candidates for this anomalous internal mixing; inertial shear spikes driven by wind stress and internal waves generated by tidal currents interacting with underwater topography.

50 days of vertical current and temperature measurements were made in the Western Irish Sea in spring and early summer are complemented by a 48 hour time series of turbulent dissipation. Inertial currents generated by strong winds were observed in the surface mixed layer with magnitudes of over 0.3ms^{-1}, while internal tidal currents of 0.1ms^{-1} were observed at spring tides. Analysis of the bulk shear vector revealed that the frequency of the shear rotation switched many times during the observations depending on wind and tidal forcing.

When wind stress was high, inertial shear spikes were observed, with maximum shear production occurring when the bulk shear vector and wind vector aligned. Maximum shear resulted 3.75 hours later when the surface motion was at 90° to the right of the wind direction. Inertial shear spikes were the most energetic baroclinic process but were found not responsible for the anomalous thermocline mixing because their dynamics were well reproduced by a 1D turbulence closure model and because of to the way in which they modified the vertical temperature structure. High vertical resolution observations showed that the spikes driven by the wind generated sufficient shear to reduce the gradient Richardson number below one quarter and sustain mixing at the base of the surface mixed layer. Each spike generated instabilities which eroded the top of the thermocline, deepening the mixed layer in a series of steps until the buoyancy frequency increased sufficiently to suppress mixing.

The observations of the nature of the internal tidal revealed that it evolved from a distinct mode 1 structure to a vertical structure with mode 2 characteristics. The mode 1 internal tide was found to have an energy flux of 34Wm^{-1} which was insufficient to account for the 1mWm^{-2} of dissipation which was observed in the thermocline region. However one third of this energy was found to come from the passage of a packet of non-linear internal waves. These waves generated strong shear and drove instabilities in the centre of the thermocline, elevating dissipation rates to $\varepsilon_{\text{th}} = 1 \times 10^{-2}\text{mWm}^{-3}$ which was up to 3 orders of magnitude higher than the background level of $\varepsilon_{\text{th}} = 1 \times 10^{-5}\text{mWm}^{-3}$.

The transition from 2 layer to 3 layer during a period of internal tidal activity lead to the hypothesis that the diffusion of the thermocline could be used to quantify internal mixing rates. Based on observations of vertical temperature structure an internal mixing parameter $\Delta\Phi$ was developed to quantify the thermocline diffusion. $\Delta\Phi$ revealed that in the Irish Sea more energy was required to cause the thermocline diffusion than was directly measured. A simple mixing model revealed that the this was due to heat input at the surface combined with low wind stress. $\Delta\Phi$ proved more useful when applied to spatial datasets where dissipation rates were higher, leading to a quantification of the level of internal mixing with distance from the Celtic Sea shelf break. Replicating this spatial signal in $\Delta\Phi$ using the internal mixing model required an energy flux of $400\mathrm{Wm}^{-1}$ and an e-folding scale of 50km.

Acknowledgements

Firstly and above all I must thank my main supervisor Dr Tom Rippeth who has given me so many opportunities that I would never have had if it wasn't for him. Research expeditions to the Arctic Ocean on Russian and Canadian icebreakers are experiences that I could never have foreseen when I came to Bangor to do the masters course over 6 years ago. His passion for climate change research and doing "proper science" is a constant reminder that the work we do is for the good of everyone (except bankers and oil company executives). Professor John Simpson has always been prepared to listen to not only the bigger picture but the important minutiae of my research, his ability to cut straight to the important points of an argument or problem is a testament to his knowledge and experience, both of which have been invaluable. His anecdotes of oceanographic experiences from the past have been great source of interest to me and set our field in a fascinating historical perspective. Dr Mattias Green has been a vital source of technical knowledge saving me many hours of head scratching. His optimism has helped me believe in the direction I was headed and I thank him particularly help with the internal wave work and internal mixing parameterisation.

My supervisory committee, Professor Alan Davies and Professor Dave Bowers have been friendly faces since I arrived at Bangor and I would like to thank them for assisting me with advice about the practicalities of achieving my PhD. I am grateful to the Bangor technical staff and the crew of the RV Prince Madog without whom I could never have collected such an interesting dataset - in particular I would like to thank Ben Powell who I have spent more time together the last 4 years than either he or I would have chosen. Much of this time has been cold uncivilised hours on the deck of various ships in "the arse end of nowhere". He has always done a good job, both on deck and in the bar. Dr Jonathan Sharples has always been very quick to help me by providing Met-Office wind data when our measurements failed, this wind data was crucial to my PhD. I must also thank all my colleagues at the school of Ocean Sciences, and in particular Yueng, Chris and Tasha, whose enthusiasm and knowledge have made Bangor a pleasant place to work. I must also thank the National Environmental Research Council for funding me through my PhD.

I would like to thank the great people I have met in North Wales for their help in making this a great place to study. While I cannot name all the fun people who I have shared this green and intermittently pleasant land I must name my housemates with whom I have shared both the joy and the pain of PhD life. Eilir and I started and finished the PhD together in fine style I can only say, "School Running's". I have many great memories from my student house, Angorfa, which was a messy but comfortable

home for many years and enjoyed by some playful, and at times oddly dressed, individuals especially, Oli, Rosie, Gwladys, Jen, Seb and honorary housemates, Sholto and Callum. Matt Toberman has been a good friend and great enthusiast of Physics, and has always been there to appreciate an interesting feature or a tricky problem. His interest in the process as much as the end result has been both a blessing and a curse! I am also grateful for the welcome I get from my oldest friends back home when I infrequently return, despite my forsaking them for this faraway foreign land.

My family deserves the greatest thanks for giving me the love and support that has allowed me to go to university and study into my 30s. My grandparents Edna and Fred were always very proud and supportive. While my Granny Barbara was always so interested in everything I did and it is a shame that she did not live to hear my tales of the ocean. My sister Josie is always a great voice of reason and her positivity and light-hearted nature always put any problems in perspective. My parents have helped me in the challenge from the start, from my scrambled application for the Masters course to supporting my purchase of a damp Welsh cottage. They have always been keen to visit me here and their appreciation for my work, even though they are not quite sure what I do, is very much appreciated. Lastly and most importantly I must thank Harriet for her eternal patience and support. She is always full of smiles, hugs and kind words, even through the most difficult times. Her delightful company has helped me throughout my PhD and for this I am eternally grateful. She has only ever known me as a student; I hope she likes me as Doctor!

Contents

List of figures

List of symbols used

$u\ v\ w$ = easterly, northerly and vertical velocity components, (ms^{-1})

$U\ V\ W$ = mean velocity components, (ms^{-1})

$u'\ v'\ w'$ = fluctuating (turbulent) velocity components, (ms^{-1})

$V_{btt}\ U_{btt}$ = northerly and easterly barotropic tidal velocity, (ms^{-1})

$v_{bt}\ u_{bt}$ = northerly and easterly barotropic velocity, (ms^{-1})

U_{bt} = modulus of barotropic velocity, (ms^{-1})

$v_t\ u_t$ = northerly and easterly baroclinic tidal velocity, (ms^{-1})

$v_i\ u_i$ = northerly and easterly barotropic inertial velocity, (ms^{-1})

$c_v\ c_u$ = northerly and easterly residual velocity components, (ms^{-1})

E_T = turbulent kinetic energy, (J)

u_{ts} = tidal stream velocity, (ms^{-1})

h = height of water column, (m)

z = distance below surface, (m)

Φ = the potential energy anomaly, (Jm^{-3})

Φ_{obs} = the potential energy anomaly, (Jm^{-3})

Φ_{2layer} = the potential energy anomaly of a heat balanced equivalent two layer temperature structure, (Jm^{-3})

$\Delta\Phi$ = internal mixing parameter, (Jm^{-2})

ρ = density, (kgm^{-3})

$\hat{\rho}$ = depth mean density, (kgm^{-3})

$\tau_{xz}\ \tau_{yz}$ = Reynolds stresses, (Pa)

N_z = eddy viscosity, (m^2s^{-1})

K_z = eddy diffusivity, ($m^2 s^{-1}$)

P = production of turbulent kinetic energy, (Wm^{-3})

B = buoyancy production (rate of mixing water column), (Wm^{-3})

ε = dissipation rate of turbulent kinetic energy, (Wm^{-3})

ε_{th} = thermocline integrated dissipation rate, (Wm^{-3})

ε_s = surface mixed layer integrated dissipation rate, (Wm^{-3})

Γ = mixing efficiency

N^2 = buoyancy frequency, (s^{-1})

S^2 = velocity shear squared, (s^{-2})

Φ_{KE} = spectral kinetic energy function, (J/cpm)

k = wavenumber, (m^{-1})

Pr = horizontal pressure gradient, (Pam^{-1})

f = Coriolis parameter, (s^{-1})

F_{Cx} F_{Cy} = components of coriolis force, (N)

Ω = rate of rotation of the earth, ($rads^{-1}$)

ϕ_L = latitude, ($^\circ$)

T = period, (hours)

u_s v_s = surface layer velocity components, (ms^{-1})

u_b v_b = bottom layer velocity components, (ms^{-1})

Sb = bulk shear, (s^{-1})

S_{BR} = bulk shear - Burchard & Rippeth defined, (s^{-1})

h_s = thickness of surface layer, (m)

h_s = thickness of bottom layer, (m)

W_z = wind speed at height z, (ms^{-1})

W_* = wind friction velocity, (ms^{-1})

τ_s = surface (wind) stress, (Pa)

τ_b = bottom (bed) stress, (Pa)

W_{10} = wind speed at height of 10m, (ms^{-1})

C_D = wind stress drag coefficient

Q = heat content, (J)

c_p = specific heat capacity, (Jm^{-3})

$T(z)$ = temperature at depth z, (°C)

C_{Db} = bottom stress drag coefficient

τ_{bx} τ_{by} = bed stress components

E_{vol} = internal wave energy per unit volume, (Jm^{-3})

w_{IW} = vertical velocity perturbation due to internal waves, (m)

u_{IW} = horizontal velocity perturbation due to internal waves, (ms^{-1})

η = vertical displacement of a streamline/isotherm, (m)

u_{fit}, v_{fit} = least squares fits to easterly and northerly velocity components, (ms^{-1})

Ψ = the complex amplitude of the vertical velocity from normal mode analysis

c_p = internal wave phase speed, (ms^{-1})

c_g = internal wave group speed, (ms^{-1})

c_n = phase speed of mode n internal wave from normal mode analysis, (ms^{-1})

u_n = horizontal velocity modal structure of mode n internal wave from normal mode analysis

Chapter 1

Introduction

1.1 Background and motivation for the study

The worlds rainforests are often referred to as the lungs of the Earth, however the worlds Oceans are thought to be at least as important as forests for both the production of oxygen and the absorption of carbon dioxide from the Earths atmosphere. The importance of the continental shelf seas within this function is much greater than their size may suggest. Although only 7.6% of the world's ocean surface is made up of shelf seas, these contribute significantly, 20-50%, to the total carbon dioxide storage [Tsunogai et al., 1999; Thomas et al., 2004].

The importance of shelf seas in the carbon cycle is partly due to the high biological activity that results from high nutrient availability and their efficient use. The availability of nutrients in shelf seas is controlled by a seasonal cycle of stratification which determines the growth of phytoplankton and therefore primary production. The onset of stratification in spring triggers the spring bloom as it stabilises the water column with warmer water sitting over dense colder water.

Dividing these layers is a region of strong vertical temperature gradient known as the seasonal thermocline. This thermocline acts to suppress vertical mixing and by retaining phytoplankton in the surface layer provides favourable conditions for growth [Sverdrup, 1953]. These blooms are impressive biological events rapidly producing one third to one half the primary production in shelf seas [Townsend et al., 1994]. However they are relatively short lived, lasting days to weeks. Once the surface layer nutrients are used up, further growth is then dependent on the vertical or horizontal flux of nutrients into the stratified euphotic zone from mixed waters below the thermocline, or across a front. The physical processes that drive these exchanges determine the productivity through the long summer stratified period.

Horizontal advection and mixing occurs at the boundaries between stratified and fully mixed regions.

These tidal mixing fronts are regions of intense biological activity and were the subject of early work into Shelf Sea mixing and primary production [Simpson, 1981]. These frontal regions though productive are limited in their spatial extent to bands several kilometres wide along the boundaries of the stratified regions. The stratified regions themselves occupy a much larger area than the frontal zones, but during summer months little primary production is observed at the surface. This is because new production is dependent on the flux of nutrients into the surface mixed layer from below the thermocline. For this reason primary production is often observed to be highest in the thermocline region, with numerous measurements showing enhanced chlorophyll concentration at the pycnocline (Anderson 1969, Sharples et al 2001). This feature has been termed the subsurface chlorophyll maximum (SCM) and can be seen in data from the English Channel plotted in figure 1.1. Concentrations of chlorophyll in the SCM are modest ($\sim 26 \mathrm{mgm}^{-3}$, Sharples et al. 2001) and the layer relatively thin in comparison to the spring bloom (5-20m). However the longer duration of the SCM means it has been estimated to be at least as significant in terms of primary production and carbon fixation as the spring bloom [Richardson, 2000].

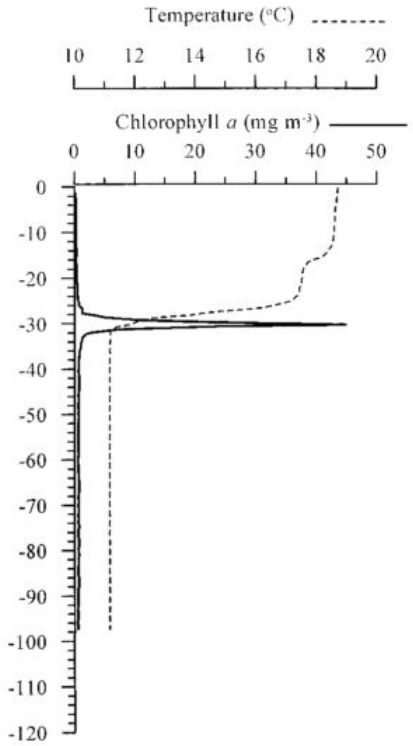

Figure 1.1: Temperature and chlorophyll concentration showing the SCM (subsurface chlorophyll maxima) in the Western English Channel Sharples et al. [2001]

Vertical mixing across the thermocline facilitates the diapycnal flux of nutrients to the euphotic zone and thus determines the primary production. These vertical mixing processes also dictate the effectiveness of CO_2 draw-down by shelf seas by a process known as the "Shelf Sea Pumping" which transfers of atmospheric CO_2 to the open ocean [Tsunogai et al., 1999]. Extrapolation of CO_2 measurements from transects in the East China Sea and North Sea to all shelf seas suggested that they may account for 50%-20% the CO_2 absorbed by the ocean [Tsunogai et al., 1999; Thomas et al., 2004].
Climate change has become a key scientific and political issue. With shelf seas playing an important role in the absorption of anthropogenic CO_2 understanding and modelling vertical mixing processes poses a key challenge if we are to predict future changes and responses.

1.2 Vertical structure in shelf seas

During summer months the shelf seas are divided into stratified and well mixed regions divided by frontal zones which comprise horizontal gradients of up to 1°C per km [Simpson and Hunter, 1974]. An example of this can be seen in figure 1.2a, where stratified regions are indicated by higher sea surface temperatures during summer. A balance between the input of solar heat at the surface and turbulent mixing determines the vertical structure and stratification of the water column. Turbulent energy is generated by tidal stresses at the sea bed and to a lesser extent by wind stress on the sea surface. This competition between the input of buoyancy and de-stratifying mixing processes became well established during the 70s and 80s in terms of vertical exchange processes ([Simpson and Hunter, 1974; Garrett et al., 1978].
The criterion of h/u_{ts}^3 developed by Simpson and Hunter [1974] was a breakthrough in understanding because it proved effective in positioning the transition from stratified to mixed regimes in terms of the tidal stream velocity, u_{ts}, and the depth h. Another useful tool in interpreting the vertical structure of shelf seas is a quantification of the strength of stratification developed by Simpson et al. [1977]; Simpson [1981]. The potential energy anomaly, Φ, is calculated from observations of the vertical density structure, and is defined as the amount of work per unit volume required to overcome buoyancy forces and fully mix the water column:

$$\Phi = \frac{1}{h}\int_{z=-h}^{0}(\rho(z)-\hat{\rho})gz.dz \tag{1.1}$$

Where h is the height of the water column, z is the vertical depth coordinate, $\rho(z)$ is the density at depth z, $\hat{\rho}$ is the depth mean density and g is the gravitational constant. Φ has been useful for quantifying stratification in a number of studies where stratification varies in space or time, e.g investigating

the position of tidal mixing fronts [Simpson, 1981], cycles of seasonal stratification [Simpson and Bowers, 1984], and tidal straining [Simpson et al., 1990].

The traditional boundary mixing theory describes competition between tidal mixing from the bed and wind mixing from the surface. Simpson and Bowers [1984] used this idea of inputting mixing energy at the boundaries in a simple model type of stratification which estimated the input of heat at the surface, and distributed this heat by evaluating the the input of tidally and wind mixing energy at the bed and surface respectively. The model was effective at reproducing the seasonal cycle of stratification. However the boundary mixing approach used in such models tends to generate a deep uniform bottom layer and a shallow uniform surface layer. This is contrary to observations of vertical temperature structure, e.g Rippeth [2005] presents measurements from a number of shelf sea locations, some of these do have two layers separated by a thin thermocline, however others are have a more diffuse thermocline which occupies a significant portion of the water column. This broad thermocline has been used as evidence for a source of mid-water mixing acting to diffuse the thermocline [Rippeth, 2005; Green et al., 2008].

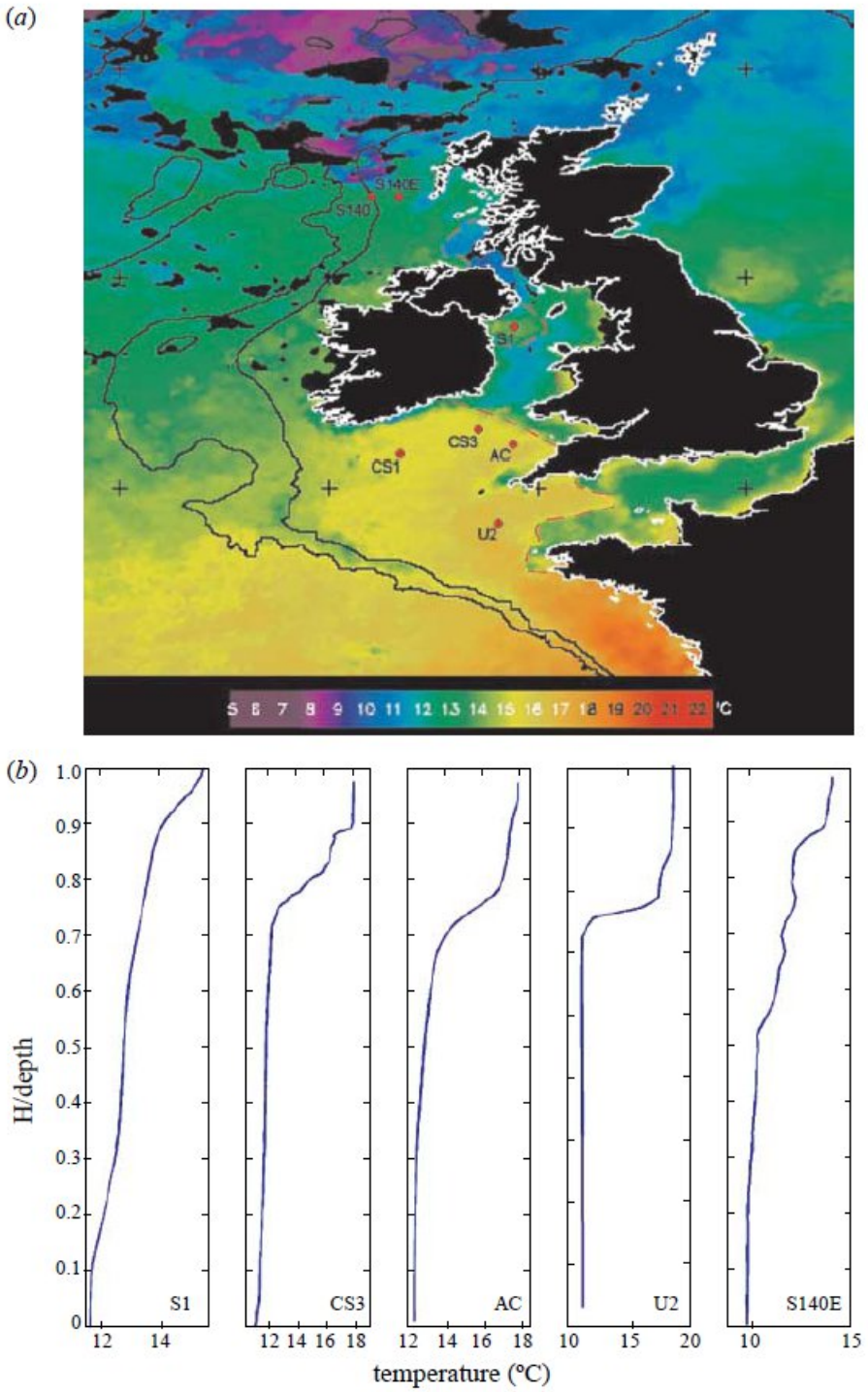

Figure 1.2: Examples of vertical temperature profiles from North West European shelf seas. a) Map of sea surface temperature during the summer across the north west European shelf seas with labels showing the positions of the temperature profiles plotted in pane b [Rippeth, 2005].

1.3 Turbulence theory

The random fluctuations in flow which we observe as eddies are part of a phenomenon known as turbulence which has challenged (and troubled) many great minds; Richard Feynman labeled turbulence the most important unsolved problem in classical physics! The random, strongly non-linear nature of turbulence has limited our understanding of turbulent processes with many theories semi-empirical in nature. Comprehensive accounts of turbulence in the ocean are available e.g. Thorpe [2009], while Simpson and Sharples [2012] present those aspects relevant to the shelf seas. The following sections contain only the fundamental theory relevant to the generation and dissipation of turbulence in the shelf sea seasonal thermocline.

1.3.1 Turbulent parameters

The velocity components u, v, w, can be expressed as the sum of a mean flow U, V, W, averaged over a selected period, and a fluctuating component u', v', w':

$$\begin{aligned} u &= U + u' \\ v &= V + v' \\ w &= W + w' \end{aligned} \tag{1.2}$$

The turbulent components, by definition, have a zero mean over the time period used to average the mean component. A quantification of the energy contained in turbulence, the turbulent kinetic energy (TKE), is defined using these turbulent components:

$$E_T = \frac{1}{2}(\overline{u'^2} + \overline{v'^2} + \overline{w'^2}) \tag{1.3}$$

1.3.2 Reynolds stresses

It is the turbulent components of velocity which are responsible for the turbulent diffusion transporting momentum as well as scaler properties. For example, the net flux of y momentum in the x direction, $\bar{F}$ is given by:

$$\bar{F} = \rho UV + \rho\overline{u'v'} \tag{1.4}$$

The second term describes the flux of momentum due to the covariance of the turbulent fluctuations u' and v'. The momentum transfer this describes is an internal stress component of which there are nine, which may be summerised in the Reynolds stress tensor (equation 1.5).

$$\rho \begin{pmatrix} \overline{u'u'} & \overline{u'v'} & \overline{u'w'} \\ \overline{v'u'} & \overline{v'v'} & \overline{v'w'} \\ \overline{w'u'} & \overline{w'v'} & \overline{w'w'} \end{pmatrix} \tag{1.5}$$

These are known as 'Reynolds' stresses and account for the transfer of three components of stress in three dimensions.

1.3.3 Eddy viscosity and eddy diffusivity

When studying vertical exchange processes we are interested in the Reynolds stresses (equation 1.5) responsible for the vertical diffusion of horizontal momentum:

$$\tau_{xz} = \rho\overline{u'w'}; \quad \tau_{yz} = \rho\overline{v'w'} \tag{1.6}$$

However our knowledge of how the fluctuating components relate to the mean flow is limited so oceanographers use an analogy to viscous stresses by defining an eddy viscosity N_z which is analogous to a fluids molecular viscosity.

$$\tau_{xz} = \rho N_z \frac{\delta U}{\delta z}; \quad \tau_{yz} = \rho N_z \frac{\delta V}{\delta z} \tag{1.7}$$

The molecular viscosity of a fluid describes the transfer of momentum through molecular collisions and is orders of magnitude smaller than a typical eddy viscosity and so operates much less efficiently. The action of turbulence also dominates the transfer of tracers such as heat, salt and nutrients. The turbulent eddies separate and disperse particles mixing them but also sharpen gradients and increase the surface area available for molecular diffusion to act. The vertical transfer of scalars is therefore treated in a similar way to momentum with an eddy diffusivity, K_z, defined as a rate of diffusion of tracers.

In a steady state equilibrium ($\delta E_T / \delta t = 0$), where convection is absent, there is an assumed balance known as *local equilibrium* in which the production of TKE by shear stresses (P) is balanced by the sum of the rate of mixing of the water column (B) and the rate of dissipation of TKE to heat (ε):

$$\begin{aligned} P &= B + \varepsilon \\ N_z \left(\left(\frac{dU}{dz} \right)^2 + \left(\frac{dV}{dz} \right)^2 \right) &= \frac{K_z g}{\rho_0} \frac{d\bar{\rho}}{dz} + \varepsilon \end{aligned} \tag{1.8}$$

From this assumption an important relation was developed [Osborn, 1980] to estimate the eddy diffusivity from measurements of the dissipation rate of TKE.

$$K_z = \Gamma\left(\frac{\varepsilon}{N^2}\right) \tag{1.9}$$

Where N is the buoyancy frequency (equation 1.10) and Γ is an efficiency factor which determines the rate of conversion of TKE to water-column potential energy through vertical mixing. The theoretical value obtained by Osborn [1980], $\Gamma = 0.2$, is widely assumed, however this is likely to be an upper limit. Osborn [1980] presents results from empirical studies of the ratio $\Delta PE/\Delta KE$ which show 10-25% of the energy efficiency in mixing. Studies in the field estimate that a relatively small proportion of the energy contained in the barotropic tide is available to increase the water column PE, $\Gamma = 0.0037$ [Simpson et al., 1978]. However barotropic tidal currents generate TKE fairly close to the bed and so may not be expected to be effective in mixing in the mid-water region where stratification occurs. Internal waves, propagating at the thermocline in the basin of fjords, were found to be much more effective in a study where, $\Gamma = 0.056$ [Stigebrandt and Aure, 1989].

1.3.4 Gradient Richardson Number

As discussed previously, sheared flow ($S = du/dz$) generates stresses which can transfer momentum vertically and mix the water column. However the level of shear required to generate instabilities in stratified fluids also depends on the strength of stratification. A parcel of stratified fluid displaced vertically from its position of neutral density will experience a buoyancy force that will cause it to accelerate back to its equilibrium, overshoot and oscillate at a frequency known as the buoyancy frequency, N. Stronger stratification leads to a higher the buoyancy frequency and greater buoyancy forces making the fluid harder to mix.

$$N = -\frac{g}{\rho_0}\frac{\delta\rho(z)}{\delta z} \tag{1.10}$$

Where ρ_0 is the density, $\delta\rho(z)/\delta z$ is the vertical density gradient and g the acceleration due to gravity. An important relation which quantifies the stability of a stratified water column is the gradient Richardson number, Ri, which can be used as a criterion for the development and maintenance of turbulence. It calculated as the ratio of the buoyancy frequency squared (N^2) over the shear squared (S^2):

$$Ri = \frac{N^2}{S^2} \tag{1.11}$$

A gradient Richardson number of $Ri < 1$ is necessary to maintain turbulence, although this does not allow for TKE dissipation to heat. For the initiation of turbulence a more demanding criterion of

$Ri < 0.25$ is widely used. This result of stability analysis by Miles [1961] and Howard [1961] is the generally accepted level at which the de-stabilising effects of shear overcome the stabilising effects of stratification and shear instabilities and internal wave breaking occur.

1.4 Measuring turbulence

Measurement of turbulence is technologically challenging due to the small spatial and temporal scales and random nature. Efforts in the ocean have concentrated on high frequency velocity and scaler (e.g. temperature) fluctuations, eliminating the need for a fixed reference point but demanding fast-response sensors [Thorpe, 2009]. The quantity measured is generally ε , the dissipation rate of turbulent kinetic energy (TKE). This is the energy at the small scales known as the Kolmogorov microscales at which the energy is dissipated by viscous forces as heat. ε is commonly measured using airfoil probes of the type first described by Osborn and Crawford [1980]. These produce electrical signals generated by a piezoelectric crystal when subjected to lateral forces generated by shear in the flow. These signals are interpreted as a spectrum of shear as a function of wavenumber. The theoretical form of the cascade of turbulence was developed by Kolmogorov in 1941 and takes the characteristic form:

$$\Phi(k) = q\varepsilon^{2/3}k^{-5/3} \tag{1.12}$$

Where the spectral kinetic energy density Φ_{KE} is a function of the dissipation, ε, and the wavenumber k $= 2\pi/$(eddydiameter), q is a dimensionless constant. Measured spectra can then fitted to this characteristic form to find a value for the dissipation e.g. figure 1.3.

The use of microstructure profilers in shelf seas has improved our understanding of boundary mixing theory with the highest rates of TKE dissipation observed in the ocean occurring in the shelf seas close to the bed (10^{-3} to 10^{-1}Wm^{-3}) oscillating at twice the tidal period Simpson and Crawford [1996]. Turbulence in the bottom boundary layer reaches up a limited distance above the bed in the stratified region with dissipation higher up the water column lagging that at the bed [Rippeth, 2005]. However dissipation measurements soon discovered unexpectedly high levels of dissipation in the thermocline [Grant et al., 1968] which could not be interpreted in terms of the traditional boundary mixing theory. The temporally patchy, enhanced rates of dissipation in the thermocline region, typically 10^{-4} to 10^{-3}Wm^{-3} have been observed in many studies and appear to be a feature of shelf seas [Rippeth, 2005; Green et al., 2008; Palmer et al., 2008].

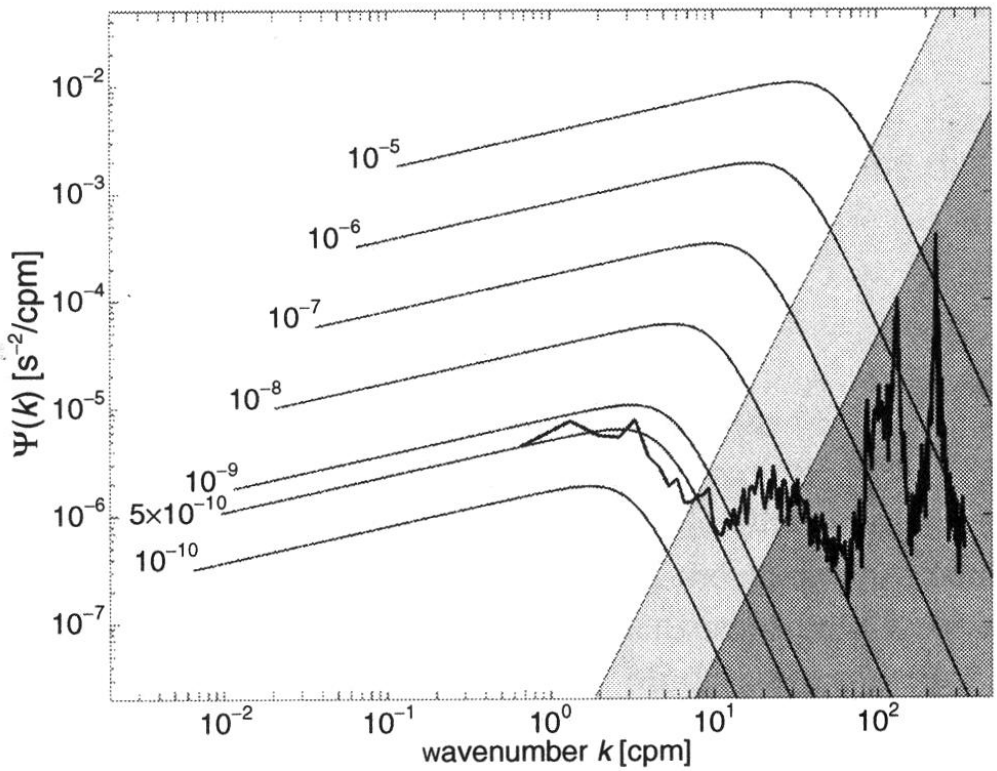

Figure 1.3: Nasmyth universal shear spectra curves showing the Kolmogorov -5/3 relationship for a range of TKE dissipation rates [Lueck, 2005]. The data plotted is the spectrum of measured vertical shear of microstructure velocity in a region of low turbulence. Deviation from the Nasmyth curve is due to instrumental noise which is evident at low energy levels. The left hand edge of the lightly and darkly shaded regions indicate the wavenumbers at which the variance (area under curves) reaches 87% and 96% of the total shear variance respectively.

1.5 Modelling turbulence

Developing an understanding of the elevated rates of thermocline dissipation has been a key research area in observational oceanography because of the inability of models to reproduce observed levels of mid-water mixing.

Models in shelf seas generally consider the various forces on the water column and apply equations of motion to calculate the velocity components u and v, e.g. Luyten et al. [1996]; Simpson and Crawford [1996]. Tidal forcing is applied by a surface slope or pressure gradient $\delta P_r/\delta x$ $\delta P_r/\delta y$, which is driven at the local tidal period and by surface stresses $\tau_s x$ $\tau_s y$, due to the wind. The Coriolis force, $F_c = fv$, describes the force due to the earths rotation in terms of the Coriolis parameter f (equation 1.16). The frictional forces are described by the final term in equation 1.13 in terms of the current shear $\delta u/\delta z$ and an eddy viscosity N_z.

$$\frac{\delta u}{\delta t} = -\frac{1}{\rho}\left(\frac{\delta P_r}{\delta x} + \frac{\delta \tau_{sx}}{\delta x}\right) + fv + \frac{\delta}{\delta z}\left(N_z \frac{\delta u}{\delta z}\right)$$

$$\frac{\delta v}{\delta t} = -\frac{1}{\rho}\left(\frac{\delta P_r}{\delta y} + \frac{\delta \tau_{sy}}{\delta} y\right) + fu + \frac{\delta}{\delta z}\left(N_z \frac{\delta v}{\delta z}\right) \tag{1.13}$$

Such models tend to use a "turbulence closure scheme" to calculate an eddy viscosity using a function based on Richardson number criteria:

$$N_z = func\left(\frac{N^2}{S^2}\right) + v \tag{1.14}$$

Where v is the "background" diffusivity, and should only represent the molecular diffusivity.

Applying this type of 1D model, with a Mellor-Yamada turbulence closure scheme, to shelf seas Simpson and Crawford [1996] found that the observed vertical structure of dissipation was well reproduced in fully mixed regions demonstrating that the traditional boundary mixing theory is well understood (see figure 1.4a). However in stratified regions the model was less capable of reproducing the observed levels of dissipation. Applying a physically reasonable rate of turbulent diffusion (scheme MY2.2a) the mid-water dissipation levels predicted by the model were 4 orders of magnitude below the observations (see figure 1.4b).

A common method for overcoming the shortfall in mid-water mixing is the use of a background diffusivity much greater than that due to molecular diffusion. This approach is examined by Rippeth [2005] who generated seasonal temperature cycles using a 1D turbulence closure model with three different levels of background diffusivity. Reproduction of the observed temperature cycle required

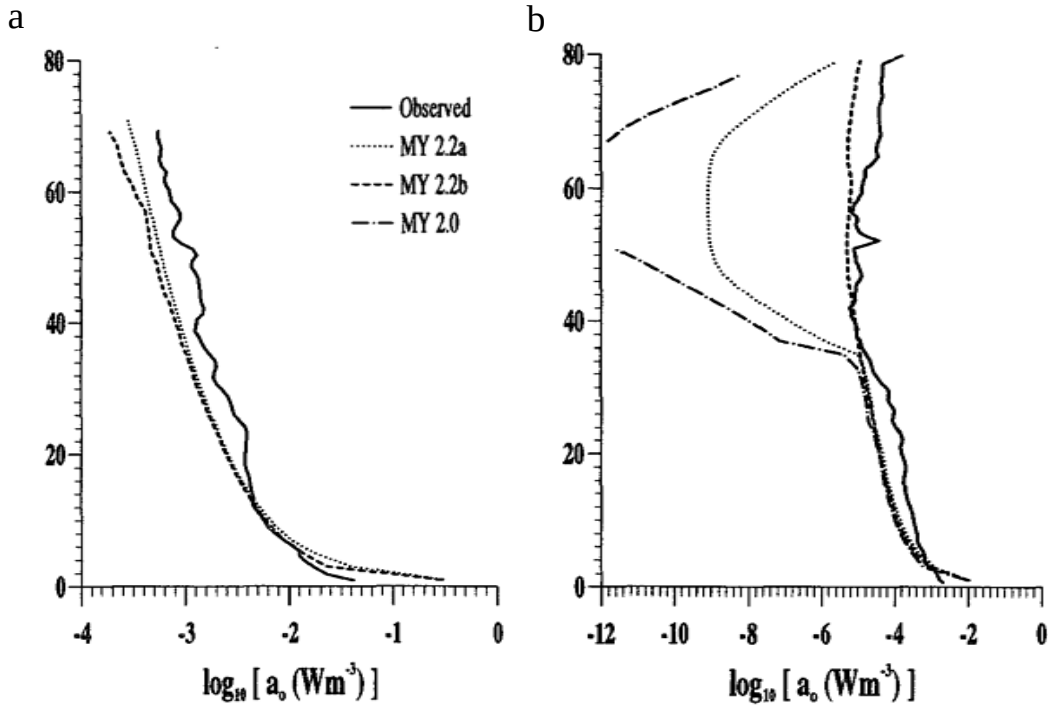

Figure 1.4: Observed and modeled vertical profiles of dissipation from a well mixed region (a) and a stratified region (b). Simpson and Crawford [1996]

a diffusivity much higher than molecular diffusivity, $\sim 3.5 \mathrm{cm}^2\mathrm{s}^{-1}$ (molecular diffusivity of heat in seawater is $\sim \times 10^{-3} \mathrm{cm}^2\mathrm{s}^{-1}$). An elevated background diffusivity would not be an issues if this diffusivity was consistent, however it varies both spatially and temporally [Elliott, 1995].

The failure of models to reproduce the observed levels of variable elevated mid-water mixing in stratified regions leads to the conclusion that there is a mid-water source of TKE which is not included within the models.

1.6 Sources of thermocline shear

Measurements of the gradient Richardson number in shelf seas show that thermocline is in a state of marginal stability $Ri \sim 1$ [Van Haren et al., 1999; Rippeth et al., 2005] and that an additional input of shear would be sufficient to initiate mixing. ADCP and microstructure measurements show that elevated levels of dissipation in the thermocline coincide with periods of enhanced shear [Rippeth et al., 2005; Burchard and Rippeth, 2009; Rippeth et al., 2009]. Identifying and understanding sources of the mid-water shear is therefore a key challenge for observational oceanographers in the shelf seas. Two possible baroclinic oscillatory motions, internal waves and inertial oscillations, have been proposed to act as an additional source of shear which could initiate mixing in the thermocline. These processes are outlined in the following two sections.

1.6.1 Internal waves

Internal tides generated in the deep ocean have gained an increasingly important role as part of climate theory. This is because they may provide a significant proportion of the 2.1TW mixing energy required to drive heat down and drive the thermohaline circulation [Munk, 1998; Garrett, 2003]. Egbert and Ray [2000] used satellite altimetry data to show that 1TW or more is dissipated in the deep ocean as a result of tidal flow interacting with bathymetric features, this is comparable to the estimated input from wind [Munk, 1998]. Despite this large figure most of the tidal energy in the oceans is dissipated in the shallow shelf seas.

An internal tide occurs where barotropic tide flows over topography displacing stratified water up and down the topographic slope. Internal tide generation occurs around the world, most commonly at the continental slope where internal tidal waves propagate off-shelf into the deep ocean and onto the shelf. These waves generally take the form of semi-diurnal oscillations in the vertical height of the thermocline and are accompanied by oscillating baroclinic currents. However shorter period waves are often associated with the internal tide. These high frequency nonlinear internal waves (NLIWs) have periods of 10 to 30 minutes, and amplitudes from several metres to hundreds of metres and are associated with the interaction of the internal tide with the shoaling seabed.

Observations of internal waves reveal a variable and intermittent process with the internal tide not always in phase consistent with the barotropic tide. The flux of internal tidal energy onto the shelf varies with location with estimates based on observations ranging from $100-400\mathrm{Wm}^{-1}$ [Sherwin, 1988; Sharples and Moore, 2001; Green et al., 2008]. A linear internal tidal model used by Baines [1982] estimated on-shelf fluxes in the Celtic Sea to be between $300-560\mathrm{Wm}^{-1}$. While this is considerably

less than the energy in the barotropic tide as discussed previously this energy is considerably more efficient at mixing at the thermocline. Direct observations at the shelf edge confirm highly elevated levels of integrated thermocline dissipation associated with the internal tide, $8-28\mathrm{mWm}^{-2}$ [Inall et al., 2000; Sharples and Moore, 2001; Rippeth, 2005; Green et al., 2008].

The high levels of mixing at the shelf edge are reflected in the vertical structure of temperature close to the shelf break which is diffuse with reduced surface temperatures [Green et al., 2008]. The consequences of this vertical mixing is also reflected in elevated nutrient and chlorophyll concentrations (both surface and subsurface waters) [Sharples et al., 2007]. An example of this indirect evidence of internal wave mixing at the shelf break is presented in figure 1.5. However the on-shelf extent of enhanced mixing due to the internal tide appears to be limited to a region only tens of kilometers from the shelf break [Rippeth, 2005; Green et al., 2008; Inall et al., 2011]. Local on-shelf topography is also capable of generating internal waves and associated mixing, although this is likely to be localised. This leaves a large portion the shelf seas with relatively low internal wave activity, and while levels of observed dissipation are much lower ($\times 10^{-5}\mathrm{Wm}^{-2}$) than the highly turbulent thermocline close to the shelf break these are still orders of magnitude higher than may be explained by molecular diffusion and the SCM is still a persistent feature. Another candidate mechanism is therefore required to explain these observations.

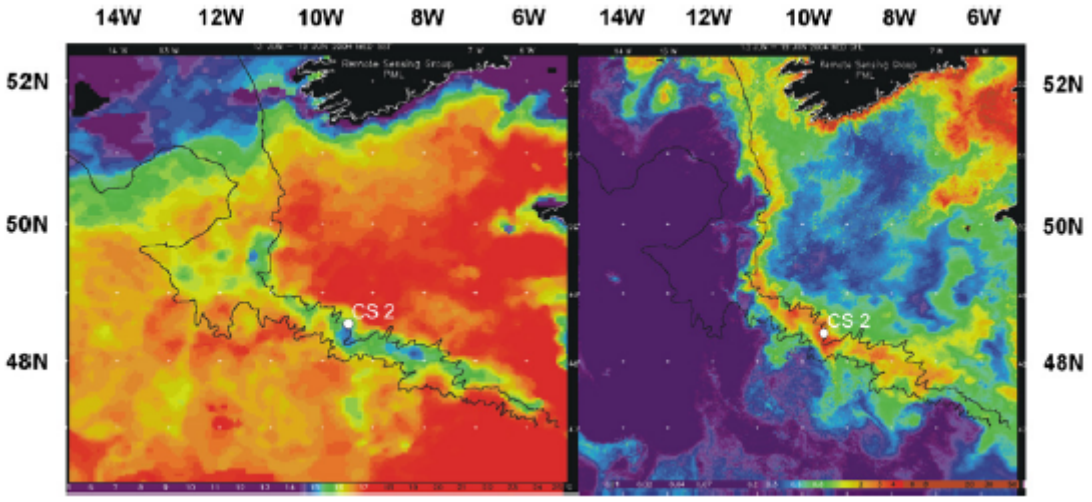

Figure 1.5: Average sea surface temperature and chlorophyll concentration in the Celtic Sea from satellite images. [Green et al., 2008]. Lower SST and higher chlorophyll levels close to shelf break are indicators of enhanced thermocline mixing due to internal wave activity.

1.6.2 Inertial oscillations

Inertial oscillations are periodic currents which occur primarily in the upper ocean. The currents are oscillatory due to the earths rotation which generates an apparent force called the Coriolis force which acts to steer currents to the right in the northern hemisphere and left in the southern hemisphere. The acceleration per unit volume due to the Coriolis force is as follows:

$$F_{Cx} = fv$$
$$F_{Cy} = fu \tag{1.15}$$

Where u and v are the velocity components in easterly and northerly components respectively and f is the Coriolis parameter:

$$f = 2\Omega sin\phi_L \tag{1.16}$$

Where Ω is the rotation rate of the Earth and ϕ_L is the latitude.
The period of the currents is also dependent on the latitude:

$$T = \frac{2\pi}{f} \tag{1.17}$$

Practical advancements in the observation of current velocities showed that inertial currents are ubiquitous features of the upper ocean which are produced by abrupt changes in wind stress [Sherwin, 1987; Knight et al., 2002]. In shelf seas the well mixed upper layer acts like a slab exhibiting uniform inertial currents with the thermocline acting as a low friction interface decoupling the bottom layer [Simpson et al., 2002]. However inertial currents do exist below the thermocline, these are 180° out of phase with those in the surface layer [Rippeth et al., 2002]. This is explained as the action of the wind stress normal to the coast setting up a surface slope which sets up a barotropic pressure gradient throughout the water column [Craig, 1989]. The effect has been used as possible evidence for increased shear at the thermocline [Pollard et al., 1972; Rippeth, 2005].
Acoustic current measurements of the thermocline currents reveal that the thermocline is often dominated by baroclinic currents at the inertial frequency [Knight et al., 2002; Rippeth, 2005; Palmer et al., 2008]. Although inertial currents have been shown to generate shear across the thermocline this shear tends to be concentrated at the top of the thermocline [Van Haren et al., 1999]. It is unclear whether inertial oscillations alone are sufficient to drive instabilities at the centre of the thermocline or whether they act in the same way as wind driven boundary mixing.

A study by Burchard and Rippeth [2009] may provide an mechanism by which inertial oscillations directly mix the thermocline through a feature known as inertial shear spiking. In their observations from the northern North Sea periods of high wind stress were accompanied by a series of spikes in the bulk shear, S_b. This bulk shear was calculated shear across the thermocline weighted by the distance between the top and bottom layer (half the depth h):

$$S_{BR}^2 = \left(\frac{u_s - u_b}{1/2(h)}\right)^2 + \left(\frac{v_s - v_b}{1/2(h)}\right)^2 \tag{1.18}$$

Where u_s and v_s represent easterly and northerly surface layer velocities and u_s and v_s represent the corresponding bottom layer velocities.

The magnitude of the spikes in S_{BR}^2 were not correlated directly with wind stress. Periods of high wind stress were sometimes accompanied by low S_{BR}^2 and periods of high S_{BR}^2 were observed at times of relatively low wind stress. The spikes generally occurred at an inertial period, although this was not always the case. The authors constructed a simple two layer model to explain the observations in terms of wind and bed stress vectors, τ_s and τ_b, and a bulk shear vector $\vec{S_{BR}}$ (figure 1.6).

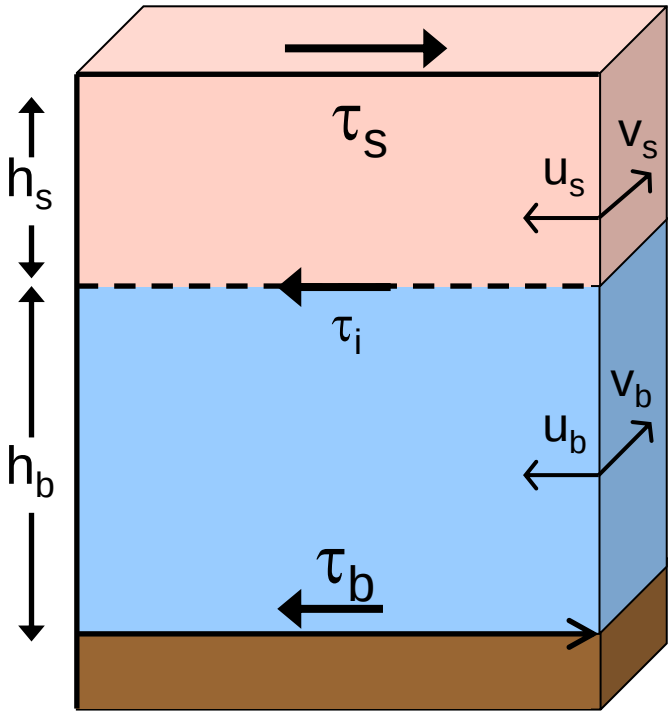

Figure 1.6: Schematic of the model used by Burchard and Rippeth [2009] to develop a mechanism for the generation of bulk shear spikes.

The model proved a success by replicating the observed pattern in the production of bulk shear, based

on the following result:

$$\frac{\delta S_{BR}^2}{\delta t} = \frac{4}{h}\vec{S_{BR}}\cdot\left(\frac{\vec{\tau}_s}{h_s} + \frac{\vec{\tau}_b}{h_b}\right) + c_i\frac{h^2}{h_s h_b}S_{BR}^3 \tag{1.19}$$

Where h_s, h_b and h are the surface layer bottom layer and total depth and c_i is a drag coefficient. The first term on the RHS represents the production of shear, although it should be noted that this may be negative and its contribution to the total magnitude of shear is much greater than the second term which represents the dissipation of energy to mixing at the thermocline. The key result of the model is that the maximum production of shear occurs when τ_s and τ_b are in perfect alignment, i.e the dynamics the surface layer velocity and wind direction are the same. This result was supported by their observations which are presented in figure 1.7 with circles indicating where the wind and bulk shear vectors align. This process is important to understand because in order to predict the correct magnitude of shear there must be sufficient temporal resolution of the wind which may not be satisfied by models using modeled wind fields.

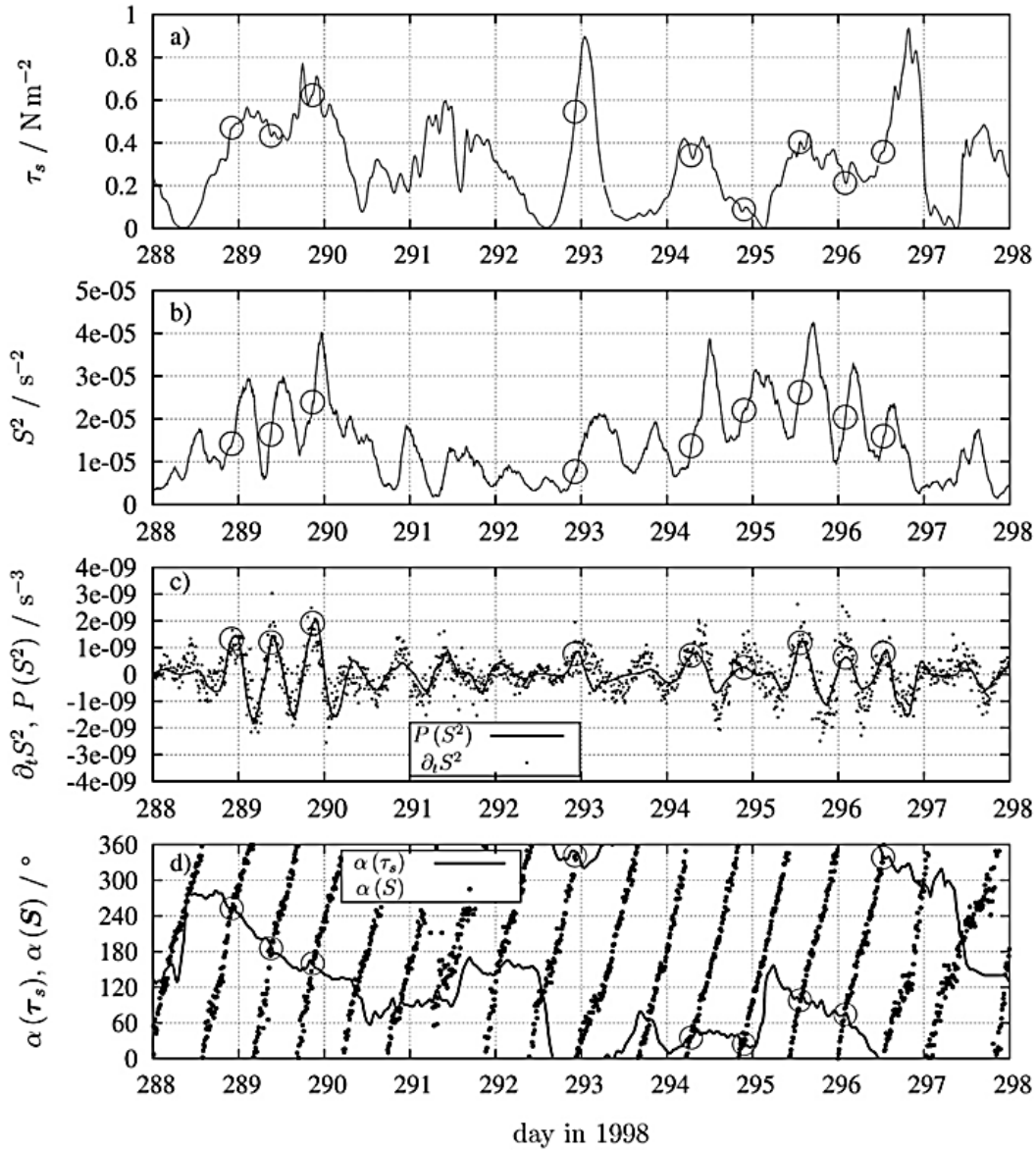

Figure 1.7: Inertial shear spike observations from the northern North Sea Burchard and Rippeth [2009] (a) surface wind stress, τ_s; (b) magnitude of bulk shear squared, S^2_{BS}; (c) Production of bulk shear squared, P (S^2_{BS}). (d) Direction of surface shear stress and bulk shear. Circles denote time of alignment between bulk shear and wind direction where shear production is a maximum.

1.7 Aims of the study

In this chapter the importance of thermocline mixing in shelf seas has been explained. Two potential candidates have been highlighted for the anomalous observed thermocline mixing, inertial oscillations and internal waves. This study aims to examine these processes by collecting data over an entire summer stratified period using a mooring in the Western Irish Sea supplemented by measurements of TKE dissipation collected on mooring deployment cruises.

The Irish Sea is mostly vertically well mixed by strong barotropic tidal currents which generate energetic turbulence. However during summer months the north-west region becomes stratified because surface heating out competes the weaker tides in this deeper part of the sea. The stratified region is bounded by the Irish coast to the west and separated from the well mixed waters of the rest of the Irish Sea by a tidal mixing front [Simpson and Hunter, 1974; Simpson and Sharples, 2012].

The Western Irish Sea has a number of advantages for our observations. The location is relatively easy to access using Bangor University's research vessel the RV Prince Madog, since it takes only 5 hours to reach from the port at Menai Bridge. The Western Irish Sea is a fairly well understood stratified region since it has been well studied over the years. Both of the candidate mechanisms are known to operate in the Western Irish Sea with inertial shear spikes observed by Rippeth et al. [2009], while a significant internal tide and NLIWs were observed by Green et al. [2010].

The specific goals of the study are to:

- Collect a high vertical resolution time series of velocity and vertical temperature structure within the thermocline region of the Western Irish Sea, accompanied by full local meteorological data.
- Identify periods of high wind stress where wind driven inertial oscillations generate bulk shear spikes and interpret the bulk shear dynamics in terms of the wind forcing.
- Use high resolution N^2 and S^2 observations to identify instabilities during shear spikes.
- Make direct measurements of the TKE dissipation rate (ε) during a period of wind driven inertial shear spiking.
- Understand whether inertial shear spikes act as a form of boundary mixing or a source of mid-water TKE using observations of dissipation and changes in vertical density structure.
- Replicate inertial shear spikes using 1D turbulence closure model to identify whether additional physics is required in order to reproduce the observations.
- Characterise the internal tide and NLIWs and quantify the energy they contain to determine whether there is sufficient energy within the internal wave field to account for the observed mid-water dissipation.
- Use high resolution N^2 and S^2 observations to identify instabilities associated with the internal tide and NLIWs.
- Test the hypothesis that the vertical density structure can be used as a record of the mixing history to provide a quantification for internal wave mixing.

1.8 Structure of the thesis

The structure of the thesis will continue as follows;

- **Chapter 2** - Description of the observations, analytical methods and models used for interpretation of the data presented within the thesis
- **Chapter 3** - Overview of the moored data series describing the evolution of the stratification and baroclinic currents. Identify the prevalence, magnitude and character of the two candidate processes of thermocline mixing. Periods when each of the mechanisms dominate are identified for more detailed examination in subsequent chapters.
- **Chapter 4** - Examines periods when the mechanism of inertial shear spiking is dominant and seeks to explain the observed dynamics during these periods in terms of the wind forcing. The stability of the water column is analysed during periods of shear spiking and linked to changes in the vertical structure of temperature during these events. Direct measurements of turbulent dissipation are examined for a period of low magnitude shear spiking. Two models are then employed to replicate the observed periods of shear spiking in order to understand whether current knowledge of the physics within such models is sufficient to describe the observations.
- **Chapter 5** - Two consecutive periods of low wind stress and strong baroclinic tidal currents are examined in order to understand the evolution of the vertical current and temperature structure due to internal waves. The energy available for mixing by the internal tide is investigated for a period of strong mode one activity. NLIWs are also investigated with one particular strongly dissipative case analysed in detail.
- **Chapter 6** - The idea that the vertical structure of stratifcation is a record of the history of vertical mixing and can be used to quantify rates of internal wave mixing is explored using the Irish Sea data series and spatial datasets from the Celtic Sea and Malin Shelf. These ideas are tested using a simple model of stratification.
- **Chapter 7** - A discussion of the results in the context of previous work with suggestions of directions for the future.

Chapter 2

Observations and methods

This chapter provides details of observations and measurements, the instruments used to make them and the methods employed to analyse them. First the dates and locations of the research cruises and moorings are outlined. Next the instruments deployed are described along with their setups and any calibrations that were required. The details of analysis methods used in subsequent results chapters are then described. Lastly an overview of three simple models used in the thesis are presented.

2.1 Location and duration of observations

The aim of the mooring was to collect data spanning a full seasonal cycle of stratification, current velocities and the local wind field. The position of the Western Irish Sea (WIS) mooring (53°47.00N 005°38.00W Fig.2.1) was chosen since it was near to a Northern Ireland Agriculture Buoy which has been in this location for a number of years. Since the mooring would be left unattended for two months at a time it was hoped that the presence of the buoy would reduce the risk of disturbance to the mooring by fishing activity. This proved to be of limited success with instrument loss due to fishing activity reducing the useable data to the first half of the seasonal cycle of stratification. The deployment lasted 51 days from May 19th 2009 to July 9th (day 138 to 189) and the moorings were deployed during research cruises on the the RV Prince Madog. Two 48 hour time series of dissipation were obtained during mooring deployment cruises by intensive vertical profiling using a vertical microstructure profiler (VMP). The setup used for the measurements are presented in the following sections with details on the methods employed for processing and analysing the data

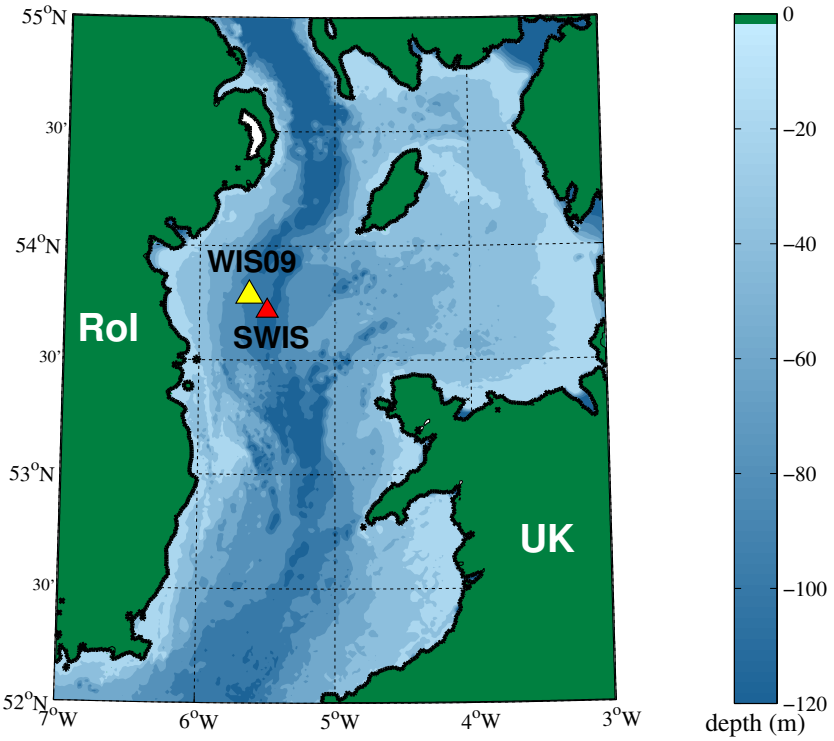

Figure 2.1: Map of the Irish Sea showing mooring position WIS for 2009 data. Also shown mooring position SWIS from the 2006 campaign.

2.2 Mooring arrangement

The mooring arrangement was designed to resolve processes in the thermocline region and thus focused on the upper half of the water column since the lower half tends to be well mixed by the strong baroclinic tidal currents (see Fig 2.2). Microcat CTDs were located at the mooring anchor and on the mooring buoy to accurately resolve temperature and salinity at the surface and the bed. The 20 StarODI thermistors were located every 2.5m in the upper 45m so as to resolve the temperature structure in the upper half of the water column. Acoustic current Doppler profilers (ADCPs) were deployed 300m from the temperature sensor mooring with a chain line between the moorings to aid recovery in the case of mooring failure. A 300 kHz RDI workhorse adcp was mounted on the bed in order to measure the full water column velocity structure. However a software fault resulted in a failure of the 300kHz ADCP to record any data. All velocity data presented therefore is measured by the 600kHz RDI Workhorse broadband ADCP which was mounted in a float at a height of 55m above the bed on a separate mooring so that the motion of the thermistors did not interfere with the acoustic measurements. Details of the calibration and processing of the data collected by the moorings is presented in the following sections.

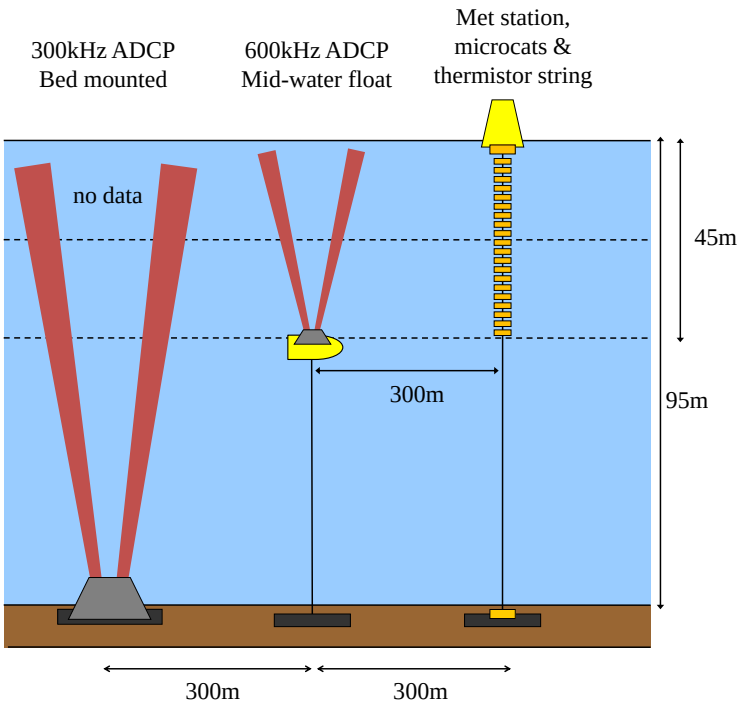

Figure 2.2: Schematic diagram showing the instruments deployed on the mooring

2.2.1 Thermistors

The thermistors were set to record every 5 minutes which was sufficient for capturing the internal tide and inertial motions but was slightly low for sampling the high frequency internal waves, however these were not expected to be an important feature of the study initially. Thermistors and microcats were placed together in a calibration bath with water through flow for several hours for calibration both before and after deployment. Temperatures recorded during calibration differed by less than 0.05°C from the mean, while drift over the deployment was less than this so no compensation was deemed to be necessary.

The main processing of the data for the mooring was estimating the depth of each thermistor at a given time. The thermistor string was suspended from the surface buoy and so moved relative to the bed with the sea surface at a tidal frequency. Every fourth thermistor had the capacity to record pressure which showed that the drag due to currents affected the position of the thermistors, bringing them closer to the surface as current speed increased. The height above the bed of these pressure sensing thermistors was therefore calculated simply by subtracting the pressure they recorded from that recorded at the sea bed by the Microcat. The thermistors without pressure sensors were equally spaced between those with, and so their position was found by linear interpolation. The positions of the thermistors according to these calculations are shown in figure 2.3.

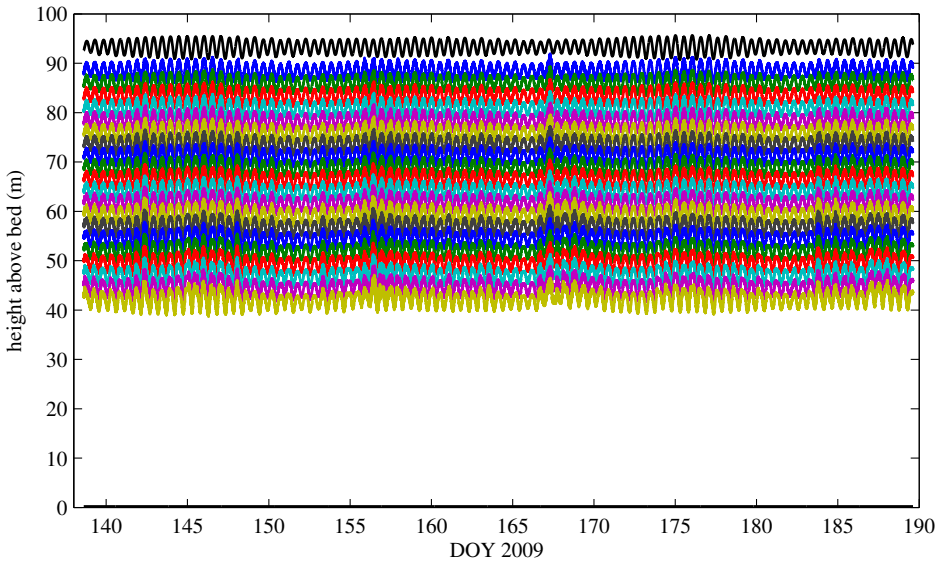

Figure 2.3: Plot of the height of the thermistors above the sea bed. Surface and bottom plots are the microcat CTDs.

2.2.2 Acoustic Doppler current profilers

The setup parameters for the mid-water ADCP are given in Table.1.1. The adcp pressure sensor shows that it was on average 35m below the surface. The position of the adcp relative to the bed was calculated from the difference between the pressure recorded by the Microcat located at the bed and the pressure on the adcp. Drag from the barotropic tide and wind driven currents caused variablity of several metres in the height of the ADCP above the bed. Therefore this calculation was performed at each time interval to give a matrix of heights for each velocity measurement in time and space. These currents also affected the pitch and roll of the ADCP with a mean deviation from the vertical of 1.3°, with angles only exceeding 2° for brief episodes (up to a maximum of 5°). At such times there was a vertical displacement of the ADCP of up to 2m below its equilibrium position. There is a blanking region of 1.92m close to the ADCP and close to the sea surface side losses due to reflection of the beams limited the data to $\sim$ 6m below the surface. The average coverage of the adcp data was therefore from 59m to 88m above the bed, giving 29m of useable data. In order to reduce the computation time when working with the data, velocities were averaged to 5 minutes. Some analysis techniques, (spectra & Richardson numbers) required a common vertical scale for the data, so at each time interval the velocities were linearly interpolated onto a regular grid with 1m spacing.

Table 1.1: Mid-water ADCP setup

frequency	600kHz
beam angle	20°
operating mode	12
bin size	50 cm
ensemble rate	30 seconds
pings per ensemble	1

2.2.3 Meteorological observations

The surface buoy failed to collect any data which was a considerable setback to the goal of linking the local wind forcing to the generation of inertial shear spikes. The wind data that is instead used to complement the mooring data is from a UK Meteorological office mesoscale model. This product integrates land based observations to model the wind field across the British Isles to give a 3 hourly wind speed and direction at a horizontal resolution of 11 minutes. The time series used has been extracted for the location of the mooring.

A comparison between the reanalysis wind and real data from the region is possible using measurements from a met buoy located in the same mooring location for 40 days in the following summer (2010). The buoy data requires adjustment due to the height of the anemometer which is located 1.5m above sea level. The velocity profile in the boundary layer above the ocean is generally accepted to follow the logarithmic law:

$$W_z = \frac{W_*}{\kappa} ln \frac{z}{z_0} \tag{2.1}$$

This relates velocity W_z at height z to the wind stress through the friction velocity W_* using equation 2.2 and von Kármán' s constant which is generally taken as $\kappa = 0.41$. z_0 is the boundary roughness and describes the roughness of the sea surface. The friction velocity is related to the wind stress τ_s through equation 2.2:

$$\tau_s = \rho_a W_*^2 \tag{2.2}$$

where ρ_a is the density of air. Rearranging equation 2.1 in terms of W gives:

$$\frac{W_*}{\kappa} = W ln \frac{z}{z_0} \tag{2.3}$$

as the LHS of equation 2.3 is constant for a given wind stress it can be used to relate the velocity at different heights. This relation can be formed to give an expression describing the wind at 10m, W_{10} as a function of the wind at height z:

$$W_{10} = W_z \frac{ln(10/z_0)}{ln(z/z_0)} \tag{2.4}$$

The value of z_0 is dependent on the speed of the wind, which had a mean magnitude of 5.2ms^{-1} for the 2010 data. Bowden [1983] gives a value of $z_0 = 2.1 \times 10^{-4}$ for wind speeds of 5ms^{-1}. This value gives a scaling factor of 1.21 to convert the buoy observations to the 10m wind levels used in the met office reanalysis winds.

Figure 2.4 presents a plot of the adjusted observed wind and the met office reanalysis modeled wind for summer 2010. The raw observed data is presented in pane a and a 3 hour average in pane b. The likeness is good, with a mean for the period of 6.4ms^{-1} for observed and modeled data sets and a standard deviation of 2.9ms^{-1} and 2.7ms^{-1} respectively. The 10 minute observations are considerably more gusty, with peak winds up to 30% higher than the mean. This will have implications for the energy input from the wind due to the way that wind stress is related to the square of wind speed using the following equation:

$$\tau_s = \rho_\alpha C_D U_{10}^2 \tag{2.5}$$

Where $\rho_\alpha = 1.3\text{kgm}^{-3}$ is the density of air and C_D is the drag coefficient. The value for C_D used has been calculated by a parameterisation by Yelland and Taylor [1996] based on observations in the Southern Ocean. This has two forms, one for low wind speeds and one for higher wind speeds:

$$1000C_D = 0.29 + \frac{3.1}{U_{10}} + \frac{7.7}{U_{10}^2} \qquad (3 \leq U_{10} \leq 6ms^{-1}) \tag{2.6}$$

$$1000C_D = 0.60 + 0.070 * U_{10} \qquad (6 \leq U_{10} \leq 26ms^{-1}) \tag{2.7}$$

The implications of using averaged wind speed to calculate the wind stress were examined by comparing the wind stress from 10 minute observations to the 3 hour averaged data for the same observations. The mean wind stress for the 10 minute observations was higher than for the 3 hour average of the same data, but the difference was small at only 4%, therefore no adjustment was deemed necessary for the use of the low resolution winds.

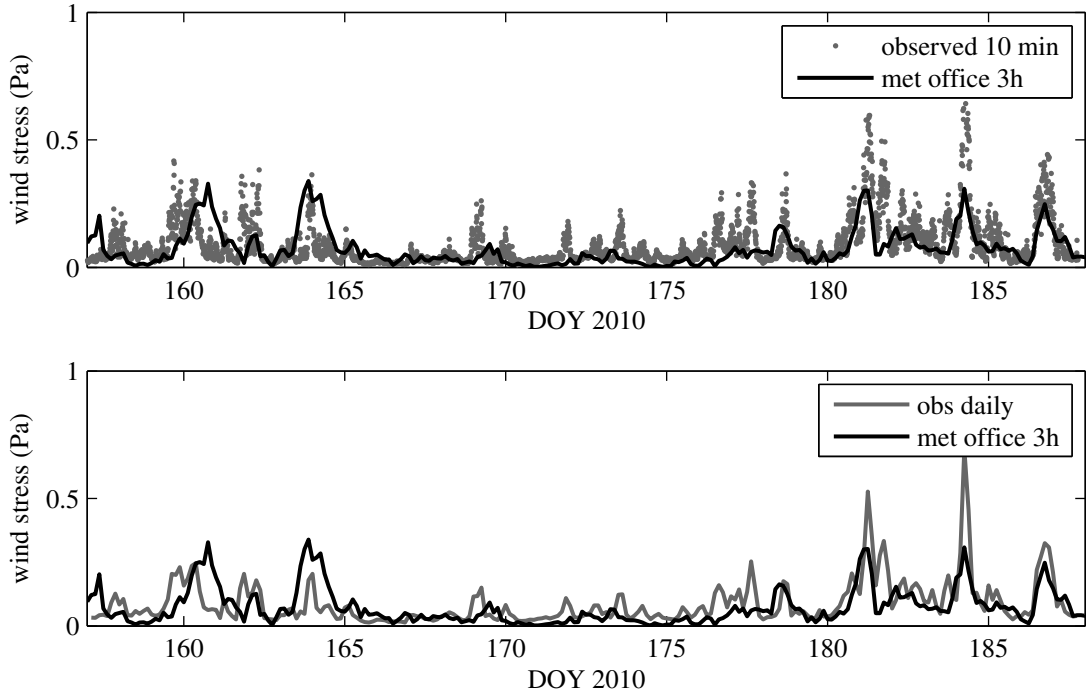

Figure 2.4: A comparison of wind observations an UK Met Office reanalysis wind stress from the Western Irish Sea in 2010. a) 10 minute observed wind stress (grey dots) and modeled wind stress (black line). b) observed wind stress averaged to 3 hours (grey line) for direct comparison with modeled wind (black line)

2.3 Shipborne microstructure observations

Measurements of turbulence were made on the July cruise using a Rockland VMP 500 coastal vertical microstructure profiler which is designed to measure dissipation scale turbulence [Rockland Scientific International, 2013]. It is a loosely tethered profiler which free-falls vertically measuring small scale velocity shear from which vertical profiles of the turbulent kinetic energy dissipation rate, ε are calculated. The profiler itself is a 1.5m tall cylinder with brushes at the top reduce vibration and control the fall rate ensuring it falls vertically (figure 2.5). There is a Seabird temperature/conductivity cell mounted on the side of the instrument, while the microstructure probes are mounted at the bottom, where they are protected from impact with the sea bed by a metal guard. Velocity shear is measured by airfoil probes, which consist of piezoelectric sensors encased in resin. These produce a voltage which is proportional to the sideways force applied to them. This sideways force is also proportional to the velocity of the current producing it. Therefore the time derivative of the voltage (performed electronically) is a measure of the horizontal velocity shear. The design of the sensors and the fall rate of the instrument are chosen so that the length scales measured are the Kolmogorov microscales at which 90% of TKE dissipation occurs. For the observations presented the fall rate of the VMP was $\sim 0.65 ms^{-1}$.

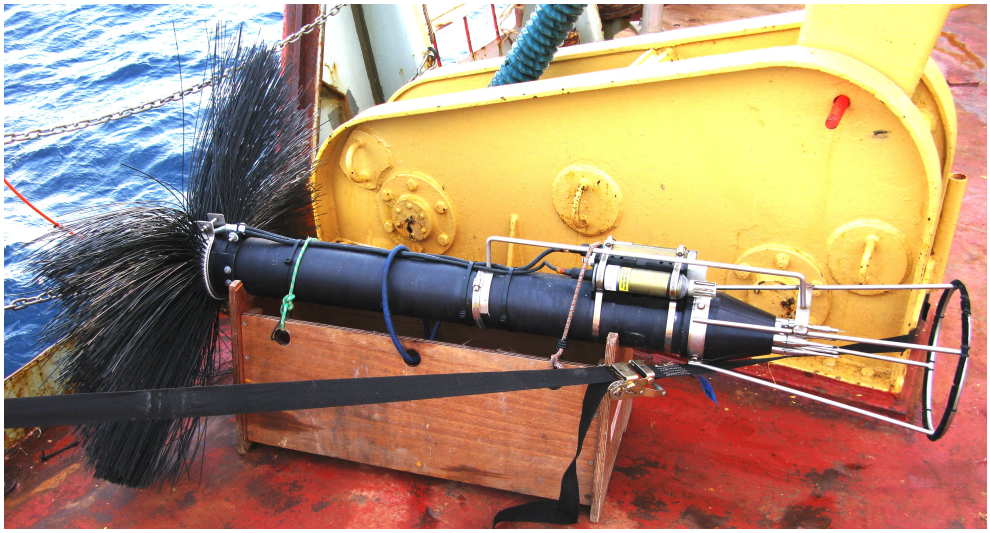

Figure 2.5: The Rockland VMP 500 micrstructure profiler. The probes are mounted at the bottom of the instrument (RHS) and are protected by a probe guard. A Seabird CTD unit is mounted on the body of the instrument. Brushes at the top of the instrument slow its fall rate and cause it to fall vertically (LHS). Power and data transmission are provided by the orange cable (LHS) which is also used to retrieve the instrument after each cast.

The VMP is tethered to the ship by a kevlar reinforced cable which is used to power the instrument and transmit the digitised data back to the ship for recording on a computer. In order to fall freely, a hydraulic line puller feeds excess cable over the side of the ship. A winch is used to recover the profiler when it has reached the sea bed. One profile plus recovery at 95m depth takes ~ 6 to 10 minutes which allows 6 to 10 profiles each hour. In order to prevent the cable from fouling the propeller the profiler is deployed from the stern of the vessel which holds a speed of ~ 0.5kt. The ships speed and tidal currents eventually carry the ship away from the mooring site, requiring the ship to reposition. At such a time (approximately every 3h) a CTD cast was made. The microstructure data presented here is from the final two days of the mooring deployment and covers the 48h period from 7th July to 9th July. During this time 279 profiles of shear were collected, however these required further processing steps in order to produce estimates of turbulent dissipation rate.

A region close to the surface is usually contaminated with turbulence generated by the ship. However the limiting factor in observation of the surface layer is the time taken to reach terminal velocity (usually 10 seconds) which prevents observation in the top 5 to 10m . The practical details of processing shear data is well described by Stips in Baumart Z et al. [2005] but the manual steps required are outlined here. The first stage was to examine the profilers fall rate and crop the data to that period when terminal velocity has been reached and before it hits the bed. The shear probes are susceptible to collisions with objects within the water (zooplankton, jellyfish, seaweed etc.) which cause spikes in the data. These spikes must be removed in order to avoid overestimating the dissipation rate. Software written to do this replaces the chosen spike region with data from either side of it, however the laborious process of spike identification must be done manually. Once all spikes are removed the provided software divides the shear records into 2 second sections (which approximate to 1.2m of vertical data). A shear spectra is produced for each section showing the shear as a function of wavenumber. The sensitivity of the probe is such that the range of the spectra is that which represent the Kolmogorov microscales. At these wavenumbers energy is being converted from the turbulent flow to heat via viscous forces. The rate of dissipation ε is related to the turbulent shear by the following equation:

$$\varepsilon = \frac{15}{2}\nu\overline{\left(\frac{\delta u}{\delta z}\right)^2} \tag{2.8}$$

where $\nu \sim 10^{-6}\mathrm{m}^2\mathrm{s}^{-1}$ is the kinematic molecular viscosity and the overbar indicates a spatial average or ensemble. The integrated area under the Kolmogorov region of the shear spectrum in is used for this calculation. The integration limits used are dependent on the energy level of the spectra since wider limits may be used in highly turbulent regions where instrument noise is masked by real turbulent

shear. An example of the average spectra for the highest energy level from one vertical profile is presented in figure 2.6. The dissipation data from the two probes used in the July cruise differed by a factor of ~ 1.7 and so the two measurements have been averaged to give a mean dissipation rate, ε which is the figure presented throughout the results.

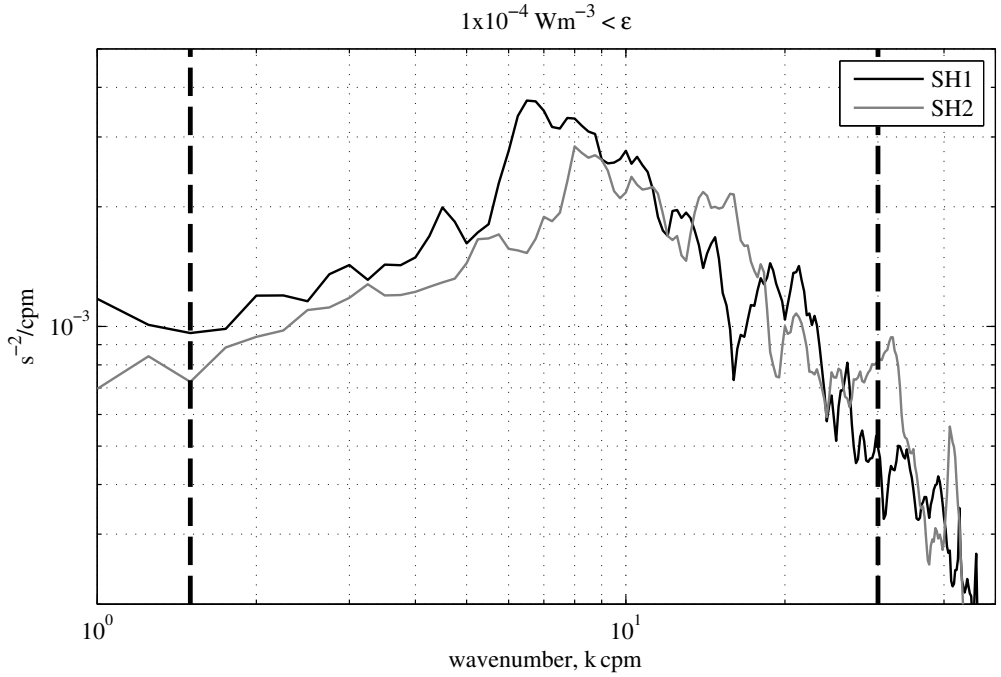

Figure 2.6: Example of the average shear spectra from one profile by the velocity microstructure profiler (VMP) for use in the calculation of the turbulent dissipation rate, ε. This composite spectra is an average of the spectra which represent the highest energy level, $\varepsilon > 1 \times 10^{-4}$. The LHS of the shear spectra shows the inertial subrange region where energy cascades to smaller scales without energy loss. The RHS of the spectra is the Kolmogorov microscales at which frequencies energy is lost to viscous forces. The dark dotted lines indicate the integration limits used to find the area under the graph which used to calculate the TKE dissipation. Integration limits are based upon the scales at which dissipation occurs and the noise limits of the instrument.

2.4 Analysis methods

The following section presents the methods and assumptions used to in the calculations and analysis presented in the results chapters.

2.4.1 Density

Density profiles were calculated using the Malab function sw_dens.m from the Matlab SeaWater (EOS80) library of seawater properties [Morgan, 1994]. The function used input profiles of temperature, salinity and pressure as recorded by the mooring. Salinity data was only available for at the surface and the bed. However stratification in the Irish Sea is primarily due to temperature. Therefore the mean value for the salinity of 34.05 was used for all calculations of density. This reduced the maximum density contrast calculated from the mooring data to 75% and 85% of that calculated from the CTD observations in May and July respectively.

2.4.2 Heat content

The heat content per square metre of the water column was calculated for each time step using the vector of density, $\rho(z)$, and of temperature $T(z)$ in a numerical integration over depth as described by equation 2.9.

$$Q = \int_{z=0}^{h} c_p(z)T(z)\rho(z).dz \tag{2.9}$$

Where z is the depth, dz the vertical resolution and $c_p(z)$ is the specific heat capacity at depth (z), which was calculated using the Matlab SeaWater library function sw_cp.m [Morgan, 1994].

2.4.3 Potential energy anomaly

Φ was calculated for each observation of the temperature structure by subtracting the depth mean density $\hat{\rho}$ from the density profile ρ(z) and numerically integrating from the surface to the bed using equation 1.1. The magnitude of Φ calculated from the moored temperature data are underestimated due to the use of a uniform salinity profile for the calculation of the density profile. Calculation of Φ for the CTD profiles collected from the ship in May and July showed that Φ values calculated using the mooring data are 70% and 80% of their true value.

2.4.4 Bed shear stress

The bed stress components τ_{bx} and τ_{by} act in the direction of flow and have been calculated from the barotropic current velocity components, u_{bt} and v_{bt} using equation 2.11:

$$\begin{aligned} \tau_{bx} &= C_{Db} U_{bt} u_{bt} \\ \tau_{by} &= C_{Db} U_{bt} v_{bt} \end{aligned} \tag{2.10}$$

Where U_{bt} is the barotropic current modulus $U_{bt} = \sqrt{u_{bt}^2 + v_{bt}^2}$. C_{Db} is a dimensionless drag coefficient, the common value for shelf seas of $C_{Db} = 0.0025$ has been used.

2.4.5 Spectral analysis

Spectral analysis was used for the interpretation of the current velocities from the mid-water adcp data. The complex form of analysis, $u + iv$, was used to define the easterly and northerly velocity components. The Matlab function psd.m was then employed to calculate a two-sided energy density spectrum which relate to the clockwise and anti-clockwise rotating components. A default Hanning window employing a window size for the barotropic spectra of 4096 data points in 14,680 records, and in the baroclinic spectra the window size was 3064 data points in the same length of record, this gave $\sim$6 and $\sim$8 degrees of freedom respectively.

2.4.6 Barotropic tidal fitting

The estimation of the barotropic tidal currents were performed by harmonic analysis using the Matlab routine T-Tide [Pawlowicz et al., 2002]. The routine reproduces the tidal signal using the sum of a finite number of sinusoids whose frequency relate to astronomical parameters. A least squares technique is employed to estimate the amplitude and phases of these tidal constituents so that the predicted output of the model captures as much of the variance in the signal at these frequencies as possible. The choice of tidal constituents is limited by the length of the record and the degree of noise in the data (due to wind driven motions).

The fit was performed at each depth of the 1m gridded velocity data and then averaged to get a depth mean energy spectra. The northerly and easterly components of the horizontal velocities were used in their complex form ($u + iv$). The fit was performed using the two principle tidal constituents M_2, S_2 as well as the shallow water harmonic M_4, which was evident in the spectra. These constituents between them explained 88% of the variance in the signal.

There was some concern that the tidal fit of the currents was a problem since the vertical coverage was limited. The validity of the fit was therefore tested using data from the 300kHz ADCP which was deployed from July to September 2009. A hindcast of the fit from the full depth currents during this period matched the fit to the mid-water currents within the errors of the instruments.

2.4.7 Baroclinic velocity

The standard method of subtracting the depth mean at each time interval to calculate the baroclinic currents could not be used because of the limited range of the ADCP data. This is because the ADCP range includes very data below the thermocline and so subtracting the depth mean had the effect of reducing surface currents and superimposing them into the bottom layer. This problem was overcome by assuming that the currents in the lower bins were representative of the bottom layer and extending them (as a linear mean) down to a height of 15m above the bed (as a crude adjustment for the bottom boundary layer) before calculating the depth mean.

2.4.8 Baroclinic velocity least squares fitting

The least squares method used here is that outlined in Emery and Thomson [2003] (Chapter 5.5.1, page 392). This was applied to the current record from each level of the data for every 3.5 day segment, yielding amplitudes and phase lags for the inertial and tidal components at each depth.
The baroclinic currents are primarily composed of tidal and inertial frequency motions which both vary in intensity over the duration of the deployment. The method of signal demodulation is a common tool for estimating the changing amplitude of components over time. The form used here involves least squares fitting sinusoids with the known frequency to sequential segments of the velocity record. When investigating the strength of just a single frequency component it is possible to use very short segments (as low as one period). However when attempting to resolve two frequencies the length of segments must be sufficient to separate the two frequency components by one cycle. It is therefore not be realistic to separate the diurnal and semidiurnal tidal components (M_2 and S_2/N_2) since 14 days would be required. However for these short segments an average (12.21h period) will suffice. However inertial and tidal periods in the Irish Sea differ by 2.8 hours and so require a minimum of 3.3 days to separate. It seemed sensible therefore to use 3.5 days as a segment, since this represents a quarter of a spring - neap cycle. This was also convenient because it was roughly the duration of the observed energetic inertial episodes.
Figure 2.7a/b shows an example of a fit to a period when tidal currents dominated. The black line plotted over the baroclinic current data in pane a shows the position of the observed data plotted in

black in pane b). The total fit plotted as a solid grey line in pane b is composed primarily of the tidal component (dark dashed line) with only a small contribution from the inertial (light dashed line). The quality of the fit to the data for the tidally dominated periods was good because the amplitude varied little over the 3.5 days analysed. However the example presented in figure 2.7b the amplitude of the inertial currents varied significantly over the 3.5 days causing some issues. Figure 2.7b/c shows the fit to a period with strong inertial currents at first but weaker currents toward the end. The fit to the tidal component is significant ($0.1 \mathrm{ms}^{-1}$) despite this being a time of neap tides with weak tidal amplitudes. The reason for this erroneous fit is that the tidal component is being used to destructively interfere with the inertial component in order to reduce the total amplitude for the second half of this segment of data and reduce the variance. The effect on the inertial component is limited since it underestimates the amplitude during the first half but this is compensated for because it overestimates the amplitude later in the data. While this effect is undesirable it is limited to generating a spurious tidal component during short duration strongly inertial events, and during such periods the fit of the tidal component should not be trusted.

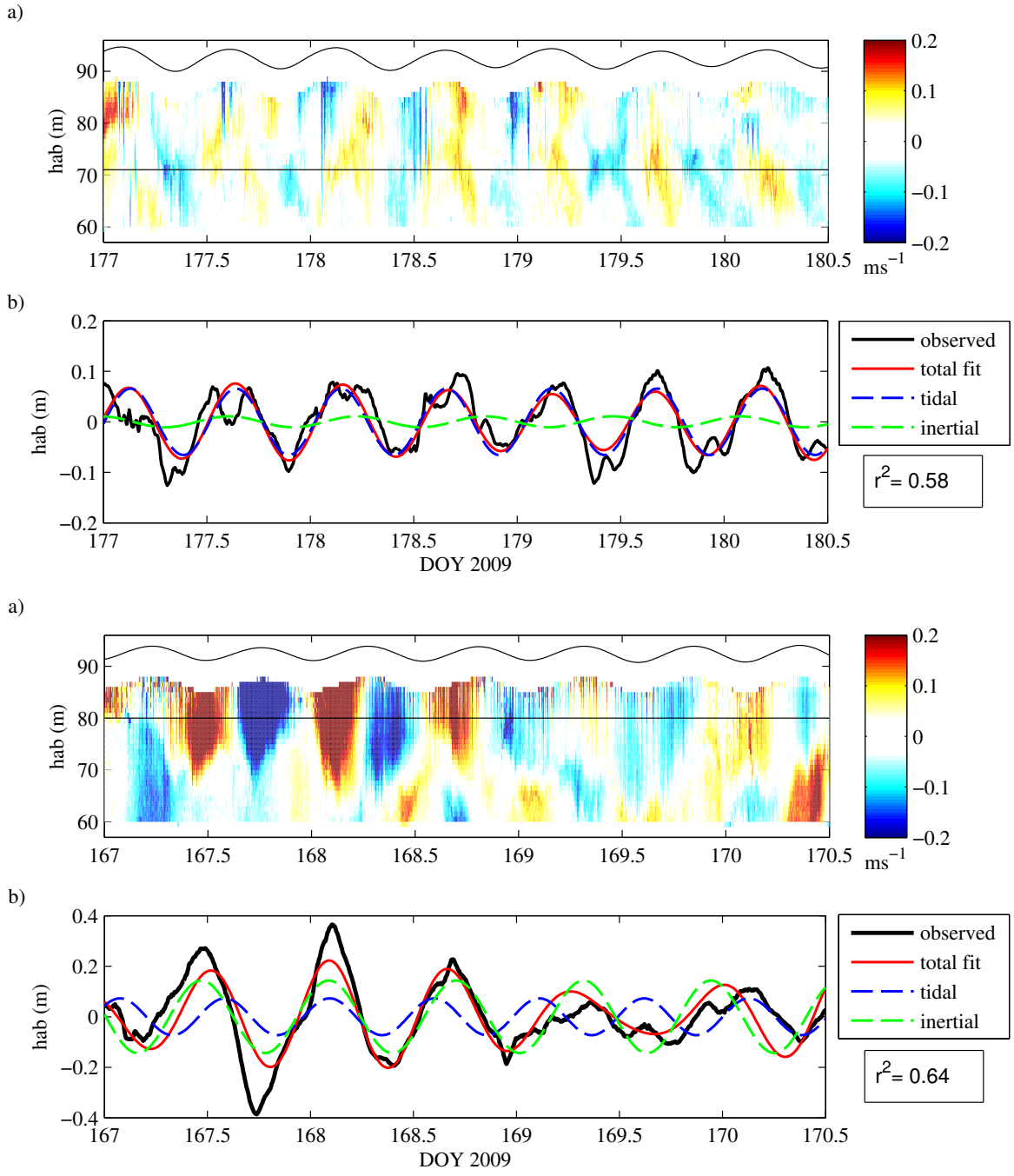

Figure 2.7: a) Plot of the baroclinic currents as a function of depth during a tidally dominated period (a) and inertial dominated (c). The black line plotted over the velocity indicates the height of fit in panes c and d. b & d) Plots of the observed currents from height of black line and the LS fit to the data (red) which is composed of an inertial component (green) and a tidal component (blue).

2.4.9 Bulk shear

Since there was not full water column coverage of the current velocities, bulk shear could not be calculated using velocities separated by half of the water column as in Burchard and Rippeth [2009]. Instead the calculation of bulk shear used takes a mean velocity from the top 5m of the ADCP range to represent surface layer velocities, (u_s and v_s) and the bottom 5m to represent bottom layer velocities (u_s and v_s). These upper and lower layer components were then be used to calculate the shear between the surface and bottom layer velocities using equation 2.11.

$$S_b^2 = \frac{(u_s - u_b)^2}{h_{diff}} + \frac{(v_s - v_b)^2}{h_{diff}} \tag{2.11}$$

Where $h_{diff} =$ is the difference in the mean height above the bed of the layer velocities. Since the ADCP was positioned below the thermocline for most of the deployment the bottom bins of the ADCP (60-65mab) are representative of the velocity of the well mixed bottom layer. However the surface layer was sometimes outside the range of the ADCP during periods when the wind stress was low. This meant that shear during these periods is likely to be underestimated or incorrect.

2.5 Normal modes analysis

Normal mode analysis was used to analyse the form of the internal tidal motions for two different 3.5 day periods over spring tides. The vertical density structure of the water column determines the phase speed and modal structure of these baroclinic motions. In order to determine the theoretical form of the modes, the vertical density gradient was calculated from the temperature profile (see section 2.4.1), and this used to obtain the profile of the buoyancy frequency (equation 1.10). The profile of the buoyancy frequency squared $N^2(z)$ was then utilised in the equation for the complex amplitude of the vertical velocity $\Psi(z)$ [Gill, 1982]:

$$\frac{d^2\Psi}{dz^2} + \left\{ \frac{N^2(z)}{c_p^2} \right\} \Psi = 0 \tag{2.12}$$

with boundary conditions $\Psi = 0$ at the surface $z = -h$ and at the bottom $z = -h$. The eigenvalues of this equation for the first three modes were found numerically using an established numerical code [Klink, 1999], which also calculates the corresponding modal structure $\Psi_n(z)$ for mode n from which the horizontal velocity modal structure $u_n(z)$ is derived. The eigenvalue is the phase velocity c_n of mode n.

2.6 Modeling

A number of different numerical models have been used for the testing of hypotheses to gain a better understanding of the physics involved in the observed dynamical processes.

2.7 Two-layer dynamical model

This simple model is a discretisation of the dynamical equations for the upper and lower layers of the two layer described by Burchard and Rippeth [2009]:

$$\delta_t u_s - \frac{1}{h_s}\tau_s^x + \frac{1}{h_s}\tau_i^x - f v_s = g\delta_x \eta \tag{2.13}$$

$$\delta_t u_b - \frac{1}{h_b}\tau_i^x + \frac{1}{h_b}\tau_b^x - f v_b = g\delta_x \eta \tag{2.14}$$

$$\delta_t v_s - \frac{1}{h_s}\tau_s^y + \frac{1}{h_s}\tau_i^y - f u_s = g\delta_y \eta \tag{2.15}$$

$$\delta_t v_b - \frac{1}{h_s}\tau_i^y + \frac{1}{h_b}\tau_b^y - f u_b = g\delta_y \eta \tag{2.16}$$

$$\tag{2.17}$$

The model was run for the final 10 days of a deployment, a period when spike spikes were observed. Time series of the surface stress components, τ_i^x, τ_i^x were calculated from the met office wind data (equation 2.5), and time series of bottom stress components were calculated from the barotropic velocity components measured by the adcp (equation 2.11). Both time sets were linearly interpolated to 1 minute intervals which was the time-step used to run the model.

2.8 Simpson Bowers model

This simple numerical model calculates a vertical profile of temperature based on the local exchange of heat through the sea surface [Simpson and Bowers, 1984]. The heat is distributed by vertical stirring which is determined by the available power from tidal stresses and from wind stresses. The model was used by the authors to successfully replicate the seasonal cycle of stratification in shelf seas. This was achieved by using seasonally smoothed values for the solar flux, the dew point temperature and the wind speed and a constant level of tidal mixing. For use in replicating the Irish Sea observations the observed tidal stream velocity (from the adcp data) and the met office reanalysis winds were used. These were applied for the period over which data were available. The model was modified to include

internal mixing energy directly at the thermocline in order to simulate mixing by internal waves. The method for this is described in chapter 6

2.9 TC model

This 1D vertical exchange model is that described by Simpson and Sharples [2012] (pages 205-209) and solves the linearised form of the horizontal momentum equations in the form given in equation 1.13. The model employed a Mellor-Yamada 2.2 turbulence closure scheme for relating the turbulent and eddy diffusivities to the shear and stratification. The model was run for a ten day period using a 10 minute time-step. The wind stress applied was calculated from the met office reanalysis data and interpolated to the 10 minute resolution required by the model using a spline method with 20% noise added to the signal to simulate realistic winds. Surface pressure gradients were synthesised so that the baroclinic currents generated matched those from the tidal fit to the barotropic tidal data.

Chapter 3

Observations from the Western Irish Sea 2009

Observations are presented here to give an overview of the meteorology, stratification and mid-water currents for the Irish Sea 2009 dataset. Previous studies from the Irish Sea have presented observations from times when wind driven inertial motions dominate [Rippeth et al., 2009], while others have observed periods when baroclinic tidal currents dominate [Green et al., 2010]. This chapter aims to interpret the 50 day mooring time-series to assess the balance of these processes in the Irish Sea, and identify periods where each mechanism dominates so that they may be investigated in greater detail in later chapters.

3.1 Stratification

On May 19th 2009 when the moorings were deployed from the RV Prince Madog, the water column at the site had already stratified (Fig.3.1a). However the stratification was relatively weak with density increasing almost linearly from the surface to the bed. There was an equal contribution to density from temperature and salinity (Fig.3.1b). On return to the mooring on July 7th there was a warm well mixed 15°C surface layer 15m thick separated from a cool, 11°C, lower layer by a sharp thermocline Fig.3.1c. The temperature contribution to density at this main interface was four times that for salinity alone (Fig.3.1d). Another smaller density gradient was present in the lower 30-40m due to a deep cold salty layer. This lower feature may have been due to the advection of a horizontal density gradient since its appearance and vertical extent varied tidally during the July cruise.

The water column temperature structure, heat content and potential energy anomaly, Φ, are plotted along with the wind speed in figure 3.2. There is a general trend of heating and increasing stratification over the mooring deployment, however the rise is by no means constant. The first two weeks of observation do show a constant increase in heat content and in stratification, but are followed by a sharp drop associated with wind speeds of up to $15 ms^{-1}$ on day 156 when Φ drops by 30%. Wind stress was high over the following two weeks (day 157-175), and while the heat content increased the stratification did not overall. Over the following ten days (175-185) the surface layer warmed from $\sim 14°C$ to $\sim 18°C$ with a doubling in Φ. However the PEA dropped 25% over days 186-187 as high winds returned.

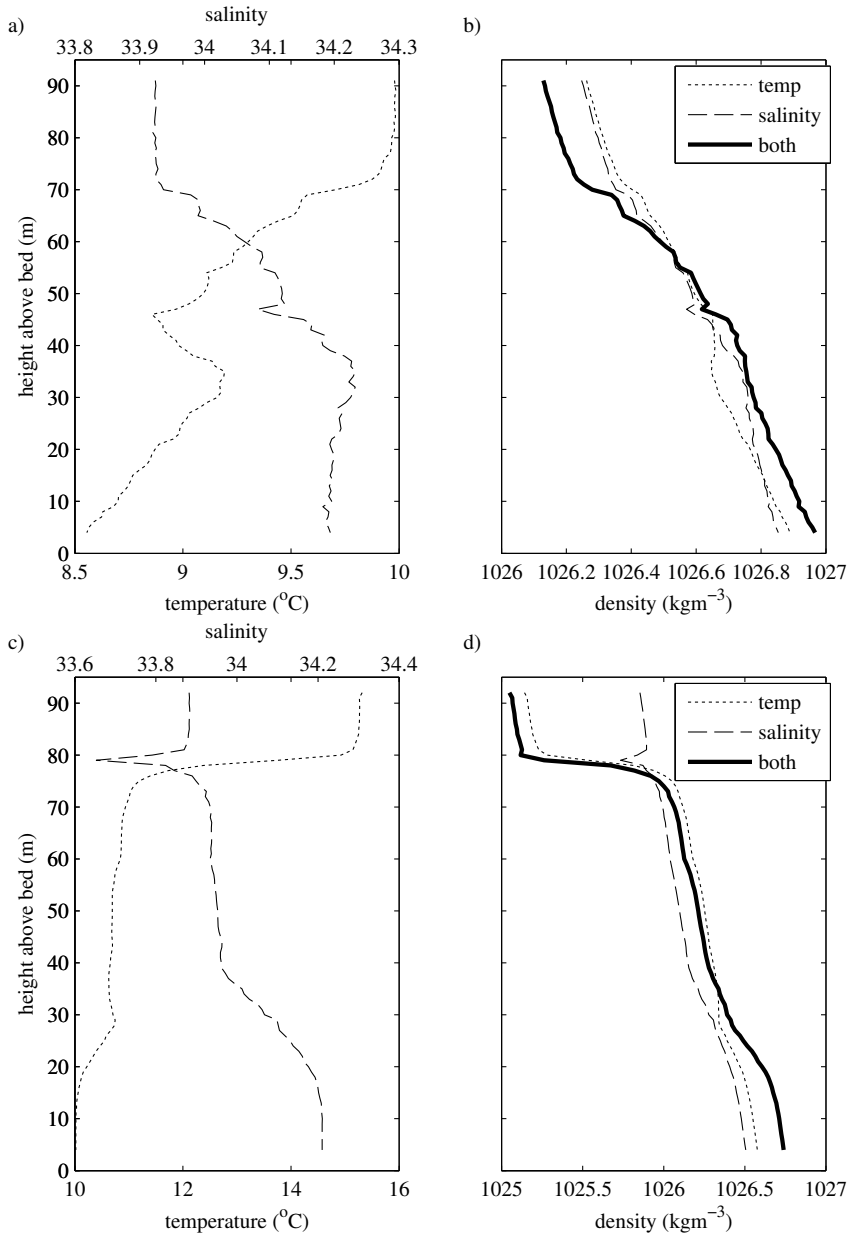

Figure 3.1: a & c) The vertical structure of temperature (dotted line) and salinity (dashed line) measured using a CTD deployed from the RV Prince Madog. b & d) Vertical structure of density calculated for variation in temperature (dotted line), salinity (dashed line) and in both (solid line). Panes a and b show observations from day 138 (19/05/2009), panes c and d from day 187 (09/07/2009).

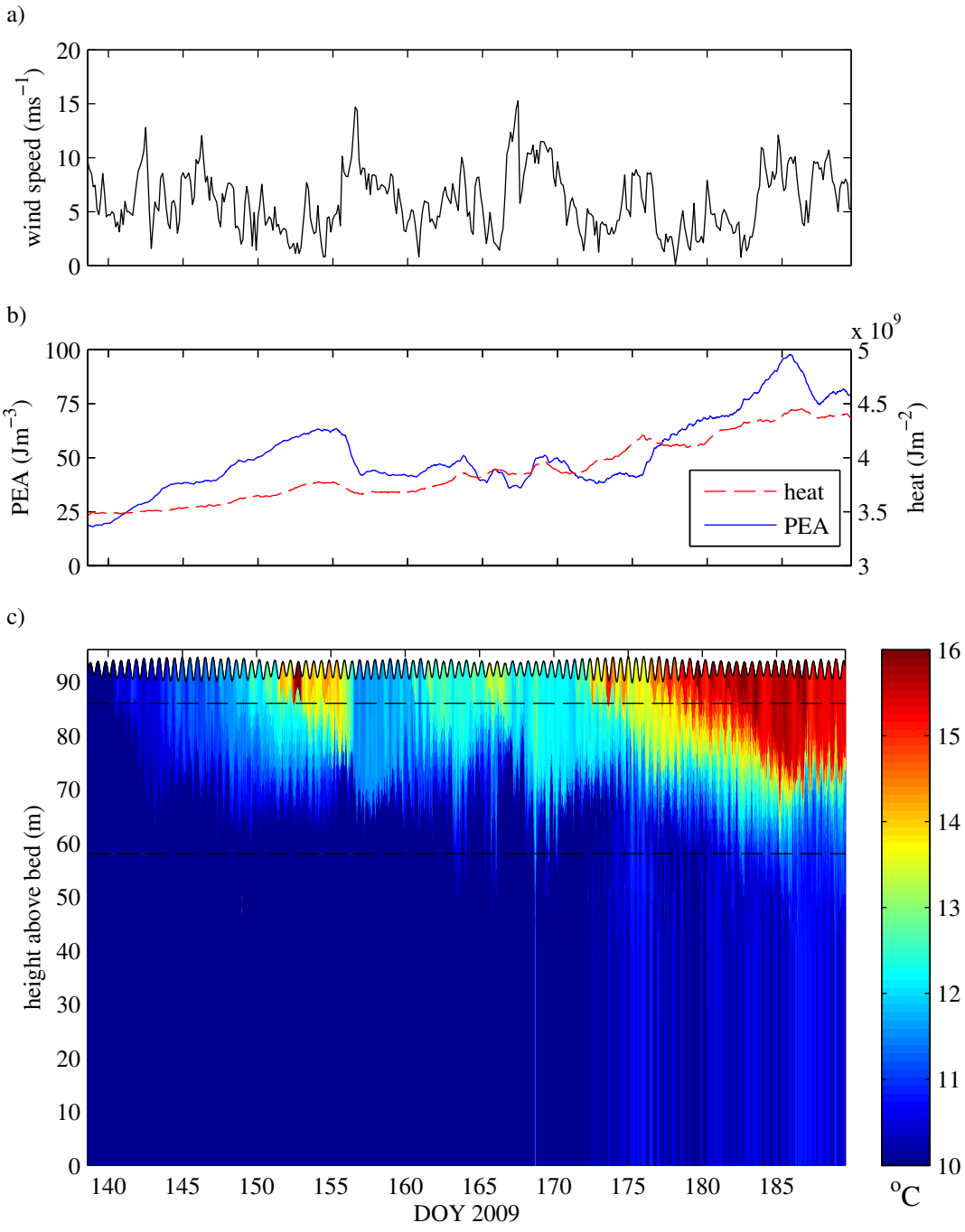

Figure 3.2: a) Wind speed from Met Office reanalysis at the WIS mooring site. b) Potential energy anomaly (blue solid line) and heat content (red dashed line) of the water column calculated from the moored temperature data. c) temperature structure (from mooring) over the period of deployment, May 18th to July 9th.

3.2 Current analysis

The currents measured by the mid-water ADCP are plotted in figure 3.3 which shows that the northerly component is an order of magnitude greater than the easterly. While it is easy to see wind driven currents, close to the surface, in the easterly current plot, they are masked in the northerly plot by the strong barotropic tidal currents. In order to isolate the different processes which provide energy for mixing it is necessary to decompose the raw currents according to those mechanisms which generate them.

It has been assumed that the horizontal currents $u(z,t)$ and $v(z,t)$ are composed of the barotropic tide, $U_{btt}(t)$ and $V_{btt}(t)$, the baroclinic tidal currents, $u_t(z,t)$ and $v_t(z,t)$, and the baroclinic inertial currents, $u_i(z,t)$ and $v_i(z,t)$:

$$u = U_{btt} + u_t + u_i + c_u \tag{3.1}$$
$$v = V_{btt} + v_t + v_i + c_v$$

Here, $c_u(t)$ and $c_v(t)$ represent a time varying component due to residual and advective processes.

The following sections seek to separate these components in order to identify periods where the different processes dominate.

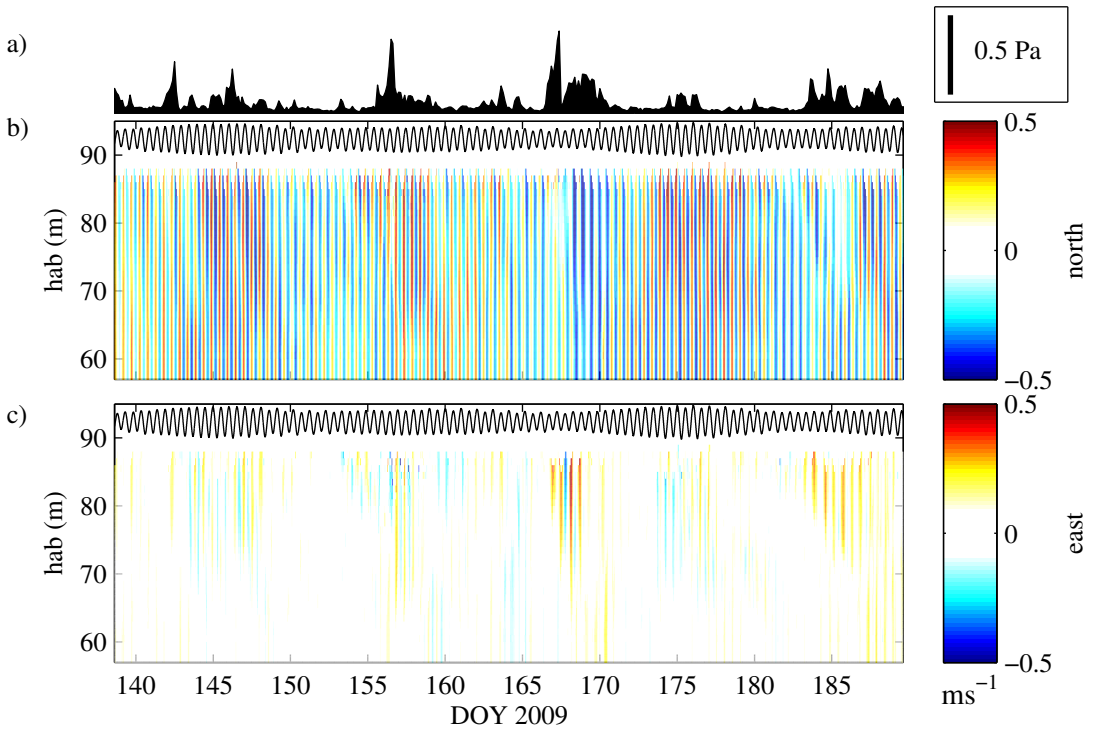

Figure 3.3: Horizontal currents observed in northerly (b) and easterly (c) directions, measured by the mid-water adcp, corrected to height above bed. The wind stress is plotted in pane a, while the position of the sea surface is plotted over the velocities in black.

3.2.1 Barotropic currents

The key frequency components of the barotropic currents were determined by complex spectral analysis. Spectra were calculated for the the complex form of the current, $u + iv$, at each depth level for which there was a complete record (See chapter 2.4.5 for the spectral methods used). A composite depth integrated energy spectra (figure 3.4) is dominated by a peak at semidiurnal frequencies due to the presence of the dominant barotropic tide. An inertial peak is also resolved, with the energy contained in this band two orders of magnitude smaller than the tidal peak. The inertial frequency energy is almost entirely contained in the positive (clockwise) direction of rotation as expected for inertial currents in the northern hemisphere. This is not the case for the semidiurnal frequency currents, where the similar magnitudes of the positive and negative rotating components reflect the rectilinear nature of the barotropic tide. There is also a significant peak in the spectra at M_4 shallow water harmonic, an overtone of the semidiurnal, M_2, tide.

The depth-mean easterly and northerly currents were computed and a complex tidal fit performed by harmonic analysis using the matlab script t-tide [Pawlowicz et al., 2002]. These are plotted with the tidal ellipse in figure 3.5. The fit using 3 harmonic tidal components M_2, S_2 and M_4 captured 88% of the variance. The results of the fits for each component is presented in table 1.1. The principle lunar component, was dominant (M_2 amplitude = 0.32ms^{-1}) however there was a solar contribution (S_2 = 0.06ms^{-1}). The ratio of spring to neap current amplitude was therefore $\sim 3:2$, which can be seen in the current plots in figure 3.5a.

Table 1.1: Result of a complex harmonic fit to the barotropic currents for the main components. Values in brackets is the 95% confidence interval for the characteristic.

constituent	frequency cycles h^{-1}	major axis ms^{-1}	minor axis ms^{-1}	ellipse orientation $^\circ$ from east	phase $^\circ$ from
M2	0.0805	0.32 (0.02)	-0.02 (0.01)	-82.48 (2.82)	312.00 (3.19)
S2	0.0833	0.06 (0.02)	-0.01 (0.01)	-79.96 (15.68)	218.99 (17.94)
M4	0.1610	0.03 (0.01)	-0.00 (0.01)	-45.14 (11.43)	265.96 (12.84)

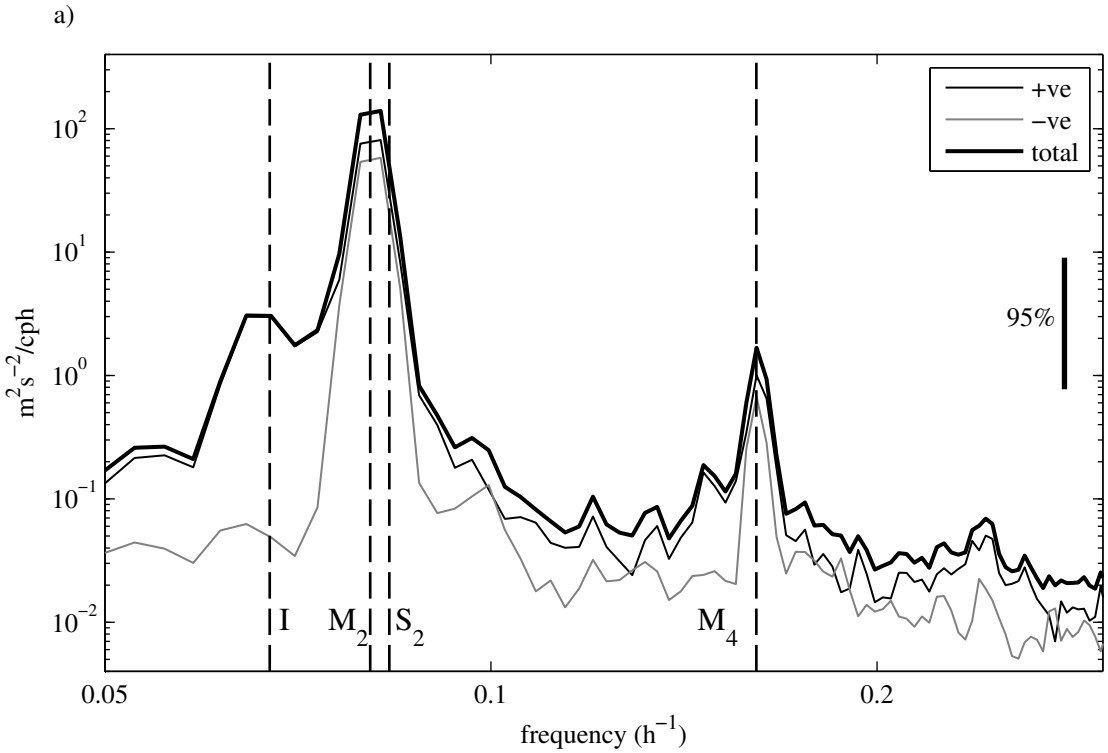

Figure 3.4: a) Complex spectral analysis of the depth mean current velocities shown in fig3.5. The red line shows the clockwise rotating component of the currents, blue is the anticlockwise, while the black line is the total.

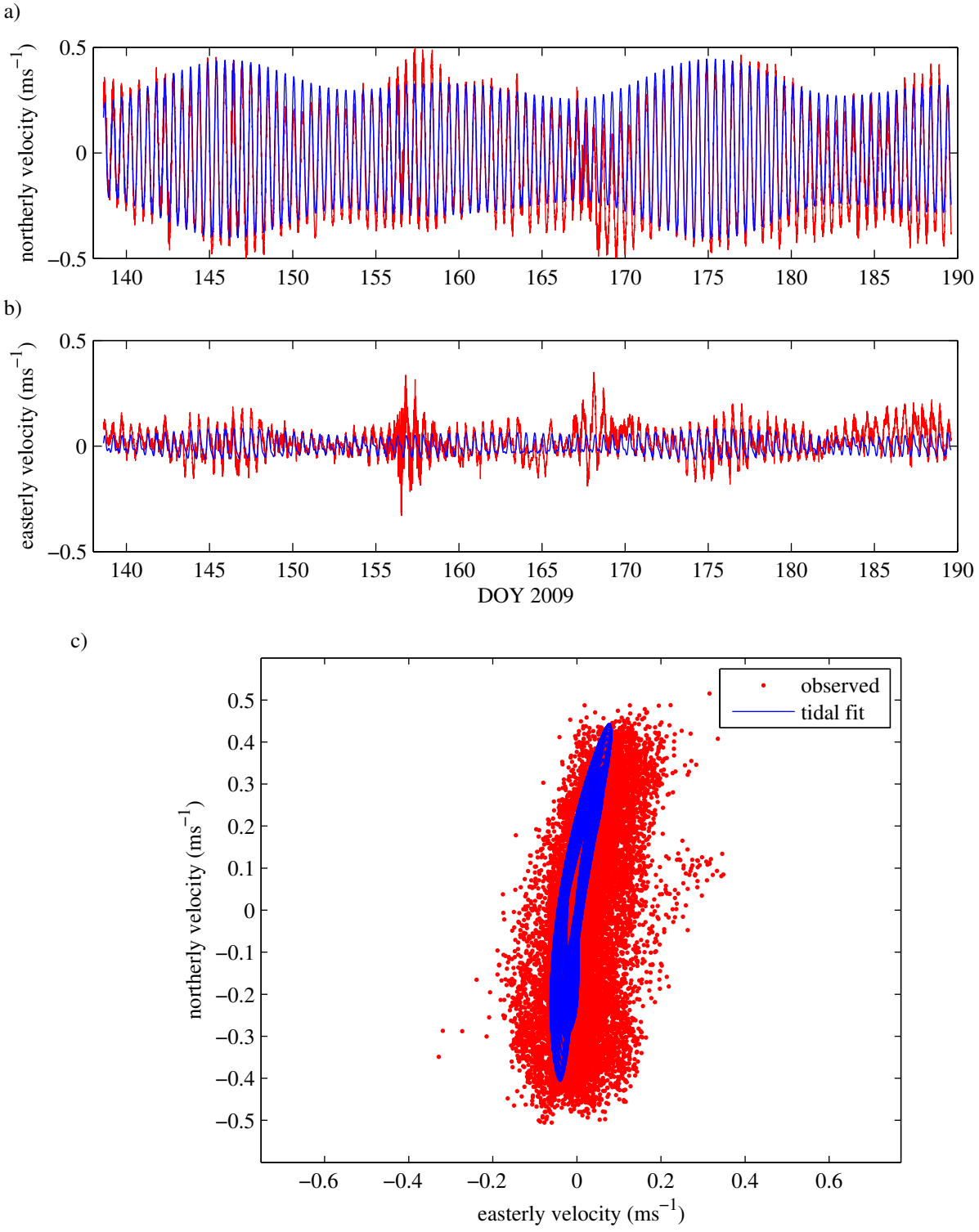

Figure 3.5: Observed northerly (a) and easterly (b) depth average current velocity (red) and tidal fit (blue) for M2, S2, and M4 components. b) plot of the tidal ellipse over the entire deployment generated from a the tidal fit.

3.2.2 Baroclinic currents

The baroclinic currents were calculated by the subtracting an extended profile depth mean from each level of the raw adcp data. This removes the barotropic tide, $U_{(bt)}$ and $V_{(bt)}$ as well as any depth mean residual component, c_u and c_v. The remaining currents are considered to be the best estimate of the baroclinic currents and are presented in figure 3.6 with northerly and easterly currents plotted for the entire deployment along with wind stress which is plotted in panel a. Peak velocities of up to 0.4ms^{-1} are seen in the surface layer and occur at times of high wind stress, e.g. days 156, 167 and 185. The energetic wind driven events last for several days and appear, first close to the surface, before penetrating deeper. Tidal range can be seen from the plot of surface height above the current data and indicate that during spring tides elevated baroclinic currents of 0.1-0.2ms^{-1} are observed. e.g. days 162 and 175. The least energetic periods are seen around neap tides when wind stress is low, e.g around days 152 and 172.

A complex spectral analysis of the baroclinic currents is plotted in figure 3.7 as a function of depth (details of spectra in chapter 2.4.5). There are strong energy bands at inertial and semidiurnal tidal frequencies, and both exhibit a two layer structure with a minimum at a depth of $\sim$68mab. The inertial band has about 50% more energy than the tidal with most of the energy contained in the top 20m (above 78mab). The spectra show that, as in the barotropic spectra, inertial currents exist only in the clockwise direction. The baroclinic tidal currents are also dominated by clockwise rotation, showing that they are not rectilinear in contrast to the barotropic tide.

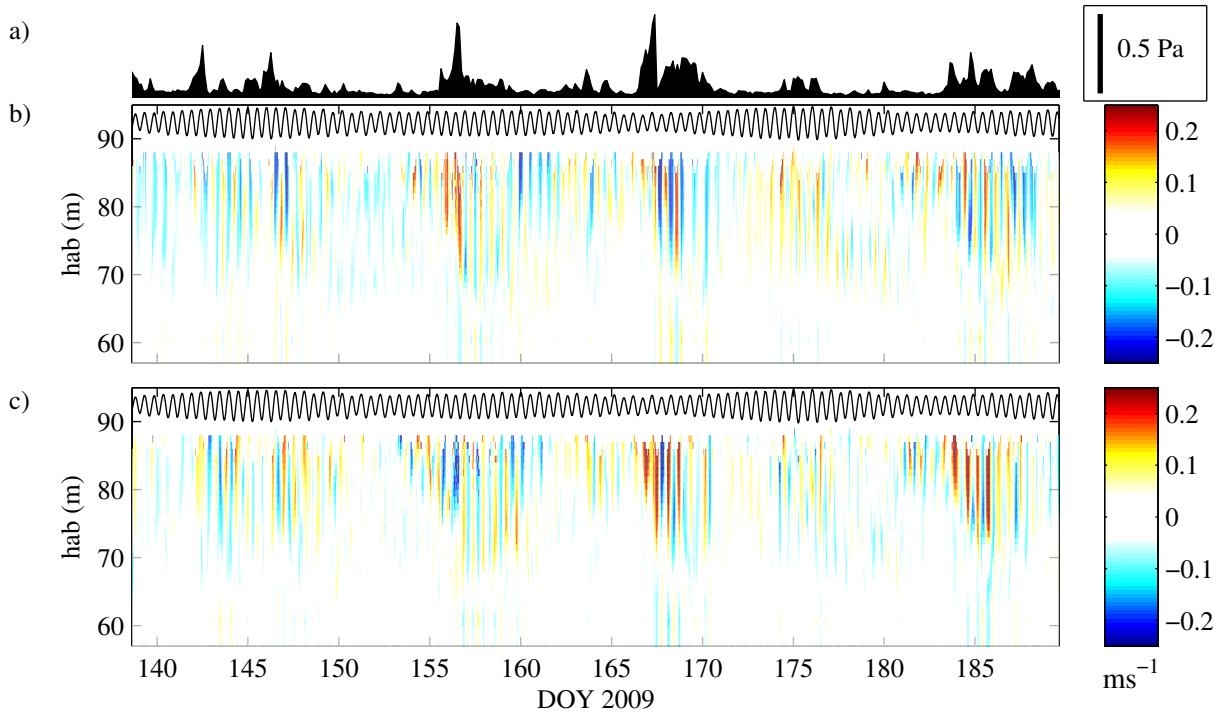

Figure 3.6: Northerly (b) and easterly (c) baroclinic current velocities calculated by subtracting the depth mean of the extended profile from each level of the raw currents measured by the mid-water adcp. Wind stress is plotted in pane a to illustrate that the strongest baroclinic currents are observed at times of high wind stress. Sea surface height is also plotted on the current data to show that elevated velocities occur around spring tides.

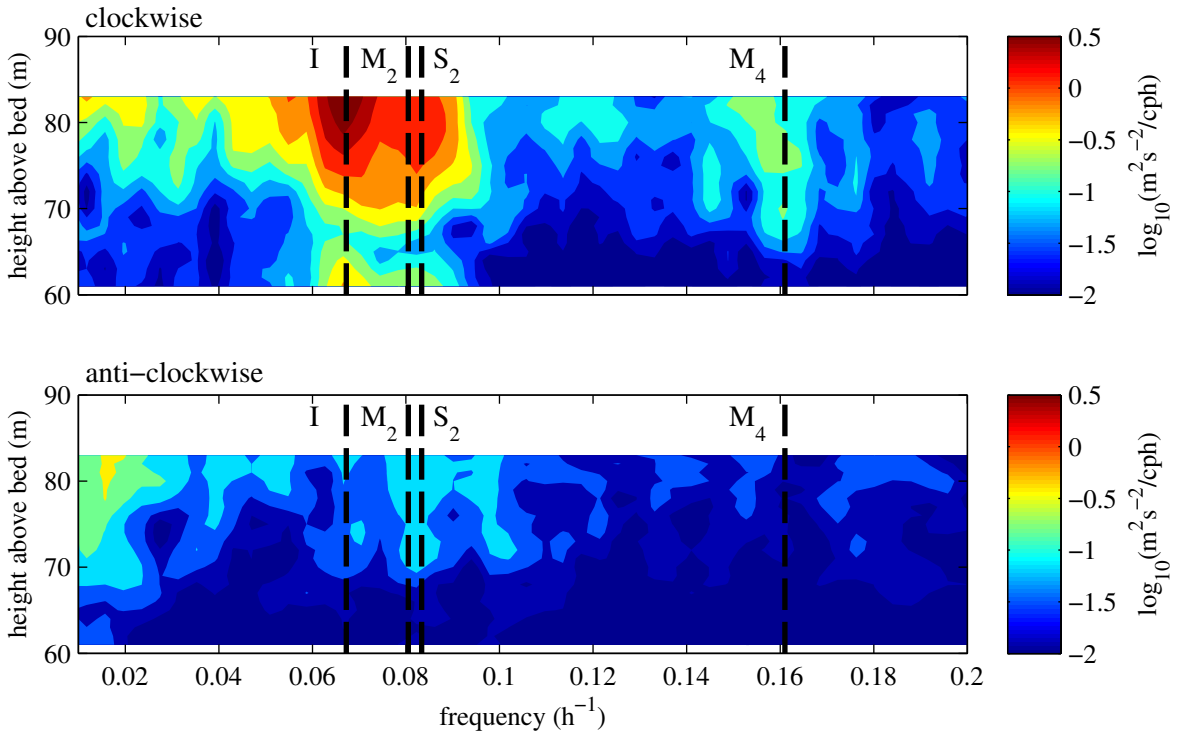

Figure 3.7: Complex spectra of baroclinic currents as a function of depth. a) clockwise components and b) anticlockwise components. Vertical dashed lines indicate the frequency of the Inertial component, I , semidiurnal tidal components, M_2 and S_2, and the tidal overtone M_4.

In order to isolate the inertial currents, efforts were made to remove the baroclinic tide. However, a least squares harmonic fit performed on the entire data set using M_2 and S_2 constituents captured very little of the observed variance during the tidally dominated periods. The reason for this was that the baroclinic tidal currents do not stay in phase with the barotropic tide through the observations. In order to resolve this issue the time series was demodulated by breaking the current record into shorter sections. The Rayleigh criterion states that the separation of two constituents f_m and f_R requires a record length T which satisfies, $|f_m - f_R|T > 1$, i.e. having started in phase two such constituents would be separated by at least one full period. The record length which satisfies this criterion for inertial and semidiurnal tidal (M_2 S_2 average = 12.21h) constituents in the Irish Sea is 2.8 days. However 3.5 day periods were chosen for the segments since it represents a quarter of a spring-neap cycle. The rapidly changing amplitude of the inertial component caused some error in the tidal fit at such times and as such tidal fits during periods of strong inertial motions are considered to be suspect. The 3.5 day sections of velocity data were fitted at each depth level with inertial and semidiurnal tidal frequency sinusoids to determine the signals variability. The result of these fits is a vertical profile of an amplitude and phase lag for inertial and tidal frequencies. These profiles are plotted below the relevant section of baroclinic velocity for northerly and easterly directions (fig 3.8 to 3.9). Each segment has been labeled with a letter (H to P) in order to aid identification. Wind stress and sea surface height are also plotted so as to indicate the forcing for the two processes. Depth mean coefficient of determination, R^2, values for each profile are given above the profiles themselves.

The interpretation of the first half of the deployment is complicated by the timing of the two processes. Periods of strong wind driven currents coincided with spring tides leading to energetic periods with strong baroclinic currents of 0.3ms^{-1}. Separating these were periods of low wind stress and neap tides where currents did not generally exceed 0.05ms^{-1}. The second half of the deployment (segments H to P figures 3.8 and 3.9) is more useful for examining the two processes separately. Two periods of high wind stress (segments J and P) occurred during neap tides while, wind stress was low during the period of spring tides which occurred in between these (segments L and M). For this reason further analysis focuses on this later half of the deployment, starting with a detailed look at the evolution of the inertial and tidal fits.

Section H occurs during neap tides and there is almost no tidal energy in the fit. There is moderate wind stress of 0.1Pa generating currents of up to $0.05ms^{-1}$ in the surface layer. These currents decrease from the surface down to a minimum at 73mab before increasing slightly below this depth. The phase lag in the inertial period currents, plotted below, shows that surface and bottom layers each have a uniform phase with the layers opposing each other by $\sim 180^{\circ}$. This is in agreement with the two layer structure displayed by the amplitudes. The following section, J, has a similar two-layer

structure, however, the current magnitude is greater, in the surface layer as the wind stress peaks on day 167 and remains high throughout this period. The lower layer has also increased in magnitude to 0.05ms^{-1} while the nodal point has descended to ~ 67mab. The tidal currents during this period have exactly the same structure as the inertial but are about a third as strong but are likely to be an artifact of the fit due to the rapidly changing amplitude of the inertial at this time.

Currents during section K are small with low wind stress and continuing weak tides. Section L falls directly over a period of spring tides and this is reflected in large tidal fit amplitudes (up to 0.1ms^{-1}), which form a two-layer form similar to that in Section J with a node at 67mab. The low wind stress at this time generated only weak inertial currents above 75mab. The subsequent section of data, M is wind free and although still dominated by tidal currents, the vertical structure has changed to three layered. Maximum tidal amplitude occurs around 70mab with a middle layer $\sim 10-15$m thick which is 180° out of phase with the surface and bottom layers. Section N contained significant tidal currents above 70mab despite relatively small tides and a two layered structure. On the last day of this section the wind stress increases and generates inertial currents up to 0.1ms^{-1} above 80mab. Section P sees this inertial event strengthen and deepen as a two layer structure develop with a uniform upper layer with 0.12ms^{-1} amplitude with amplitudes of 0.04ms^{-1} below 70mab in a form. This current structure is very similar in structure and magnitude to the high wind stress section J.

These average snapshots of the vertical structure do reveal an interesting shift in dominance between the two processes. The final three weeks of the deployment show two short periods of inertial currents and a week long period of tidal domination.

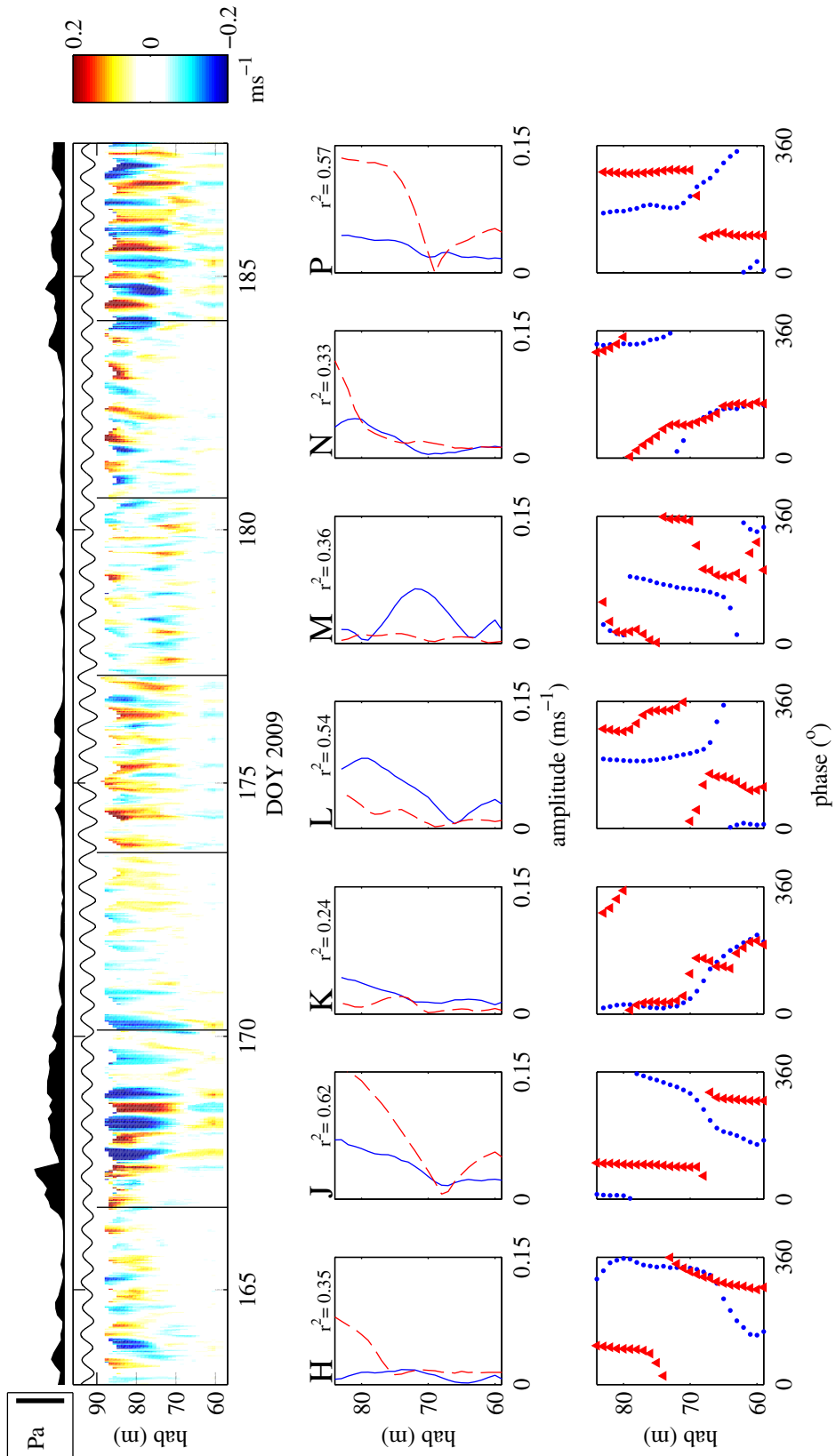

Figure 3.8: Least squares fits of tidal and inertial components for the northerly baroclinic currents for the second half of the deployment. a) wind stress. (b) easterly baroclinic currents. The amplitudes (c) and phase lags (d) of least squares fits are plotted below the respective sections of the velocity data, with the for the inertial component (14.9h) in red (dashed line & triangles) and tidal component (12.21h)in blue (solid line and dots). The mean R squared value is given for each segment.

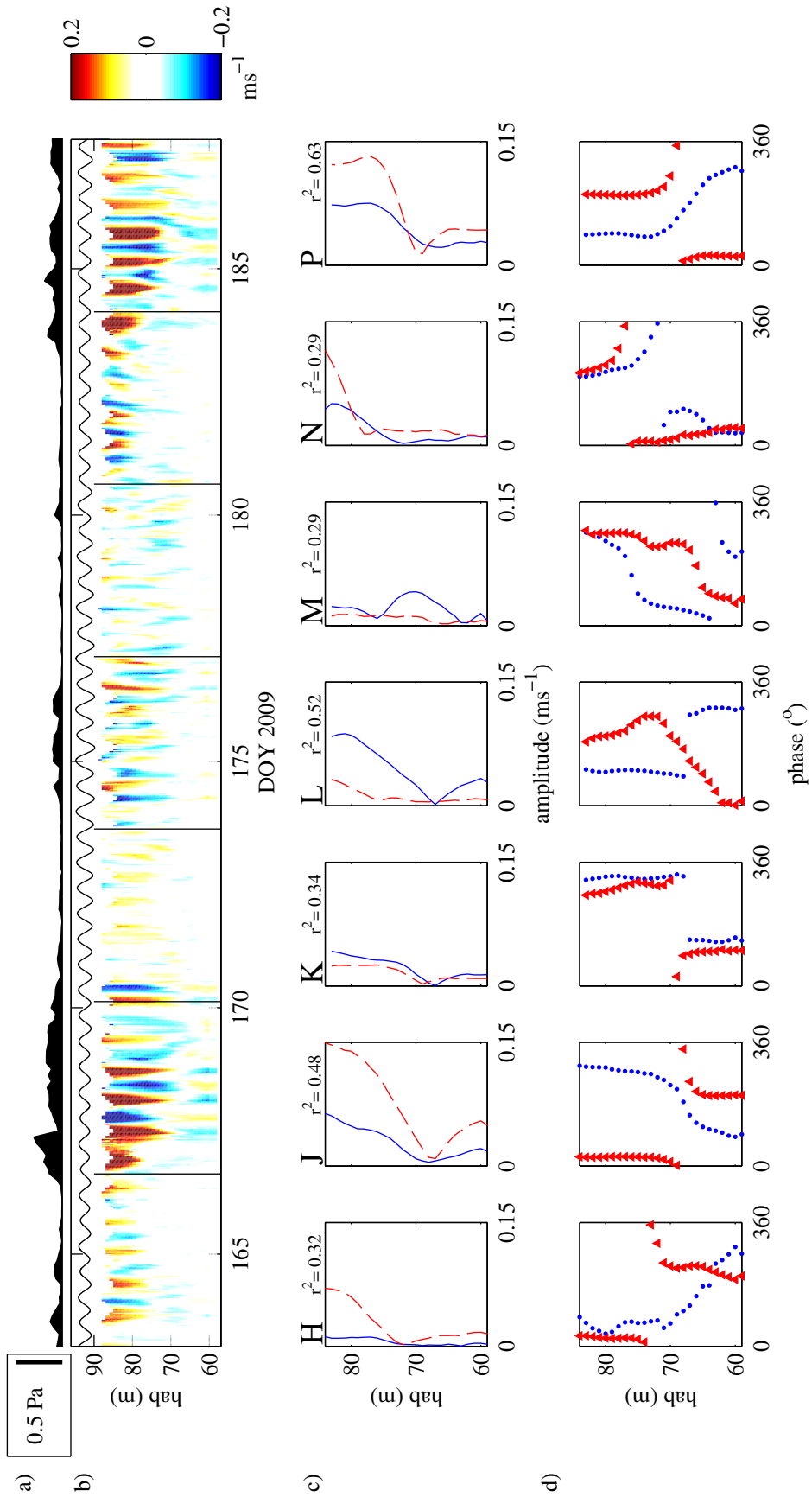

Figure 3.9: Least squares fits of tidal and inertial components for the easterly baroclinic currents for the second half of the deployment. a) wind stress. (b) easterly baroclinic currents. The amplitudes (c) and phase lags (d) of least squares fits are plotted below the respective sections of the velocity data, with the for the inertial component (14.9h) in red (dashed line & triangles) and tidal component (12.21h)in blue (solid line and dots). The mean R squared value is given for each segment.

3.3 Bulk shear

The periods of energetic inertial and tidal currents generate shear across the thermocline which may be represented as a bulk shear vector. Surface layer velocity (u_s and v_s) and bottom layer velocity (u_b and v_b) components have been calculated using the ranges 80-88mab and 60-65mab respectively (plotted on figure 3.10). These layer velocities are then used to calculate the bulk shear vector S_b^2, using equation 2.11. S_b^2 represents the square of the total shear across the thermocline and has not been scaled by the distance h between the the heights of the two layers. In figure 3.10 the magnitude and direction of S_b^2 are plotted below the wind stress and tidal range.

3.3.1 Bulk shear magnitude

Peak values of over $\mathrm{S_b^2} = 2 \times 10^{-4}\mathrm{s}^{-2}$ ($0.3\mathrm{ms}^{-1}$ shear) occurred at times of high wind stress, with magnitudes three times those observed during tidally dominated periods. The wind driven shear peaks were equivalent in magnitude to those observed in the North Sea [Burchard and Rippeth, 2009] and larger than those previously observed in the Irish Sea [Rippeth et al., 2009]. The magnitude of S_b^2 was highly oscillatory throughout the time series, particularly during the inertial events, often dropping close to zero before rising again in a series of bulk shear spikes like those described by Burchard and Rippeth [2009]. However, like the inertially dominated periods these shear spike episodes were not persistent, lasting only a few days. Two clear examples of inertial shear spiking were apparent and were the most energetic baroclinic events in the time series. Both periods of spiking occurred in the later half of the deployment when stratification was well established and have been labeled on figure 3.10 as periods P1 (days 165 to 172) and P2 (days 180 to 190). In the next chapter these two wind driven episodes will be investigated in greater detail.

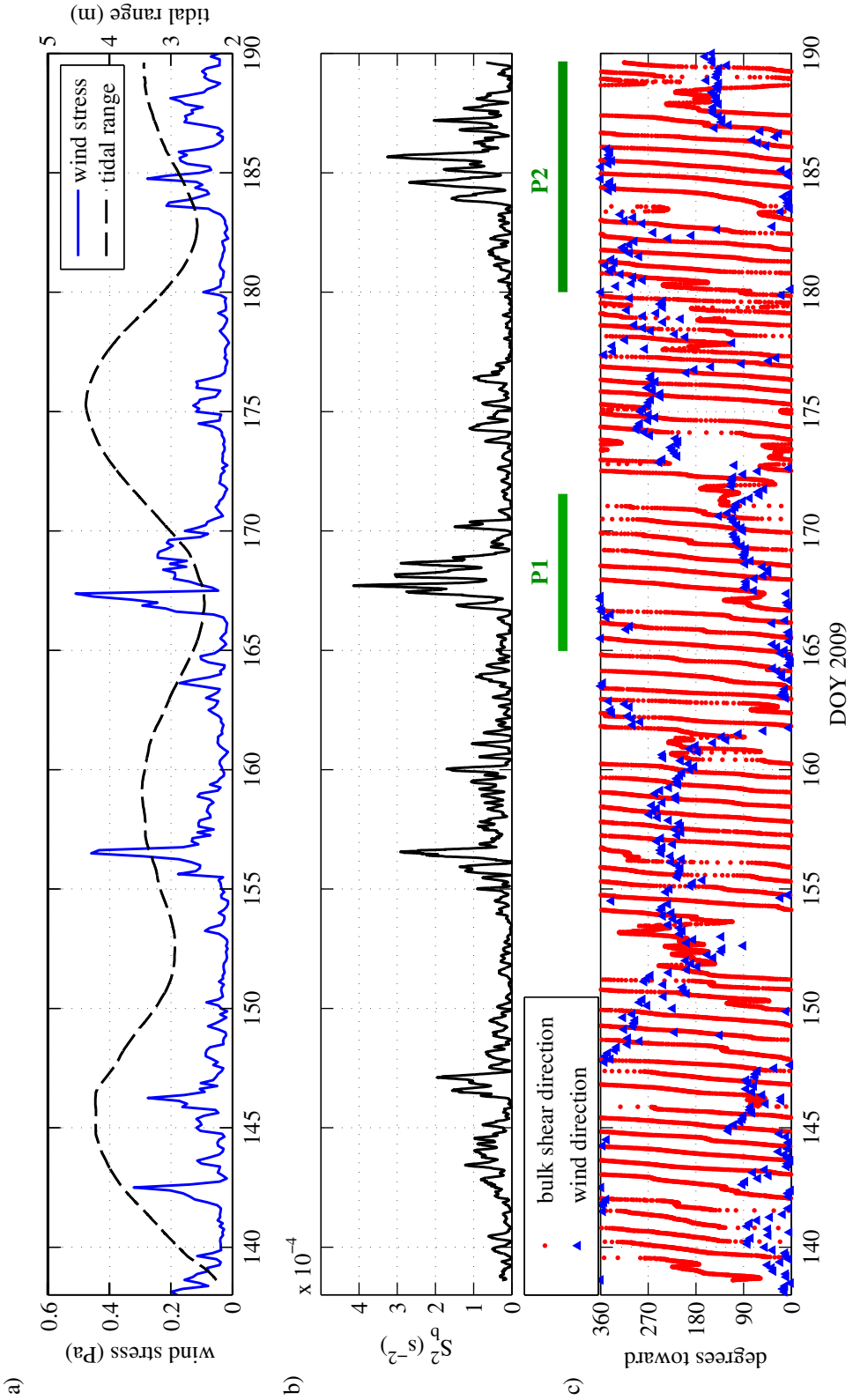

Figure 3.10: Mooring data showing bulk shear over the entire mooring deployment. a) Wind stress from met office reanalysis (solid line) and tidal amplitude from bed mounted pressure recorder (dashed line). b) Magnitude of bulk shear squared, S_b^2, calculated from mean velocity above (80 to 88mab) and below the thermocline (60 to 65mab) using a 2h moving average. c) Direction of bulk shear vector (red dots) and wind stress (blue triangles). The lines, between panes b and c, marked P1 and P2 indicate the two periods of shear spiking presented in detail.

3.3.2 Bulk shear rotation

The direction of shear plotted against time can be a useful indication of the shear generating processes through its slope. For example, the slope of an inertial shear rotation is such that it will take 14.87 hours to pass through 360° rather than 12.42 hours for a tidally rotating vector. The direction of the shear vector is plotted, for the second half of the deployment in figure 3.11 with the segment letters from figures 3.8 and 3.9 added for reference.

Rotation of the shear vector is not continuous instead it rotates clockwise for several days before halting, sometimes reversing, before resuming clockwise rotation. To establish which process is dominating during these periods of vector rotation, the vector direction has been plotted twice, the upper plot (pane b) has a theoretical inertial rotation overlaid, while (pane c) has a theoretical tidal rotation overlaid. The theoretical slopes have only been overlaid during periods of consistent rotation and the phasing has been set to the start of each. The evolution of the shear vector rotation appears closely linked to the forcing processes as revealed in the least squares fits.

- Strong wind forcing on day 167 starts 4 days of shear vector rotation which tracks the theoretical inertial slope closely. The tidal slope is too steep to match the observations and rotates a full 360° too far by day 171. The least squares fit from this time (section J) reveals strong inertial currents.

- The quiescent period K is accompanied by a loss of shear rotation before a new period of rotation commences on day 174. Despite a moderate increase in wind stress at this time the shear vector more closely tracks the tidal slope suggesting that the large spring tides were responsible for generating shear at this time.

- Segment M has no consistent rotation of the shear vector, which at first seems surprising since it is the period when tidal currents were found to be at their peak. The reason for this is the three layer vertical velocity structure which is seen in the least squares fit, where top and bottom 5m are in phase and of similar magnitude. This means that the shear between these layers is not significant despite the large shear between them and the energetic middle layer. If the shear is instead calculated across the middle layer, then the rotation during this period is tidal too (see figure 3.12). When the tidal motions become two layered again during section N, the shear vector rotates once again at a tidal rate.

- On day 183 the wind stress increases and rotation is lost before restarting before four days of rotation begin. Segment P behaves in the same way as section J with the slope matching the inertial slope for six rotations before it is lost again.

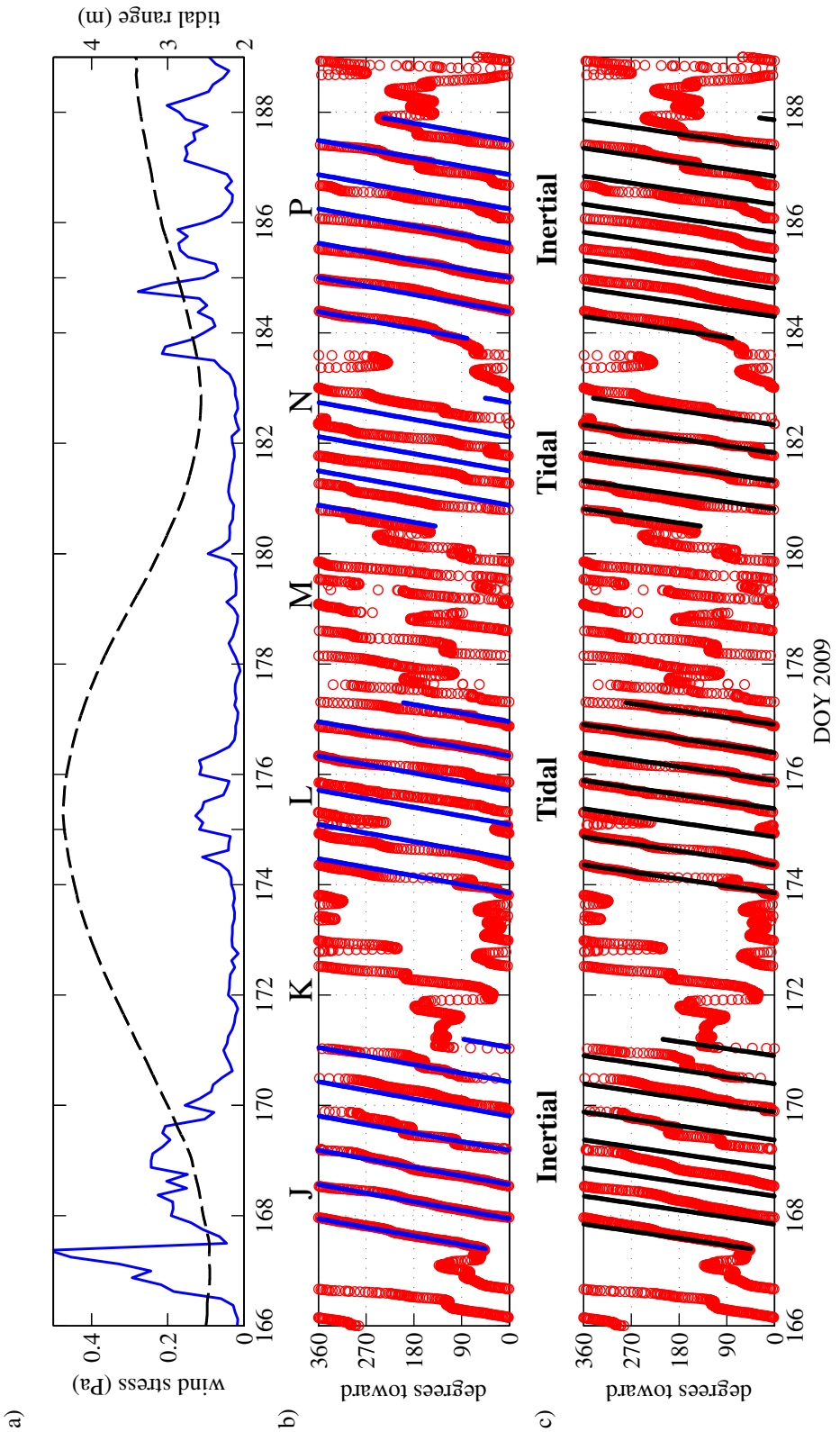

Figure 3.11: Bulk shear vector direction plotted for days 166-189 (relates to segments J to P). a) wind stress (black) and tidal range (blue), b) observed bulk shear direction (red circles) with a pure inertial rotation overlaid (blue dots) b) observed bulk shear direction (red circles) with a pure M2 tidal rotation overlaid (black dots).

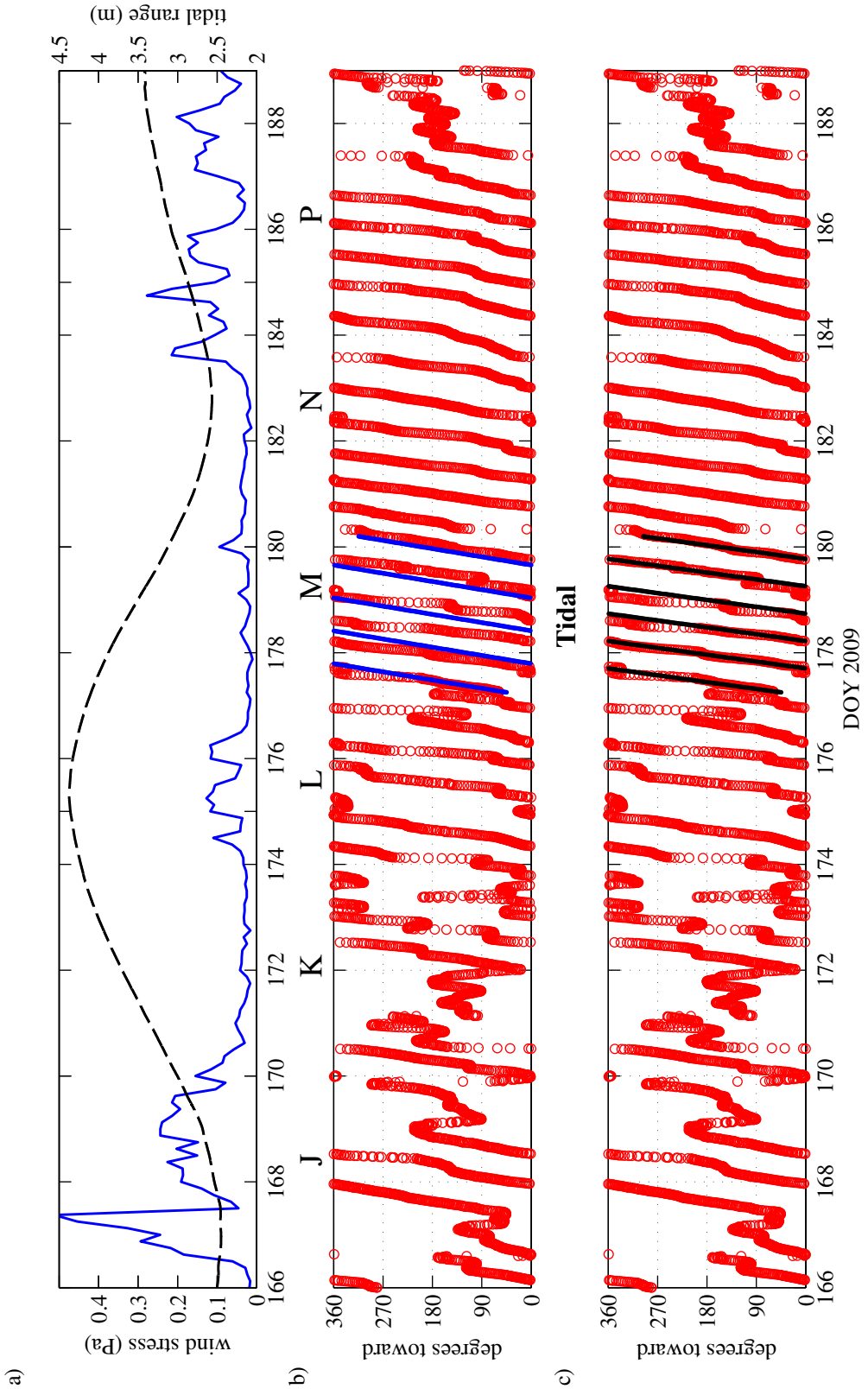

Figure 3.12: Bulk shear vector direction showing period when 3 layer tidal shear dominates. a) wind stress (black) and tidal range (blue), b) observed bulk shear direction (red circles) with a pure inertial rotation overlaid (blue dots) b) observed bulk shear direction (red circles) with a pure M2 tidal rotation overlaid (black dots).

3.4 Summary

- Moored data from the Irish Sea for 51 days in spring time showed a trend of strong surface heating and increasing stratification punctuated by wind mixing events.
- Several high wind stress episodes were observed and generated strong inertial currents which persisted for several days before dying out.
- The vertical structure of inertial currents was strongly two layered, with velocities of up to 0.3ms^{-1} in the upper layer, three times the magnitude of those in the lower layer.
- Baroclinic tidal currents of up to 0.1ms^{-1} were observed during periods of low wind stress with greatest magnitude around spring tides.
- The vertical structure of the barotropic tide evolved from 2 to 3 layered over the period of peak current velocities.
- The dominant mechanism for shear generation across the thermocline switched several times during the time-series with periods of high wind stress generating strong inertial shear and tidal shear dominating during quiescent periods.
- During the latter half of the deployment there is good separation of the two mechanisms of shear production providing an opportunity to examine each process in isolation.

Chapter 4

Inertial Shear Spikes

This chapter investigates the shear spikes observed during the wind driven episodes identified in chapter 3. The first part aims to interpret the dynamics during these events in terms of the wind forcing and bulk shear and then to examine their effect on stratification and mixing. The second half of the chapter then seeks to reproduce the shear spike observations using two different models. The aim of the modelling is to test whether the existing physics contained in the models is sufficient to describe the observed dynamics and mixing generated by shear spiking events.

4.1 Period P1: days 165 to 172

This was the first prolonged period of significant shear spiking observed during the deployment. It occurred during the second half of June when a frontal jet associated with the passage of a front brought the highest wind stress of the entire deployment and was accompanied by neap tides. The wind stress magnitude and tidal range are plotted in figure 4.1 along with the total magnitude of the baroclinic velocity with isotherms overlaid, below these are the S_b^2 magnitude, direction along and the wind direction.

The vertical density structure at the beginning of this period was diffuse with stratification extending right to the surface and a thermocline thickness of $\sim 30m$. Weak currents observed in the surface layer were inertial in frequency (see section J for fits, figures 3.8/3.9) with a small tidal range, no baroclinic tidal currents were observed. Although S_b^2 was low throughout day 165 and into day 166 the shear vector rotated at an inertial frequency. However during the second half of day 166 wind stress rose rapidly, generating a surface layer velocity of 0.3ms^{-1} with S_b^2 rising to a peak of magnitude $3 \times 10^{-4}\text{s}^{-2}$. Simultaneously the shear vector jumped from 120° anticlockwise to 10° aligning itself with the wind direction (toward the north).

After this initial impulse the shear vector initially rotated clockwise but on day 167 it reversed as the wind strength increased. This slowed the surface layer oscillation before driving it once again to in the direction of the wind. The shear magnitude declined and to roughly a quarter of its maximum value during the counter rotation. However as the shear vector became aligned with the wind again (spike 2) the surface layer was accelerated and shear generated with S_b^2 peaking at a level slightly above the first spike.

Spike 2 receded initially, but little shear was lost before the shear increased again and formed largest shear spike in the entire deployment. This is interesting because it was not correlated with an increase in the wind stress, which had actually reduced considerably by this time. Instead it was a change in the wind direction which appears to have generated this third and largest spike to form at a time of relatively low wind stress with the wind veering from north (0°) to east (90°). The result was that, rather than opposing the surface current and reducing the shear, the wind accelerated the surface layer increasing shear from its already elevated level.

After the shift in direction on day 167, the wind continued to blow toward the east for several days. The shear vector rotated through 360° at the inertial frequency throughout and a series of shear spikes are generated once every rotation (spikes 4 to 8). Each time the wind stress vector aligned with the bulk shear vector shear was generated. Gradually the spikes reduced in magnitude and the rotation of the shear vector stopped on day 171 when low wind stress had S_b^2 had fallen close to zero and there

remained only weak currents in the surface layer.

During period P1 there were significant changes in the stratification which are obvious in the isotherms plotted in pane b. The diffuse vertical density structure observed initially changed as soon as the wind stress increases. The isotherms converge with the lower ones rising to meet the upper ones. There were several jumps in the height of the thermocline over the following days, with periods of elevated S_b^2 corresponding to a depressed thermocline. However the general trend over this period was one of deepening the mixed layer, with the base of the mixed layer descending from less than 10m initially down to 20m below the surface . Despite this deepening the surface layer did not cool, in fact there appears to be no heat loss during this period and little change to Φ (see figure 3.2).

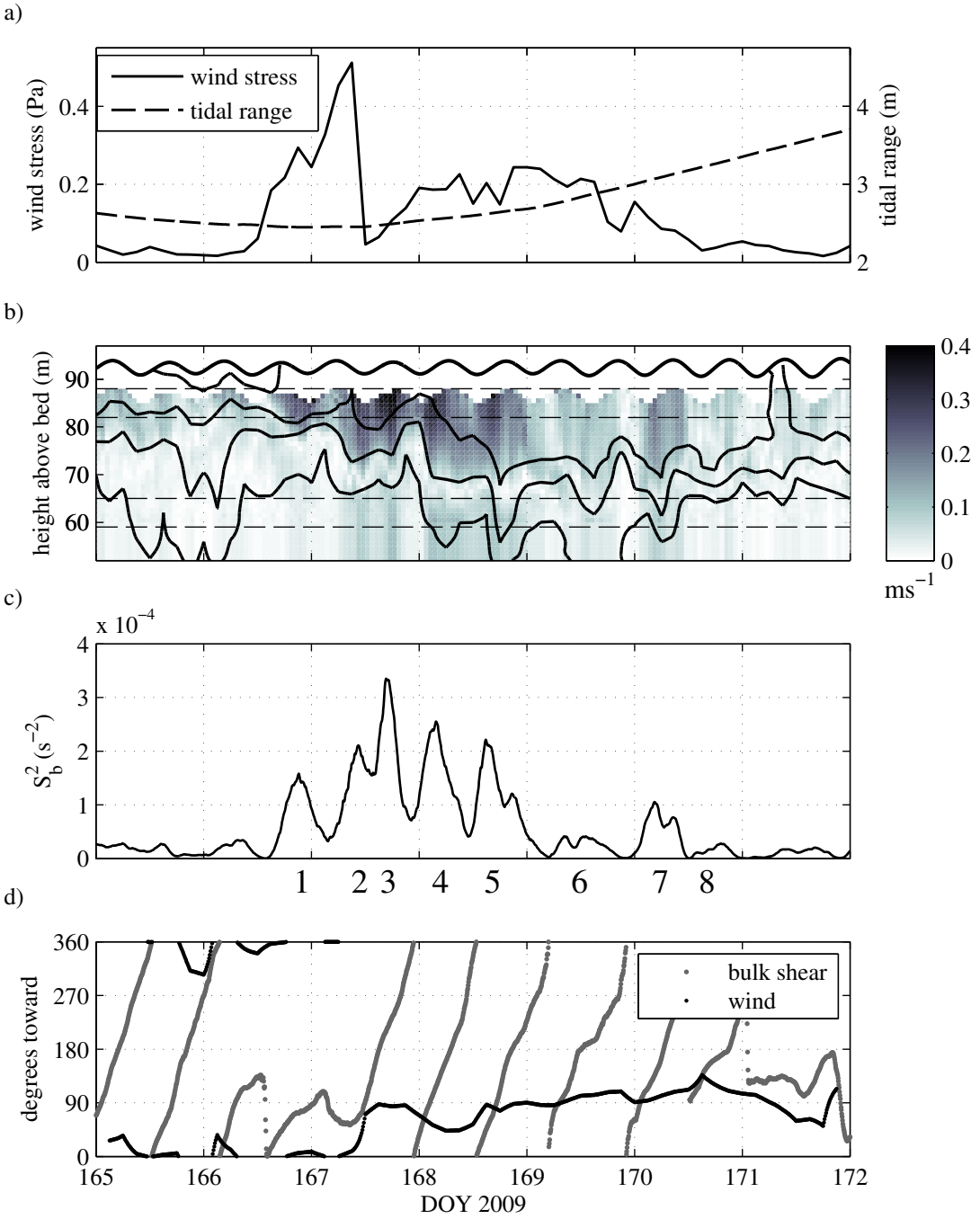

Figure 4.1: Bulk shear analysis from period P1. a) Wind stress calculated from Met Office 3h reanalysis wind(solid line), tidal amplitude (dashed line) b) Magnitude of mid-water velocity with temperature contours (10, 11, 12, 13 °C) overlaid. c) Magnitude of bulk shear squared, S_b^2, calculated from 2h moving average mean velocity above (80 to 88mab) and below the thermocline (60 to 65mab) (dashed lines on pane b indicate ranges). d) Direction of S_b^2 (light dots) and wind stress (dark triangles). Spikes have been numbered for reference in the text.

4.2 Period P2: days 180 to 190

The second period of inertial shear spiking occurred during the final week of the mooring deployment. The mooring recovery cruise took place on the final two days of P2 and so additional analysis is presented for this period in the form of surface layer motion plots, gradient Richardson number calculations and dissipation observations.

4.2.1 Shear spikes

Bulk shear spikes and met data are presented in figure 4.2 for period P2. The observed wind data is also plotted and shows the period covered by the mooring recovery cruise.

There was moderate shear during the first three days, with baroclinic currents primarily of tidal frequency (see section J for fits, figures 3.8 and 3.8). During this time the shear vector rotated at the tidal frequency (see figure 3.11) while wind stress was low.

Midway through day 183 the wind stress increased rapidly and the shear vector jumped (180°) to a direction roughly (45°) to the right of the wind (see 1st spike). S_b^2 rapidly grew to produce the first shear spike at the end of day 183. This was the start of three days where the shear vector rotated at the inertial frequency. The wind continued to blow towards the north through days 184 and 185 producing 3 more shear spikes with each spike produced when the wind and shear vectors aligned (spikes 2-4). Spike 4 was the largest despite wind stress which was half the peak magnitude. This was due to a drop in the wind stress during spike 3 which left some residual shear as less energy was removed from the surface layer than had been added during spike generation.

On day 186 the wind stress dropped and no major spike was spike produced. Four more spikes were generated from late day 186 to early day 188. These differed from the first group of spikes because the bulk shear vector no longer rotated at the inertial frequency perhaps in response to increasing baroclinic tidal currents as spring tides approached. Spikes are still produced when the wind stress vector and bulk shear vector align but decrease in magnitude on days 187 188 and little bulk shear remains on day 189. This was unfortunate since these two days at the end of the deployment were when dissipation measurements were made from aboard the RV Prince Madog.

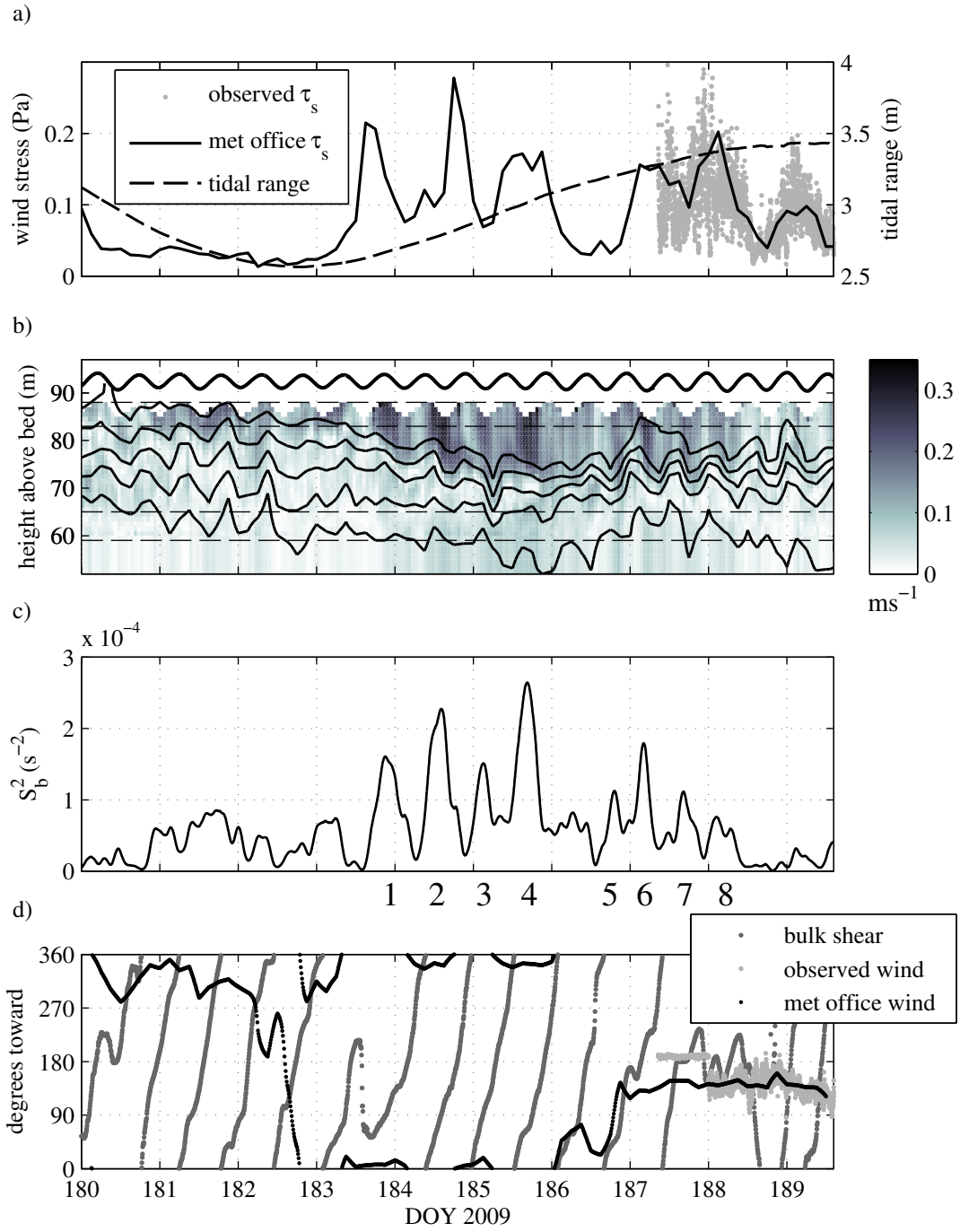

Figure 4.2: Bulk shear analysis from period P2. a) Wind stress calculated from Met Office 3h reanalysis wind (solid line) and observations (grey dots). mean tidal range (dashed line). b) Magnitude of mid-water velocity with temperature contours overlaid (11, 12, 13 and 15°C) . c) Magnitude of bulk shear squared, S_b^2, calculated from 2h moving average mean velocity above (82 to 88mab) and below the thermocline (60 to 65mab) (dashed lines on pane b indicate ranges). d) Direction of bulk shear vector (dark dots) and wind stress (black triangles = met office, light dots = observations). Spikes have been numbered for reference in the text.

4.2.2 Surface layer motion

Current profiles show that shear bulk shear during periods P1 and P2 was primarily due to the wind driven inertial motions of the surface layer. In order to visualise the production of shear due to this surface layer motion a progressive vector plot (PVP) of period P2 has been plotted in figure 4.3. Wind and the bulk shear magnitude are plotted above the PVP which has a color-scale indicating the magnitude of the shear at that position/time. Wind vector arrows are also plotted at the start of each day over the top of the plotted path. The surface layer shows a series of inertial oscillations the four largest of which relate to the four large shear spikes (numbers 1 to 4) on days 183 to 186.

- Day 183 there are light winds toward the NW which drive the surface slowly north before the surface layer briefly reverses due.

- Day 183-184: stronger winds toward the NNE generate a strong easterly surface current producing the first major shear spike. The green color of the path at this time indicates that the shear at this time peaks at $1.5 \times 10^{-4}\mathrm{s}^{-2}$ before the Coriolis force steers the surface layer clockwise so that the wind stress is opposing it. This decelerates the surface layer tightening the radius of the oscillation through its southerly portion.

- Day 184: When the surface layer moves north again the wind is blows strongly towards the north and the shear grows once again. This second oscillation reaches a greater magnitude of $\mathrm{S}_\mathrm{b}^2 = 2 \times 10^{-4}\mathrm{s}^{-2}$ and path is coloured in orange when the motion of the surface is again easterly.

- Early day 185: This smaller spike occurs due to the wind weakening and shifting to the NE which generates a smaller oscillation.

- Late day 185: the final, largest spike, is formed as the wind blows strongly towards the NNW and generates large bulk shear ($\mathrm{S}_\mathrm{b}^2 = 3 \times 10^{-4}\mathrm{s}^{-2}$) as the surface layer moves towards the ENE.

- Day 186: The wind stress drops and there are two smaller oscillations which produce modest spikes.

- Day 187-189: The wind strengthens and blows towards the SE driving the surface layer south. The spikes generated over days 187 and 188 occur when the strongly rectilinear tide and wind stress are both directed south reflecting the interaction between the wind and tide discussed previously.

Figure 4.3 shows that the net transport of the surface layer is at $\sim 90^\circ$ to the right of the wind direction. This is a consequence of the peak surface layer velocity (and therefore bulk shear) occurring when the surface layer velocity was at 90° to the wind.

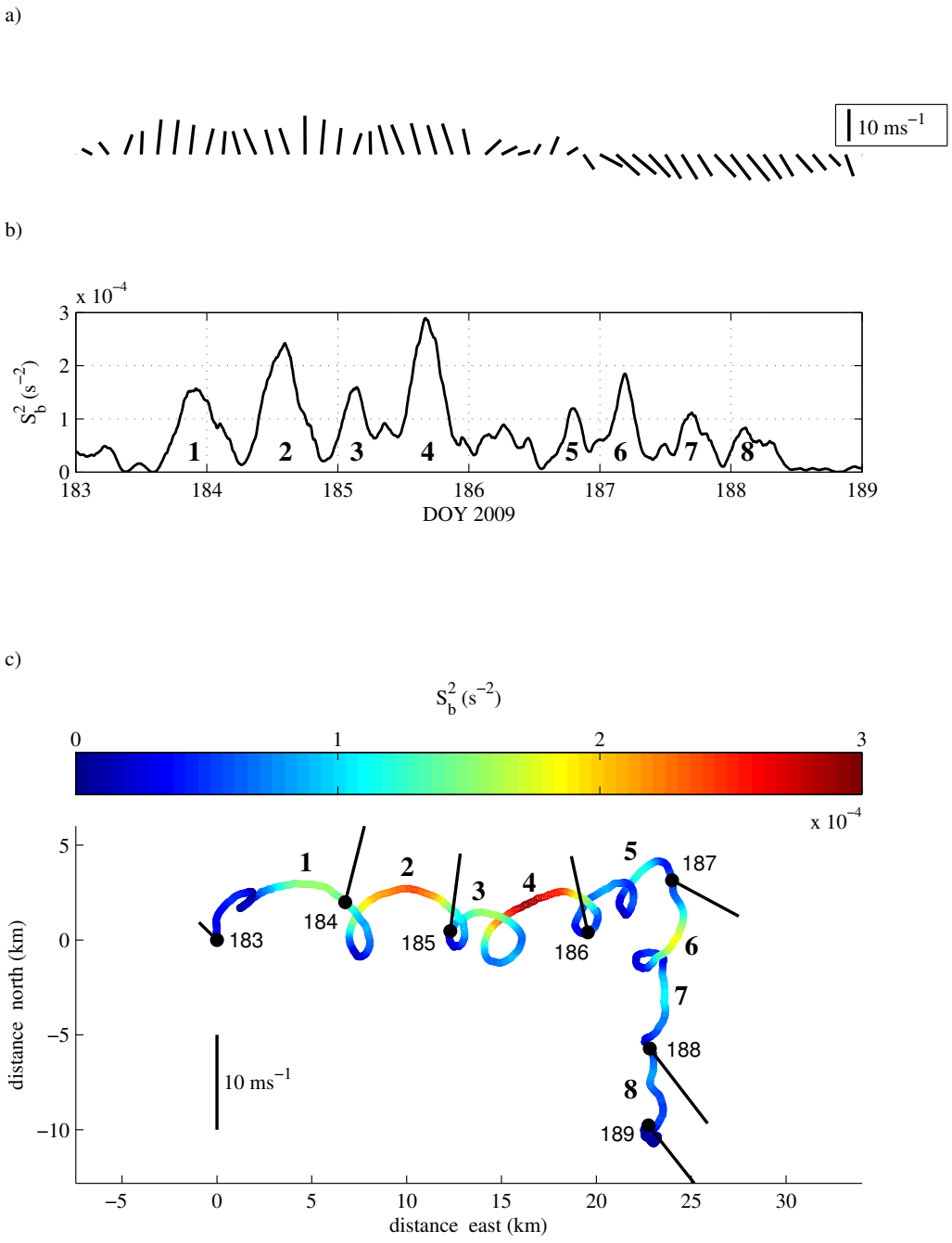

Figure 4.3: Surface layer progressive vector plot showing shear during inertial oscillations on days 183 to 189. a) Time series vector plot of met office reanalysis wind speed. b) Bulk shear squared calculated from the mid-water adcp data. c) progressive vector plot of the surface layer motion with the color of the plot indicating the magnitude of shear. Wind vector is plotted at the start of each day.

4.2.3 Shear production

The production of shear is described in the Burchard and Rippeth [2009] 2 layer model. The first term in equation 1.19 describes the production of shear and predicts that peak production occurs when the bulk shear vector, $\vec{S}$, wind stress vector, $\vec{\tau}_s$, and bed stress vector, $\vec{\tau}_b$, are perfectly aligned:

$$P(S^2) = \frac{4}{h}\vec{S}.\left(\frac{\vec{\tau}_s}{h_s} + \frac{\vec{\tau}_b}{h_b}\right) \tag{4.1}$$

This prediction was tested by calculating the rate of shear production, P, using the met office winds, and adcp current data to generate a time-series for the bulk shear vector and bed stress vector. The surface layer depth, h_s, and bottom layer depth, h_b were estimated to be 15m and 75m respectively. The resulting production of shear is plotted for spikes 1-4 in figure 4.4 along with the observed shear production ($\delta_t S_b^2$).

The two agree well in their general pattern but that the model underestimates the production by a factor of approximately two. However this may be due to the value used for the surface layer depth. There is also a small spike on day 185 which the model misses entirely. The production of shear is dominated by the wind stress term with a negligible contribution from the bed stress term . This is because, despite surface and bottom stresses of similar magnitude, the bottom layer ($h_b = 70m$) is large compared with the shallow surface layer ($h_b = 15m$), which reduces the bed stress shear production. Later in the year when the mixed layer is deeper the bed stress term is likely to become more significant.

The circles plotted in 4.4 mark the peaks in S_b^2 and occur when the production term is ~ 0 and falling. Each of the peaks occurs when the wind was at an angle of 90° to the right of the bulk shear vector and marks the point at which the wind stress opposes the surface current and starts to remove energy from the surface layer. This is the same effect which was observed in the surface layer motion plot (figure 4.3 and can be understood if we examine the way in which the production term is calculated (including only the dominant wind stress term).

$$P(S^2) = \frac{4}{h}\vec{S}.\frac{\vec{\tau}_s}{h_s} \tag{4.2}$$

Since $\vec{S}$ and $\vec{\tau}_s$ are both vectors the product of these two (using the dot product rule) is the cosine of the angle, θ between them.

$$P(S^2) = \frac{4}{h}S.\frac{\tau_s}{h_s}cos\theta \tag{4.3}$$

Therefore production is maximised when $\theta = 0$ since $cos\theta = 1$ and wind and shear vectors are aligned. However the peaks occur after this when $P(S^2) = 0$ so:

$$P(S^2_{BR}) = \frac{4}{h} S . \frac{\tau_s}{h_s} cos\theta = 0 \tag{4.4}$$

This has solutions at $\theta = \pm 90^\circ$. The two solutions relate to a minimum S^2_b at $\theta = -90^\circ$ with peak S^2_b at $\theta = +90^\circ$. This is one quarter of an inertial cycle, so in the Irish sea peak S^2_b occurs approximately 3.75 hours after the shear vector and wind vector align.

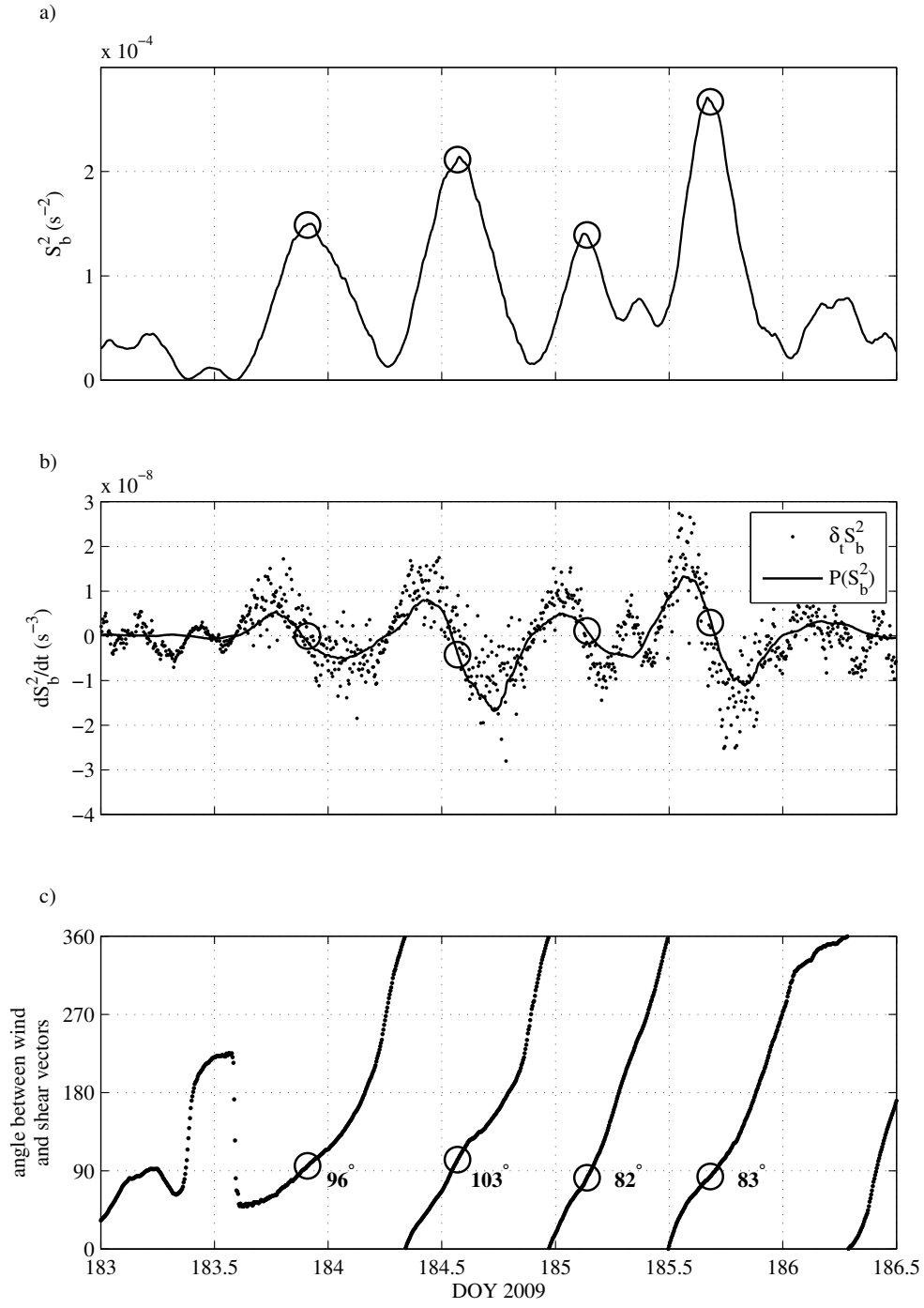

Figure 4.4: Bulk shear production for inertial shear spikes, days 183 to 186.5. a) Magnitude of bulk shear squared, S_b^2. b) time derivative of bulk shear squared, dS_b^2/dt, Production of bulk shear squared $P(S_b^2)$ from equation 4.1, both calculated using adcp data. d) The clockwise angle from the shear vector to the wind vector. The circles indicate the peaks of the shear spikes and occur when: $P(S^2)$ is ~ 0 and $\vec{\tau}_s$ is $\sim 90^\circ$ clockwise from $\vec{S}$.

4.2.4 Richardson number during spikes

Profiles of N^2 and S^2 were computed to a common hourly 2.5m vertical grid based on the height of the thermistors (N^2 calculated using function sw_bfrq.m [Morgan, 1994]). These are plotted for P2 in Figure 4.5 above the inverse Richardson number calculated from them. The stratification is initially very diffuse extending from 60mab right up to the surface with shear concentrated close to the surface. The shear spikes (pane b) correspond to 5-10m thick regions of elevated shear (pane b) which penetrate deeper as they increase in strength. There is an additional spike, which has been labeled spike 0 which is observed close to the surface and not captured by the calculation of S_b^2 due to the limited range of the adcp. The first three spikes (0 to 2) each cause a deepening of the surface mixed layer (pane c) although there is a a small retreat after each spike as shear declines. The first three spikes reduce the Richardson number below 0.3 for several hours and briefly below 0.25. The fourth smaller spike has little effect only reducing Ri below 1 right at the thermocline. The fifth, and largest spike reduces Ri below 0.5 but its effect appears to have been mitigated by the increase in N^2 from 3×10^{-4} to 1.2×10^{-3}. Peaks in N^2 coincided with the peaks in S^2. e.g. day 183.9 and 186.2. The increase in N^2 was more rapid than the increase in the shear as the spikes increased in magnitude. The impact of the shear spikes on the stratification is clear, rather than mixing from the centre of the thermocline and broadening it the shear spikes appear to deepen the mixed layer with each spike eroding the thermocline from above. Figure 4.6 shows an enlargement of Ri^{-1} during the deepening period, with a white line plotted to indicate the height of maximum N^2. The plot above this (pane b) shows a plot of Ri^{-1} at the height of this line in black with lines also plotted for Ri^{-1} from 3.7m above and 3.7m below. The highest values of Ri^{-1} was generated by the first (spike 0), with each subsequent spike producing lower spikes in Ri^{-1}. This illustrates the decreasing effectiveness of the shear spikes over time despite their increasing magnitude.

Another key feature is the relative stability of the upper and lower thermocline. The lower thermocline remains stable with Ri^{-1} generally below 1 throughout most of the spiking period. Ri^{-1} is greater at the height of the maximum stratification, although never falling below $Ri^{-1} \sim 3$. Notably it is the upper thermocline which has the highest values for Ri^{-1} with the three main peaks causing deepening all greater than $Ri^{-1} = 3$. This indicates that the shear spikes erode the top of the thermocline and entrain thermocline water into the surface mixed layer. Since the surface layer remains well mixed it follows that this must be turbulent also. The fact that N^2 is low in the surface layer means that relatively low shear is required to generate instabilities, this may be too small to measure.

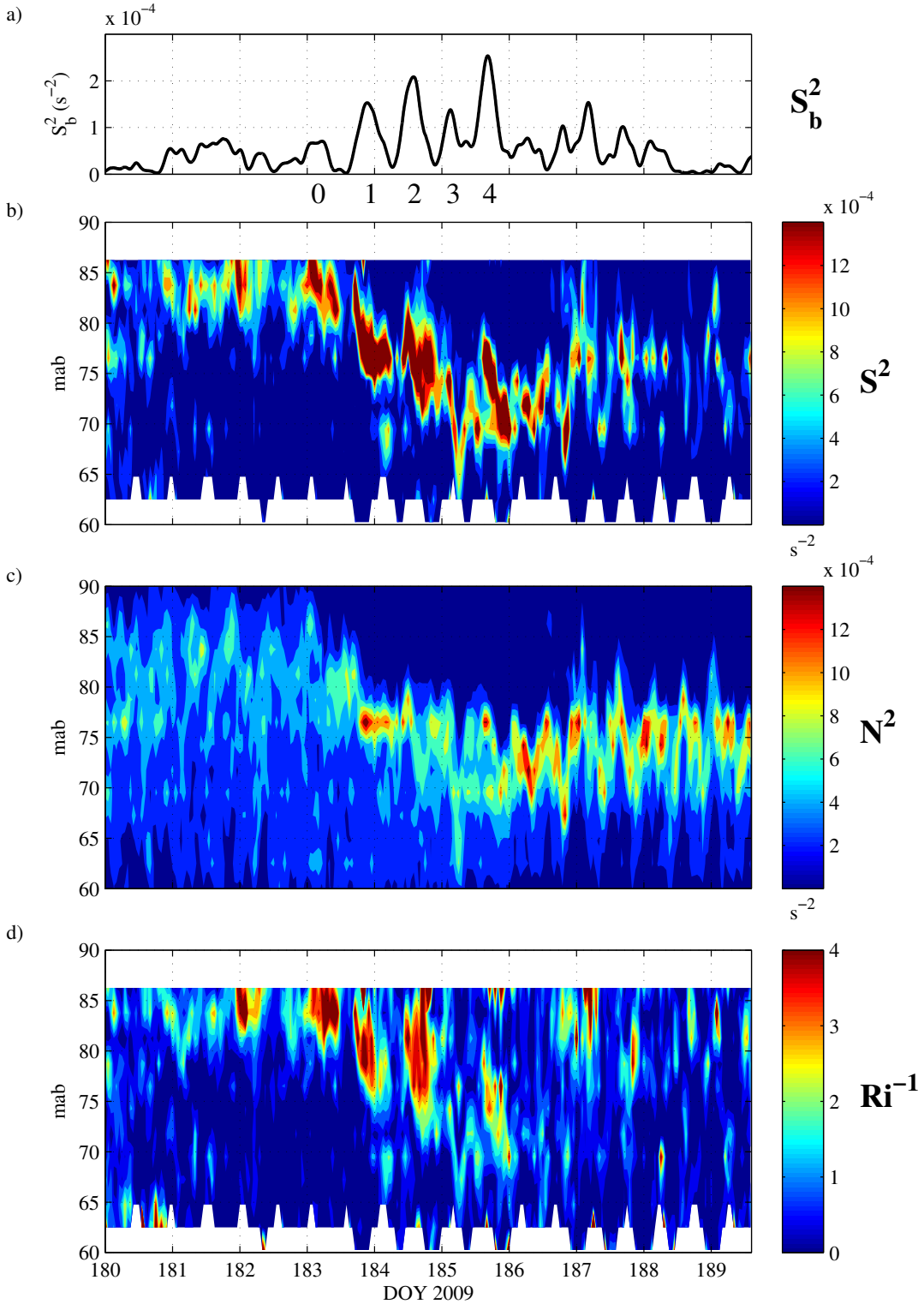

Figure 4.5: Inverse Richardson number, S^2, N^2 and bulk shear spikes, days 180 to 190. a) magnitude of the bulk shear squared. b) time series of the vertical structure of S^2. c) the vertical structure of N^2 d) the vertical structure of Ri^{-1}. The first three shear spikes reduce Ri and cause the thermocline to deepen while N^2 increases.

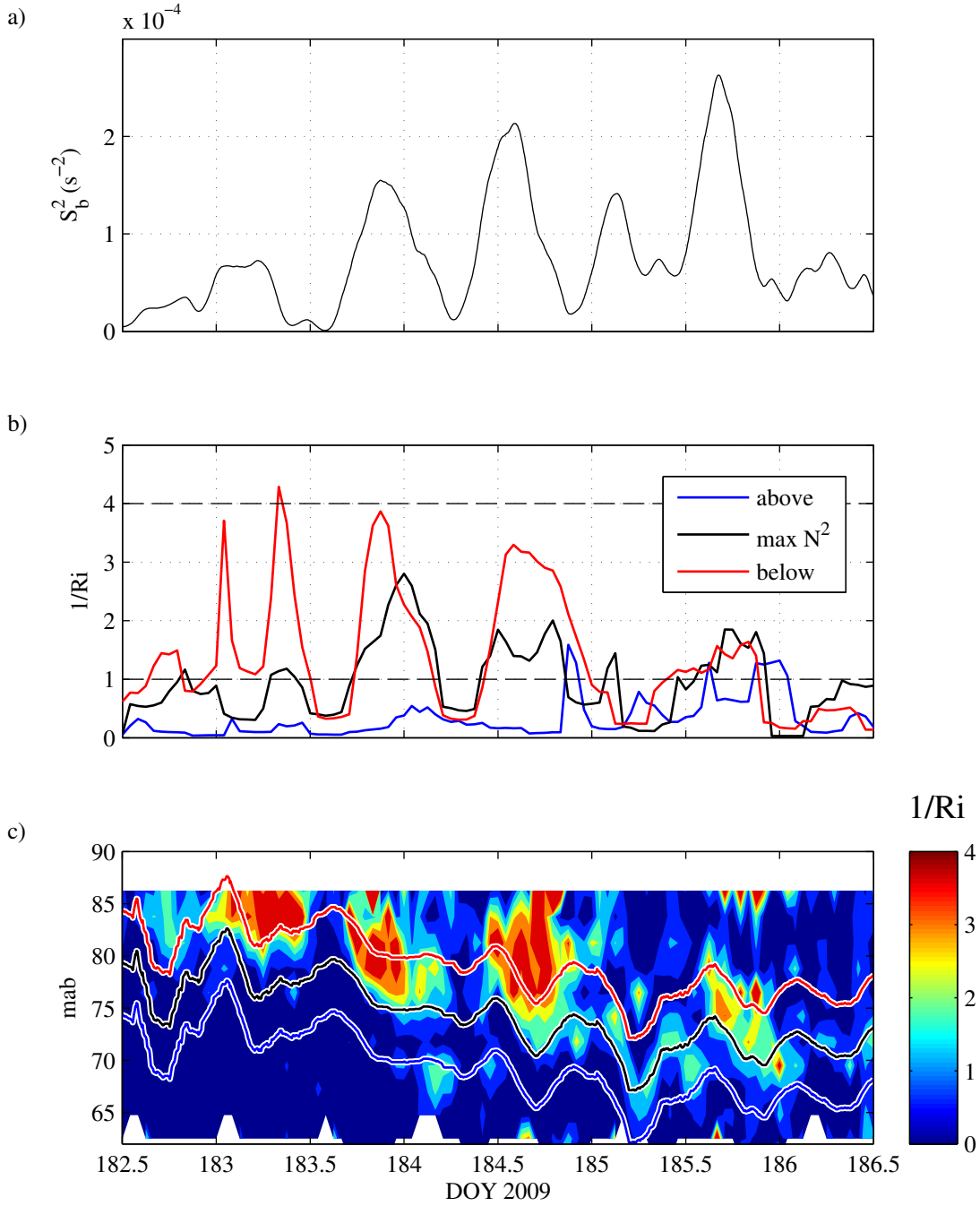

Figure 4.6: Ri^{-1} for shear spikes days 183 to 186.5. a) magnitude of the bulk shear squared.c) time series of the vertical structure of N^2 c) Ri^{-1} at the height of maximum N^2 (black) and 3.75m above (red) and below (blue). d) time series of the vertical structure of Ri^{-1} with lines indicating the height of the maximum N^2 and 3.75m above and below. Ri^{-1} is highest in the upper half of the thermocline with stability increasing lower down.

4.2.5 Dissipation Observations

The strong winds during period P2 delayed the mooring recovery cruise because the RV Prince Madog could not leave port due to the sea state. This was unfortunate since it prevented direct observation of mixing during the initial set of large shear spikes which deepened the mixed layer. However the cruise did overlap with the second set of smaller spikes (see ships met data in figure 4.2). Unfortunately the shear vector was no longer rotating at the inertial period in the standard shear spike generation mode when the ship arrived at the mooring site, however two small spikes (7 and 8) were observed during the dissipation observations.

Figure 4.7 presents the time series of ε averaged to 30 minutes. The commonly observed features of dissipation in stratified shelf seas are present. An energetic bottom boundary layer ($\varepsilon > 10^{-3}\mathrm{Wm}^{-3}$) extended up to a maximum of 50m above the bed and increased through the time series as spring tides approached. The interior of the water column was generally low energy ($\varepsilon < 5 \times 10^{-5}\mathrm{Wm}^{-3}$) although there were occasional patches of elevated dissipation ($\varepsilon > 5 \times 10^{-4}\mathrm{Wm}^{-3}$). The surface layer is not well resolved through the entire time series due to the time taken for the VMP to reach terminal velocity combined with internal tidal motions of the thermocline. However it is clearly intermittently turbulent with energetic periods ($\varepsilon > 5 \times 10^{-4}\mathrm{Wm}^{-3}$) around day 187.9) and relatively quiescent times ($\varepsilon < 5 \times 10^{-5}\mathrm{Wm}^{-3}$ around day 187.9). The thermocline region also displayed a highly variable rate of dissipation, with mean rates varying by four orders of magnitude over the time series.

Dissipation rates in the surface layer, ε_s, and thermocline region, ε_{therm}, are plotted in figure 4.8 together with the observed wind stress, τ_s and bulk shear, S^2. The pattern in the observed wind stress is reflected in the mean dissipation in the surface layer (pane b) with peaks in both occurring on day 187.9 and day 189.1. There is an order of magnitude difference in τ_s between these peaks and the minimum on day 188.6 which is matched by an order of magnitude difference in ε_s over the same periods.

The dissipation in the thermocline, ε_{th} (pane d) has three major peaks, and while two of these occur at time of elevated wind stress the central one does not. There is a minimum in ε_{th} on day 187.9 when τ_s is a peak suggesting that wind stress is not directly driving the dissipation at the thermocline. There is better agreement between the dissipation and the bulk shear with the first peak in ε_{th} matching the first peak in S^2 but responding less to the second spike. The final spike in ε_{th} (day 189.2) also occurred at a time of elevated bulk shear. The large spike in ε_{th} on day 188.4 occurs at a time of low bulk shear and low wind stress. However the cause of this spike is evident in a scatter plot of the individual VMP profiles for the first half of the time series (figure 4.9). The high dissipation on

day 188.4 occurs during two large depressions in the thermocline indicating that short period internal waves were the cause of the intense turbulence at this time. These waves were the largest observed during the VMP profiling period, however a number of smaller displacements were also observed (day 187.7 to 187.8) and these profiles also showed elevated ε_{th} at the thermocline. It is interesting to note that this was the time of the initial bulk shear spike which leads to the question of whether this elevated thermocline mixing would have occurred without internal waves or whether these smaller waves would have generated such energetic mixing without the background of elevated bulk shear.

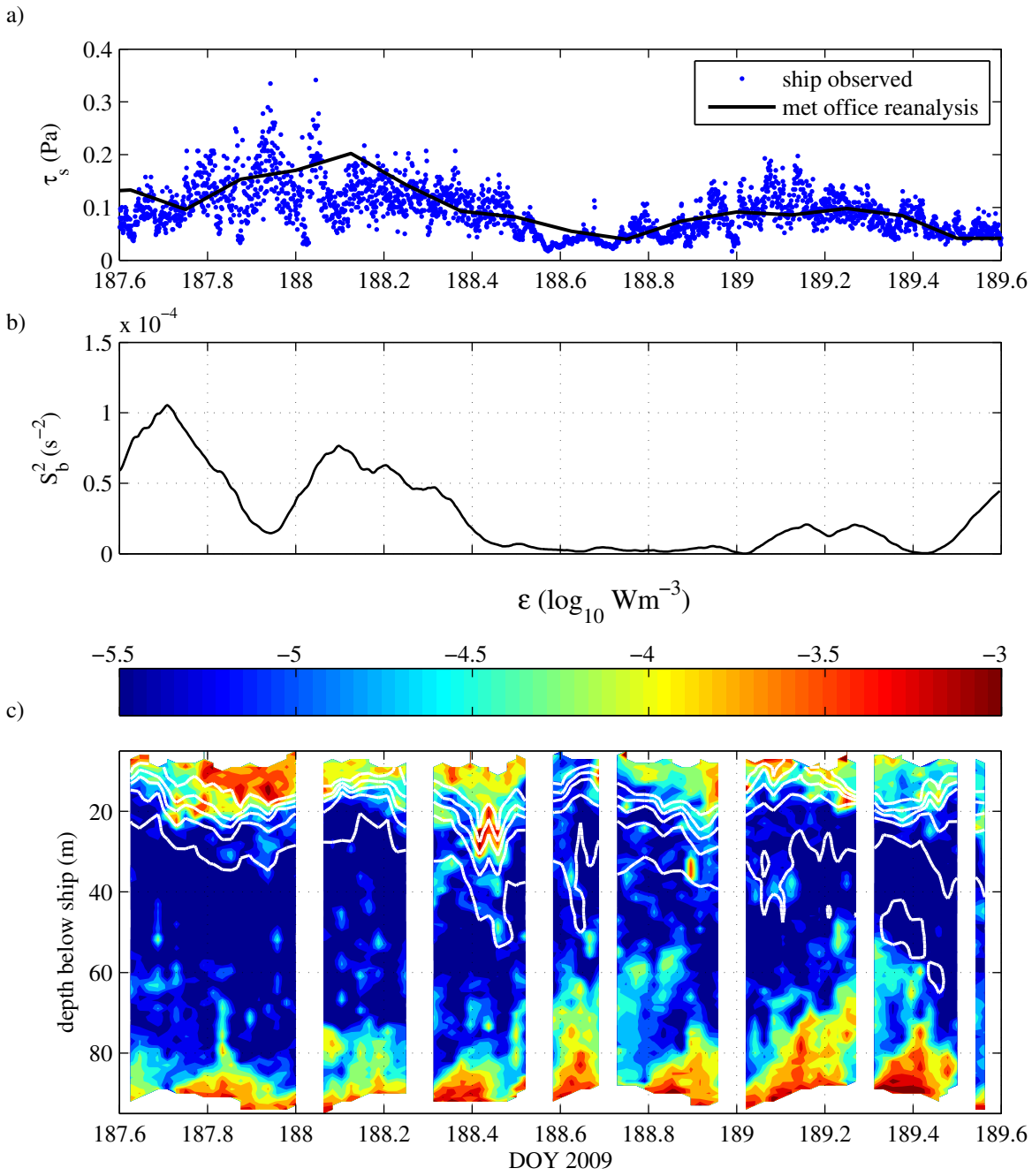

Figure 4.7: 48 hour time series of dissipation from the final two days of the mooring deployment. a) wind stress calculated from the ships observations (blue dots) and the met office reanalysis winds (black line). b) bulk shear squared calculated from mid-water adcp. c) Rate of turbulent dissipation, ε measured using a vertical microstructure profiler deployed from the RV Prince Madog. Data averaged to 30 mins and 1m common vertical grid.

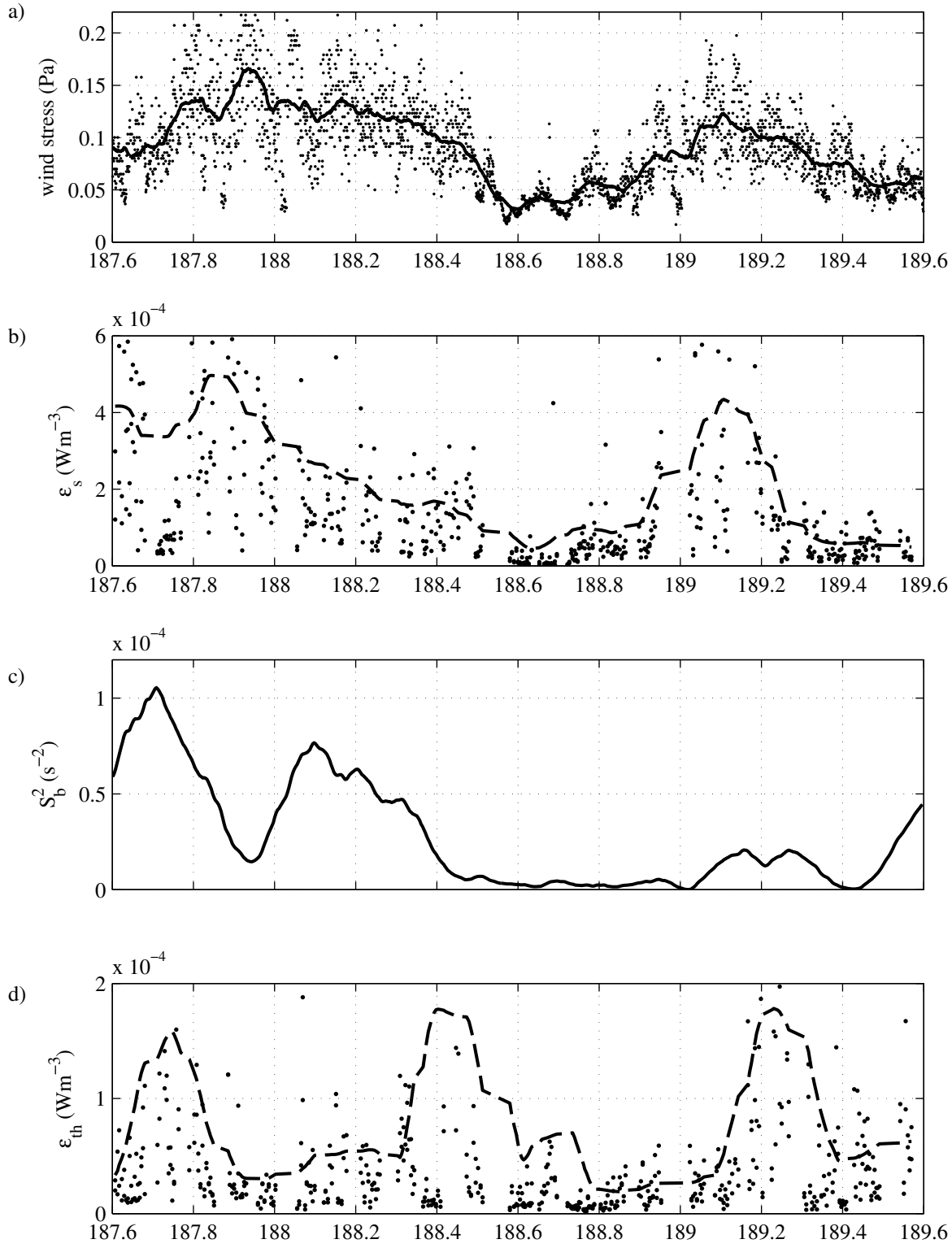

Figure 4.8: Surface layer and thermocline integrated dissipation rates. a) Observed wind stress (dots) and 60 min moving average (line). b) mean surface layer dissipation rate, ε_s and 60min moving average. c) bulk shear squared from mid-water adcp. d) mean thermocline dissipation rate $\varepsilon_t h$ and 60min moving average.

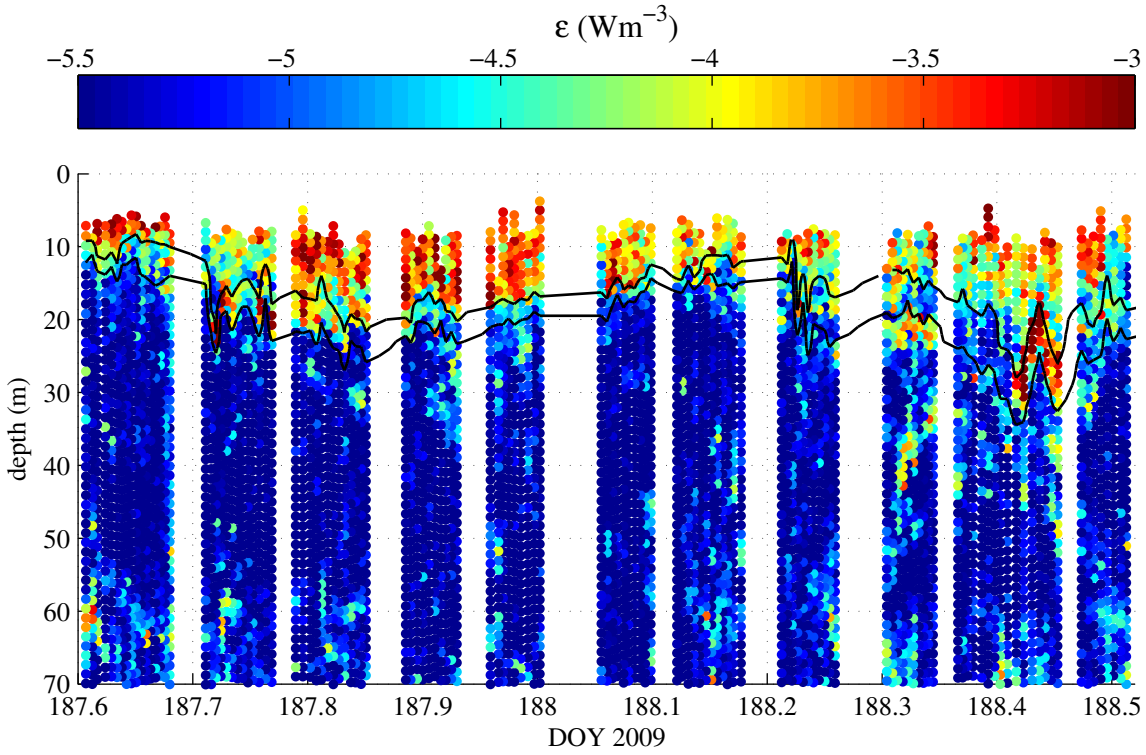

Figure 4.9: Plot of the individual dissipation profiles for the first half of the dissipation time-series. Each individual dot represents one shear spectra and translates to $\sim 1m$ vertical bins. The black lines indicate the position of the $12.5°C$ and $14.5°C$ degree temperature contours. The period of very high ε_{th} occurs during the passage of short period internal waves (day 188.4) while elevated ε_{th} at other times also coincides with rapid displacement of the thermocline.

4.3 Modelling shear spikes

The following section describes attempts, using two different numerical models, to replicate the observed of shear spikes presented in P2. First a simple two layer model is used to replicate the bulk shear dynamics. After this a more sophisticated 1D turbulence closure model is employed to further understand the vertical structure of mixing by the spikes.

4.3.1 Two layer model

The Burchard and Rippeth [2009] model accounts reasonably well for shear production during the shear spiking observations presented for period P2. However that approach used observations of current velocity to calculate the shear vector direction. Their paper describes a two layer numerical model which can be used for the prediction of shear from basic knowledge of wind and tides alone (for details see chapter 2.7).

Running the model using the met office winds and realistic tidal forcing reproduced the observed shear spikes with approximately the correct timing, but the amplitudes proved sensitive to the depth of the mixed layer. Figure 4.10 shows the bulk shear generated by the model using three different values for the mixed layer depth, $h_s = 8$m, 10m and 12m. The effect of increasing the mixed layer depth by 50% is to increase the shear of the largest spike by 150%. This is a problem for getting the correct magnitude of the spikes when using a single value for h_s. The first spikes are too small while the later spikes are too large. The problem is that during the observed shear spiking events there is a significant change in the depth of the mixed layer. Figure 4.11a shows that the base of the mixed layer descends from a depth of 5m to 14m during the first four shear spikes before rebounding slightly to 12m. When the observed mixed layer depth is applied to the model the shear spikes obtained are relative better proportioned and more consistent with the observations.

This dependence on the mixed layer depth to give the correct shear levels could be a problem since it would preclude the use of a mean seasonal value since the depth is sensitive to recent mixing history and meteorology. A more sophisticated model is needed to describe the mixing due to the spikes and estimate the correct mixed layer depth.

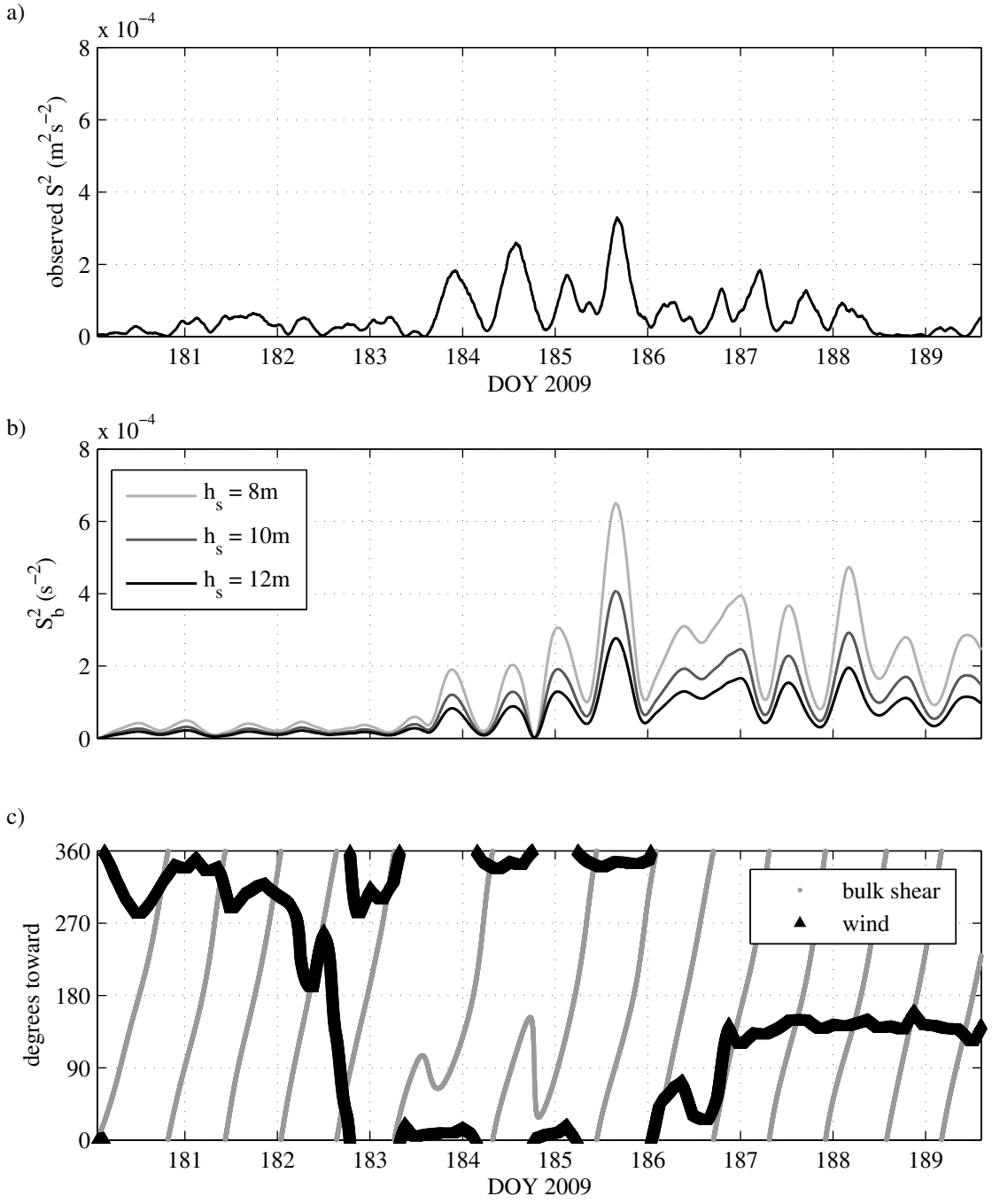

Figure 4.10: Two layer model shear spike sensitivity to mixed layer depth. a) Observed bulk shear from period 180 to 190 compared with b) bulk shear from, two layer model with three different surface layer depths, 8m, 10m and 12m. c) bulk shear and wind direction for the two layer model. The two layer model reproduces the phase of the initial group of shear spikes quite well, however the magnitude of the spikes is highly dependent on the mixed layer depth.

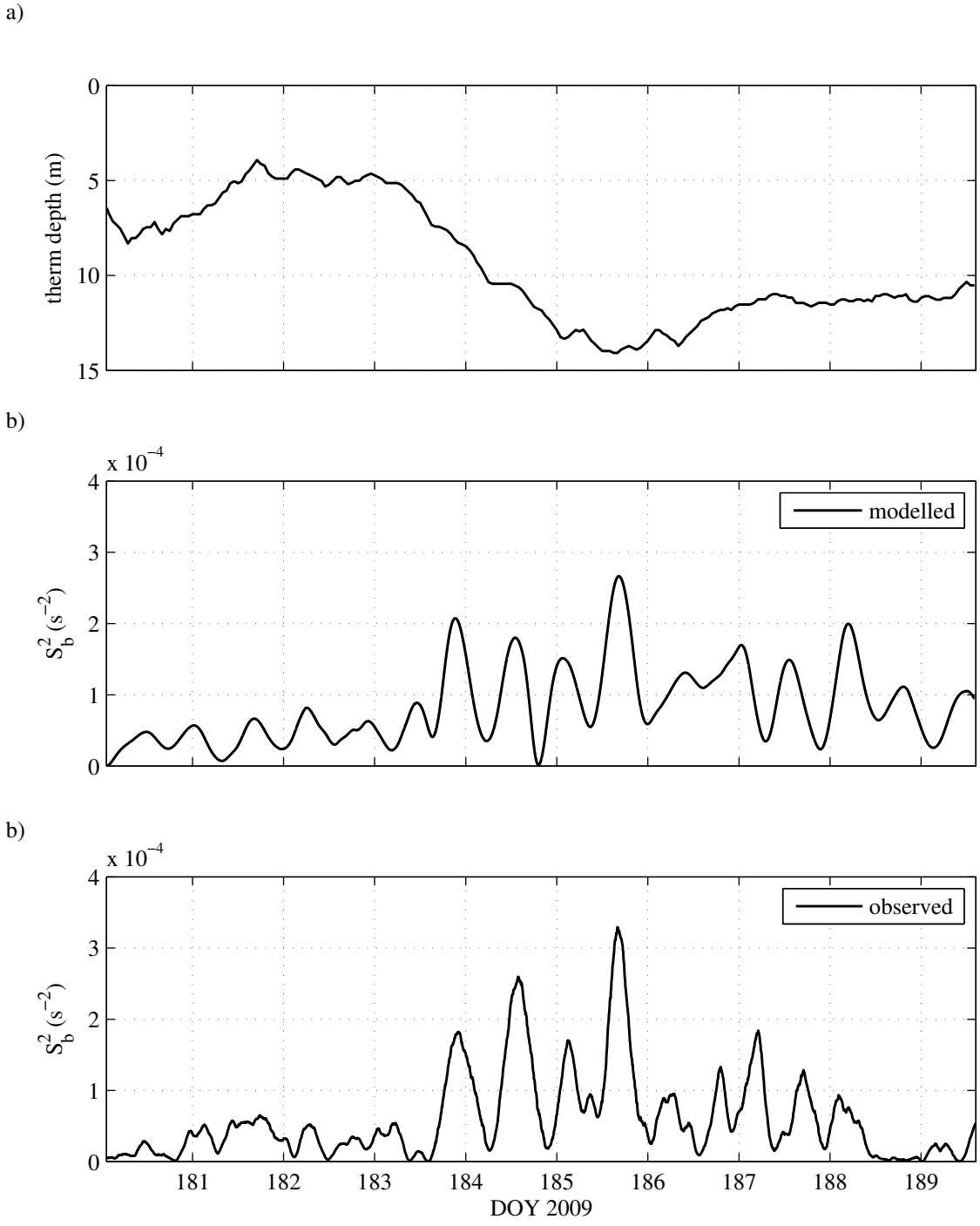

Figure 4.11: Two layer model shear spikes using the observed mixed layer depth. a) depth of the base of the surface mixed layer calculated from the observations. b) bulk shear squared from the two layer model using the depth of the mixed layer h_s from pane a. c) Observed bulk shear

4.3.2 Turbulence closure model

A. Figure 4.12 presents the output of a 1D turbulence closure model (chapter 2.9) for shear spike period, P2. Output is presented in the same bulk shear format as previously and shows that the model reproduces a set of shear spikes very similar to the observations. There are small discrepancies in the phase and amplitude of the spikes but the general pattern of dynamics is reproduced very well. The model develops strong inertial currents in the surface layer which cause the bulk shear vector to rotate at the inertial frequency with almost exactly the same phase as the observations. The density structure also evolves in approximately the same way with rapid deepening of the mixed layer accompanying the initial spikes. The model however does fail in two respects. Firstly the modeled surface layer cools by a couple of degrees compared with the observations which is due to the model running without heat input. This reduces stratification making it easier for the spikes to mix and deepen the pycnocline also diminishing spike magnitudes. The second difference occurs after day 186 where tidal influence became significant and the model failed to capture these effects.

Since the model reproduces the observed dynamics and density structure well it may be useful in understanding the mixing of the spikes since these were not measured directly in the field campaign. Figure 4.13 shows the depth profile time series of S^2, N^2, Ri^{-1} and ε outputted by the model for the upper part of the water column. As in the observations the shear is concentrated at the base of the mixed layer which deepens rapidly with peak shear corresponding to peak N^2. However this layer is much thinner in the model than in the observations. The deepening is accompanied by an entrainment of fluid into the surface layer which is just visible in the plot of N^2 causing a weaker upper layer of shear to form in the surface layer. This weak upper gradient weakens as the deepening and entrainment slow. The shear spikes are clearly visible in the plot of Ri^{-1} with each spike penetrating deeper than the last before subsiding. Unlike the observations this instability is present right to the surface. This may be due to the weak stratification in this region which means that shear is likely to be low even though it is turbulent,it may be too low to measure with the ADCP. The Richardson number remains close to unity in the pycnocline itself throughout the modeled period. The spikes are also reflected in the modeled ε where the spikes penetrate the top of the pycnocline, to a depth greater than the unstable region. The spikes are of greatest magnitude close to the surface and rapidly reducing in magnitude as they encounter this stratification.

The good correspondence between the observations and modeled mixing is highlighted in figure 4.14 which shows that the three main spikes in ε_{mod} (plotted contours) correspond very closely to the observed instabilities Ri^{-1} (colour plot).

The full depth ε time series for the July cruise is compared in figure 4.15. The general form and

magnitude of the bottom boundary layer is reproduced and the surface layer dissipation rates are also realistic, however the modeled mid-water mixing is not well represented. This is illustrated in a mean for the period plotted in figure 4.14. The mean profile of N^2 is slightly broader in the observations but of very similar magnitude. The mean modeled S^2 broadly agree at the thermocline, but falls off in the surface layer in the observations and falls off in the bottom layer in the model. The model represents the observed dissipation rate fairly well in the bottom boundary layer (bottom 40m) and at a depth of 10m below the surface the two also agree. However ε in the stratified mid-water and thermocline region is completely underestimated by up to two orders of magnitude. This failure of the model is highlighted in the mean profiles of dissipation from the observations and from the model which are plotted shown in figure 4.16.

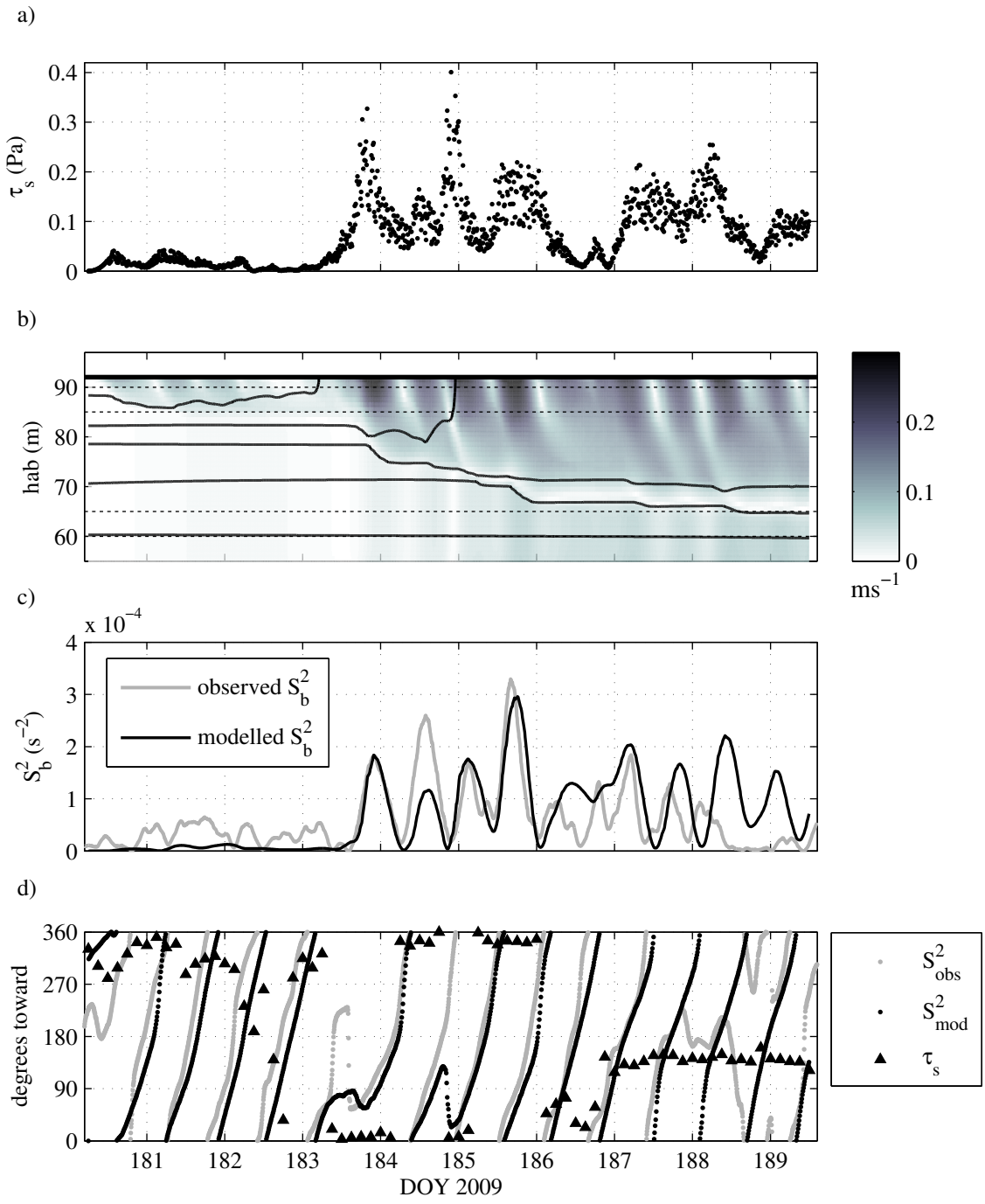

Figure 4.12: Bulk shear analysis of turbulence closure model output for period P2. a) Wind stress calculated from Met Office 3h reanalysis wind with added variability. b) Total baroclinic velocity magnitude with density contours overlaid. c) Magnitude of bulk shear squared, S_b^2, from model (thin black line) and observations (thick grey line). d) Direction of bulk shear vector from model (dark dots) and for observations (light dots). Wind stress direction is plotted as black triangles.

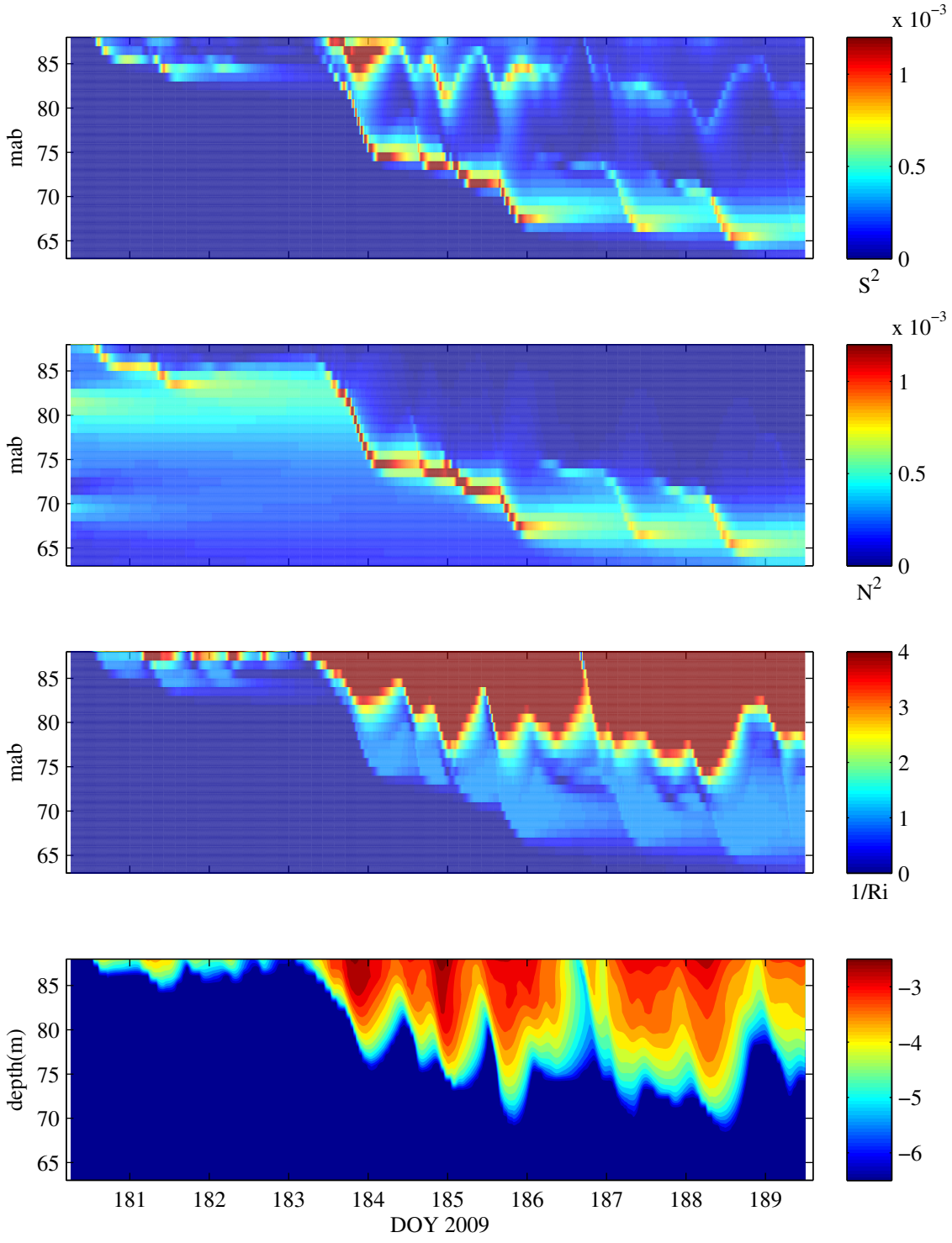

Figure 4.13: Output from turbulence closure model for period P2 as a function of depth. a) vertical profile of shear squared. b) buoyancy frequency squared. c) inverse Richardson number d) turbulent kinetic energy dissipation rate.

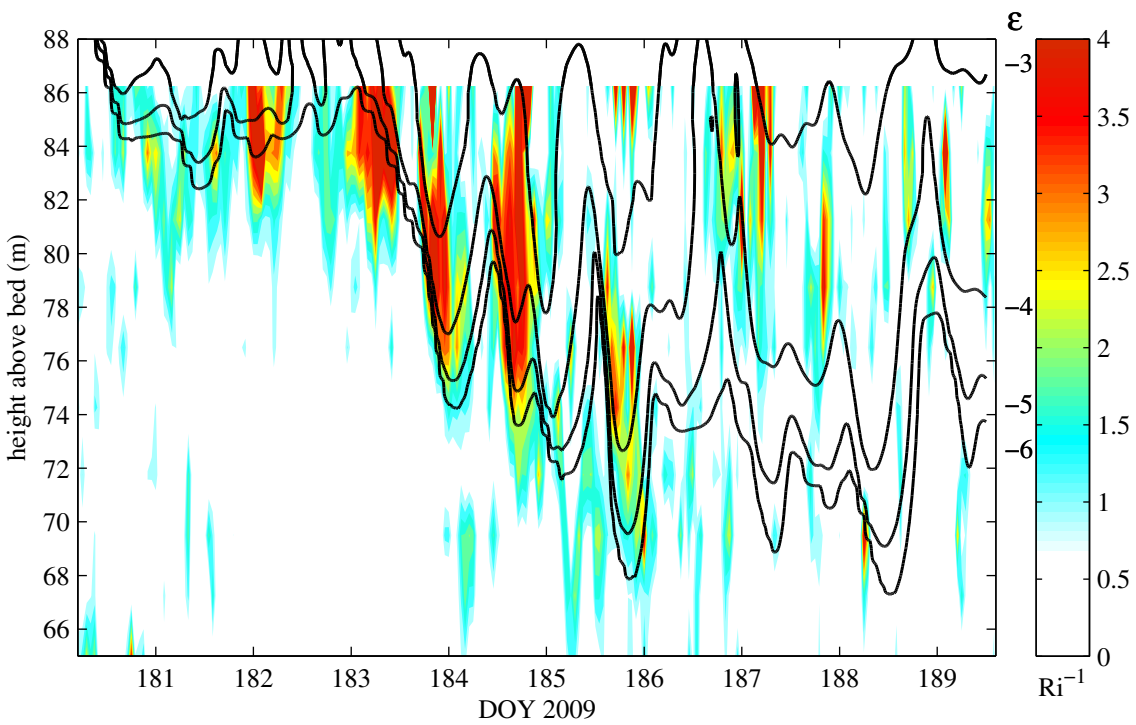

Figure 4.14: Observed inverse Richardson number plotted with modeled turbulent dissipation rate contours overlaid. Contours represents log_{10} rates in Wm^{-3} indicated to the left of the color bar.

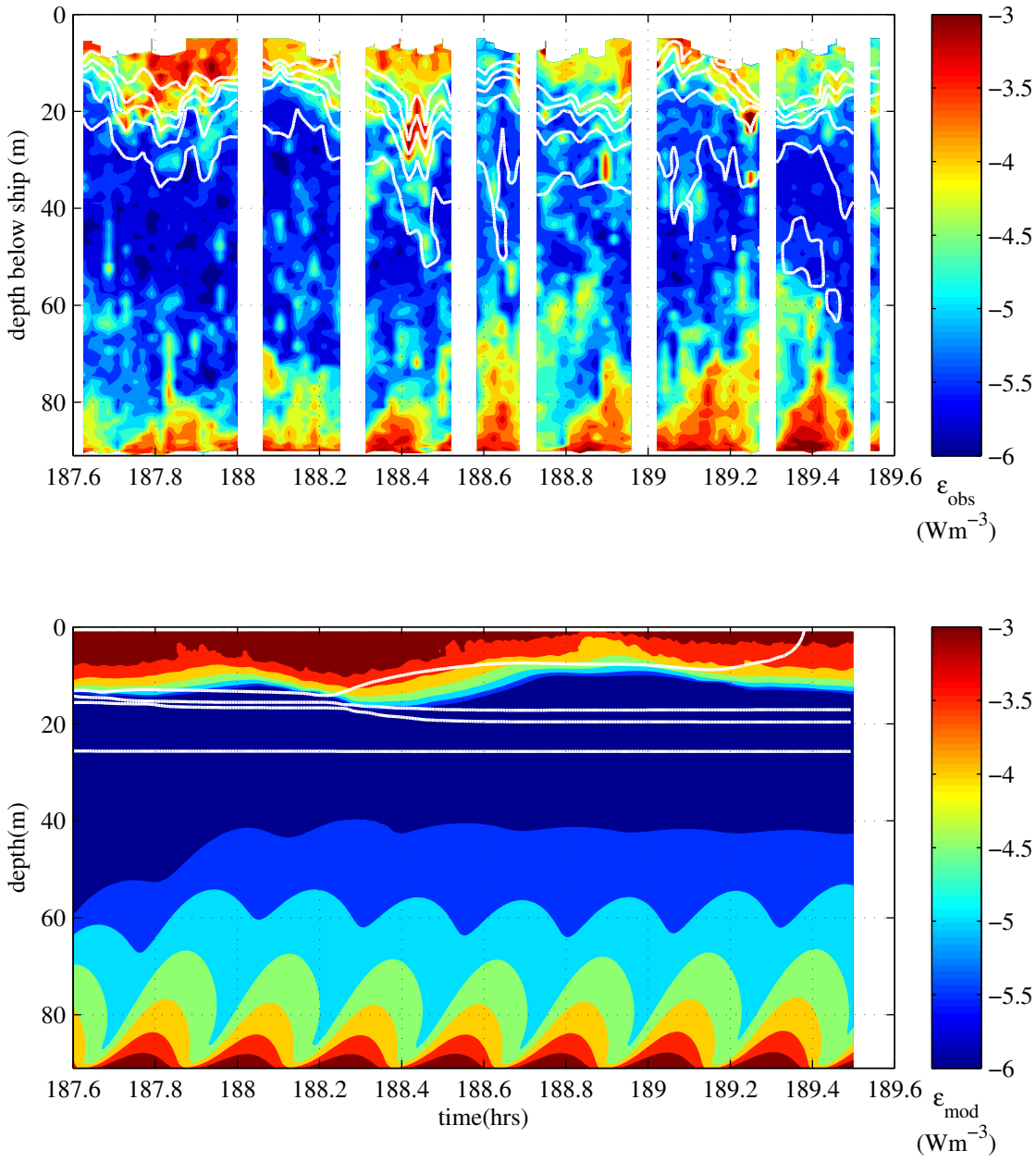

Figure 4.15: Comparison of the modeled and observed turbulent dissipation rate. a) observed TKE dissipation rate b) modeled dissipation rate

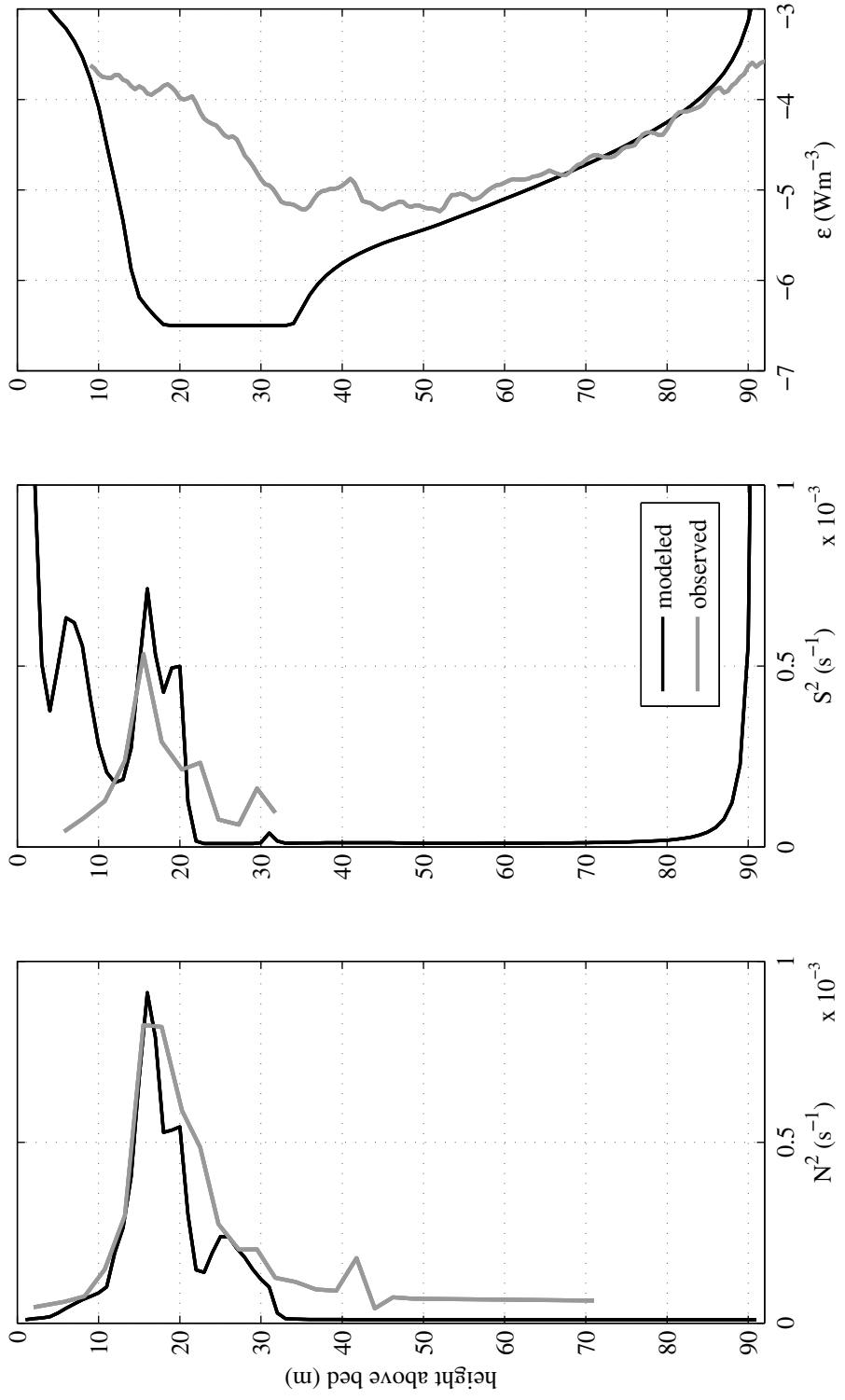

Figure 4.16: Vertical profiles of N^2, S^2 and ε from observations (grey line) and turbulence closure model (black line). a) buoyancy frequency. b) shear squared and c) turbulent dissipation rate.

4.4 Summary

- Shear spikes were observed for 10 days out of 50 when the wind stress exceeded 0.1Pa and were the most energetic features in the dataset.
- Spikes were generated when the wind vector and shear vector aligned so generally occurred at an inertial frequency.
- The two largest shear spikes did not occur at the times of highest wind stress, but when changes in wind direction or magnitude allowed residual shear to accumulate.
- The primary cause of shear across the thermocline was the motion of the surface layer with peak velocities occurring when this motion was at 90° to the right of the wind. This means that spikes occur 3.75 hours after alignment.
- It was not possible to make direct measurements of the mixing during the major shear spike episodes due to the high sea state.
- Microstructure measurements show that surface layer dissipation rate tracked the wind stress, while thermocline dissipation was more closely related to the bulk shear.
- Episodes of elevated mid-water TKE dissipation rate were observed when there was no low frequency bulk shear on such occasions mixing appeared to be due to the presence of internal waves, with elevated dissipation rates observed at displacements of the thermocline.
- Richardson number calculations show shear spikes mixing from the top of the thermocline with spikes generating low Ri regions at the base of the mixed layer.
- Initial spikes not the largest spikes were most effective at mixing since they occurred when stratification was diffuse, close to the surface and N^2 was low.
- The effect of the mixing by each spike was evident in the stratification with a rapid deepening of the mixed layer accompanying the initial spikes.
- There was no net loss of Φ during the spiking period, due to heat input in the surface layer which maintained its temperature despite entrainment of cooler water.
- A simple two layer model worked well to replicate the shear spikes but is limited by sensitivity to the observed changes in mixed layer depth.

- A 1D model using a turbulence closure scheme to estimate mixing was equally capable of replicating the shear spike dynamics and the rapid mixed layer deepening with depth and timing corresponding to the observations.
- The model suggested that the spikes are a form of boundary mixing and generate highest dissipation close to the surface. Despite the models success in reproducing the shear spikes it still underestimates the rate of mid-water dissipation by two orders of magnitude. The reason for the enhanced mixing in the mid-water appeared to be the result of short period internal waves.
- The lack of local wind field and high resolution data did not appear to preclude reasonable replication of shear spikes, suggesting that 3 hour winds are appropriate to dive models once interpolated to a higher resolution.

Chapter 5

Internal waves

During spring tides (days 173 to 181) significant baroclinic semidiurnal tidal currents were identified from least squares fits (chapter 3). Baroclinic inertial currents were more energetic but these were shown to act as a source of boundary mixing and could not be responsible for the anomalous thermocline mixing observed (chapter 4). The evolution of the tidal currents from 2 to 3 layer during the spring tides suggests that internal waves may be acting to mix the mid-water and diffuse the thermocline. Also the direct observations of turbulent dissipation presented in chapter 4.3 suggest that high frequency waves may play an important role in mixing at the thermocline.

This chapter aims to reveal the nature and intensity of the internal tide during the spring tide period when tidal currents dominated. The energy in the waves is estimated to see whether it is sufficient to explain the observed dissipation rates. The high frequency non-linear waves will also be examined to try and understand where they originate and what their contribution may be to internal mixing.

5.1 Internal Tide

In order to illustrate the form of the internal tide and its evolution over time we consider the least squares harmonic fit of the mid-water baroclinic currents which was presented in chapter 3.2.2. The period when tidal frequency baroclinic currents were the dominant process in shear production (segments L and M, days 173 to 180) are examined in greater detail in the following two sections.

5.1.1 Section L - day 173 to 177

During period L stratification extended 20m from 65 mab to 85 mab with peak N^2 at 80mab. Figure 5.1 presents the observations and fits for the baroclinic velocities and isotherm heights. The vertical profile of the fitted velocity amplitudes is plotted (panes e and f) along with the first three normal modes,V1 - V3 calculated from the N^2 profile in pane g (for method see section 2.5). The amplitude of the modes was scaled by eye and it can be seen that the fitted observed profile closely follows the first normal mode over much of the observed range, although it does deviate slightly above 80mab suggesting some higher modal structure. The least squares fits to the isotherms (panes c and d) give amplitudes (pane g) which are relatively constant over the fitted range while the motion of the isotherms were in phase which is consistent with a first mode structure.

5.1.2 Section M - day 177 to 180

During period M stratification had broadened (60 - 90mab), and strengthened (peak N^2 increased by 20%). Figure 5.2 presents the observations and fits for period M which indicate a change in the vertical structure. Peak observed and fitted velocities were found in the centre of the thermocline at 72m while the velocity amplitudes had a distinct 3 layer structure. The lower node of this structure corresponded to the node of the first mode , but above 70mab the structure was more similar to mode 2. Mode 2 dynamics were also apparent in the isotherm motions (pane a) which compress then spread in the form of the second mode (day 179). The amplitudes of the isotherm fits (pane g) also indicate mode 2 dynamics with with greatest amplitudes around the height of the upper node and decreasing toward the height of the velocity maximum.

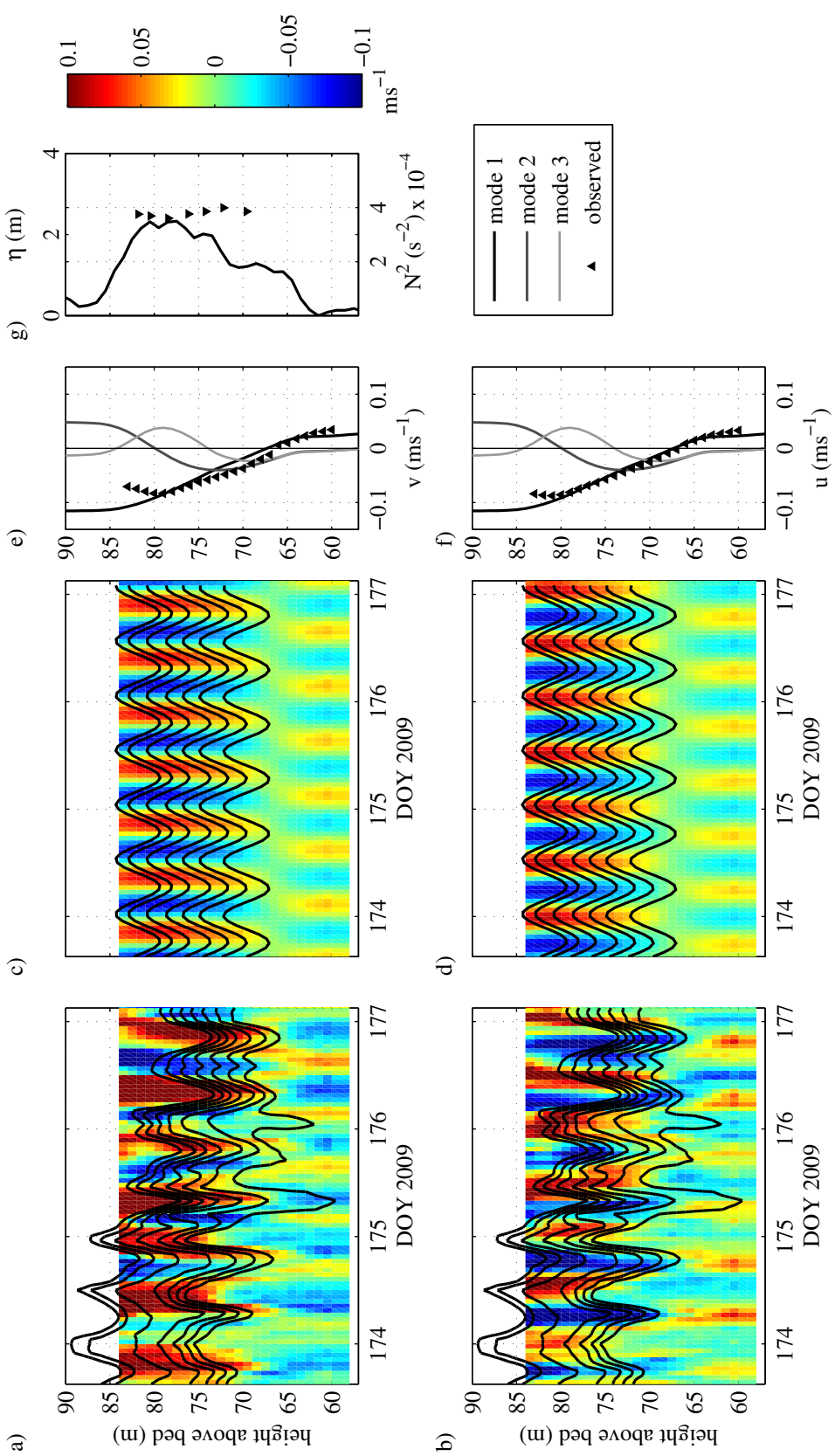

Figure 5.1: Least squares fits of baroclinic currents and isotherm displacements for section L (days 173.5 - 177). a & b) Observed hourly northerly and easterly baroclinic currents with isotherms (11 to 12.8°C in steps of 0.3). c & d) Tidal frequency (M_2/S_2 average) component of least squares fit to the observed velocities and isotherms. e & f) Amplitude of the velocity fits from panes c and d (triangles) with the first three normal modes (solid lines). g) Plot of the N^2 profile (solid line) used to calculate the normal modes and amplitudes of the isotherm displacement fits (triangles).

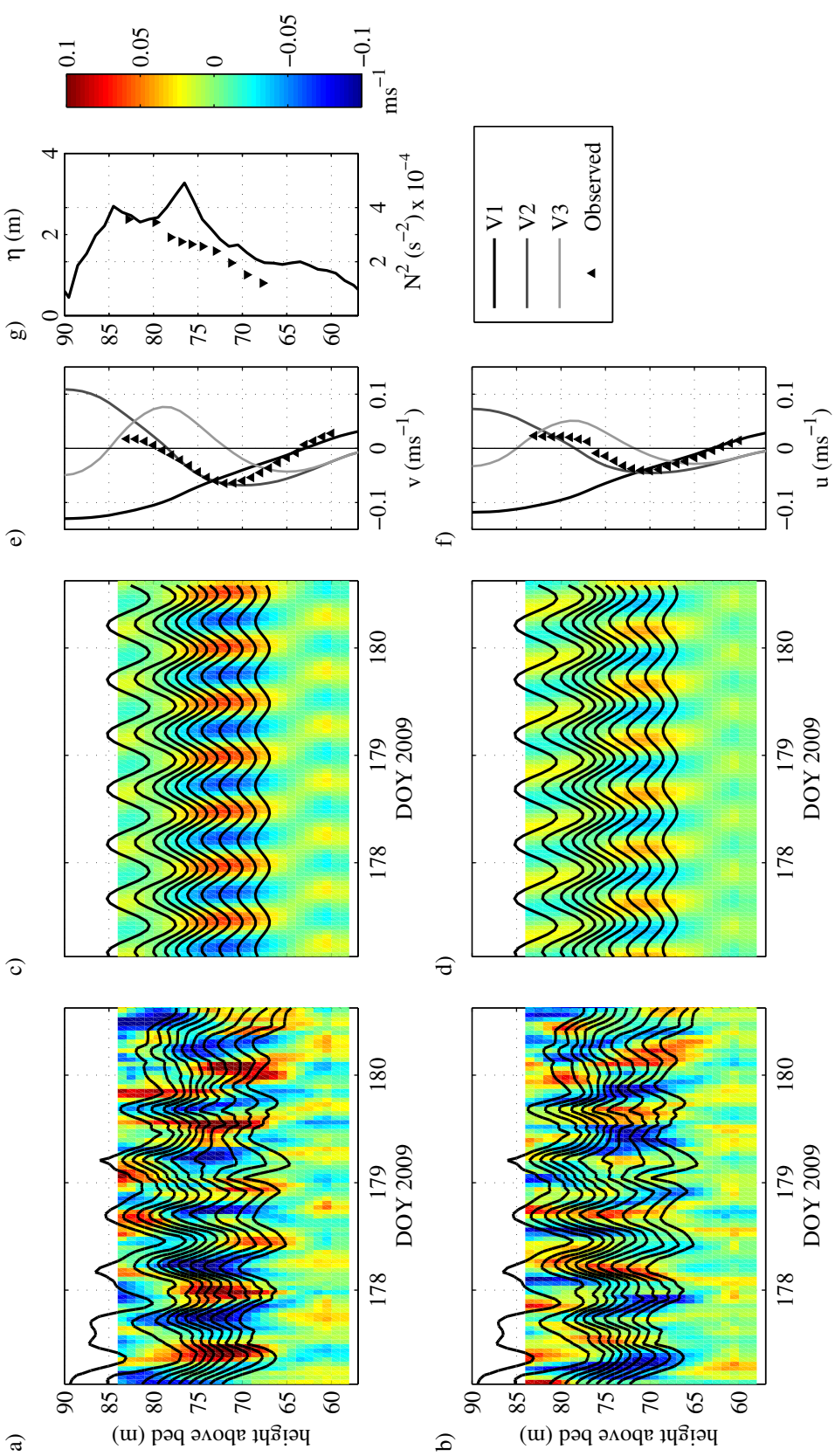

Figure 5.2: Least squares fits of baroclinic currents and isotherm displacements for section M (days 177 - 181). a & b) Observed hourly northerly and easterly baroclinic currents with isotherms (11 to 12.8°C in steps of 0.3). c & d) Tidal frequency (M_2/S_2 average) component of least squares fit to the observed velocities and isotherms. e & f) Amplitude of the velocity fits from panes c and d (triangles) with the first three normal modes (solid lines). g) Plot of the N^2 profile (solid line) used to calculate the normal modes and amplitudes of the isotherm displacement fits (triangles).

5.1.3 Internal tide energy flux and shear

The internal wave energy flux, E_f, may be calculated at depth z and time t from the perturbation in pressure, p', and horizontal velocity perturbation, u' where $\mathrm{E_f(z,t)} =< \mathrm{u'p'} >$ as described by Kunze et al. [2002]. However, the method requires full water column coverage of velocity and density which were not available. An alternative method for estimating the energy flux of linear internal waves is outlined by Baines [1995](Chapter 4.9, p201). Where wave amplitudes are small the total wave energy density per unit volume E_{vol} for a wave travelling in the x direction is given by:

$$E_{vol} = \frac{1}{2}\rho_0(u_{IW}^2 + w_{IW}^2 + N^2\eta^2) \tag{5.1}$$

Where u_{IW} and w_{IW}, are the horizontal and vertical components of the velocity perturbations and η is the vertical displacement of a streamline/isotherm. The results of the least squares fits may then be used to provide values for equation 5.1 and then integrated over depth to generate estimate the flux of internal wave per unit width, E_f, can then be estimated as follows:

$$E_f = c_g . \int_{-z}^{0} E_{vol} \tag{5.2}$$

Where -z is the depth to which data exists and c_g is the group speed of the waves which may be estimated, as described by Chang et al. [2006], from the phase speed, c_p which was obtained by normal mode analysis.:

$$\frac{c}{c_g} = \frac{\omega^2}{(\omega^2 - f^2)} \tag{5.3}$$

Where ω is the frequency of the tide, and f the inertial frequency

Fitted velocities from section L (figure 5.1) were used to calculate the total velocity perturbation, $\mathrm{u_{IW}^2 = u_{fit}^2 + v_{fit}^2}$. This largest tidal velocities and isotherm amplitudes were observed during period L so energy fluxes have been calculated for this period to give an estimate of the maximum energy available for mixing by the internal tide. The group speed of the 1st mode, $\mathrm{c_g = 0.34 ms^{-1}}$ an energy flux of $15\mathrm{Wm^{-1}}$ which seems rather small. However this calculation underestimates the energy density of the internal tide because the velocity data recorded by the ADCP does not extend down to the bed. The contribution due to stratification is accounted for since the stratified part of the water column is well resolved, however the maximum velocities in the first mode internal tide occur in the surface and bottom layer which are out of the range of the ADCP. In order to account for this effect, the fitted dominant first vertical mode (plotted in fig 5.1e) was combined with the least squares fits to generate a full water column time series of velocities. The effect on the fluxes was to double the mean energy to $34\mathrm{Wm^{-1}}$.

Green et al. [2008] showed that the likely generation zone for the internal tide in the Western Irish Sea is in the north of the region and suggested a decay length scale for the internal tide of 100km because this is the length of the stratified region. Since that the region is bounded internal waves are unable to propagate escape then all then it can be assumed that all the internal tidal energy is lost over the 100km length (figure5.3). This gives a mean rate of energy loss for the energetic period L of $\varepsilon_{\text{th}} \sim 0.34\text{mWm}^2$. This rough figure implies that the internal tide contributes at most one third of the total mean thermocline dissipation rate of $\varepsilon_{\text{th}} \sim 1\text{mWm}^2$. This leaves a deficit of $\varepsilon_{\text{th}} \sim 0.66\text{mWm}^2$ in the thermocline mixing budget.

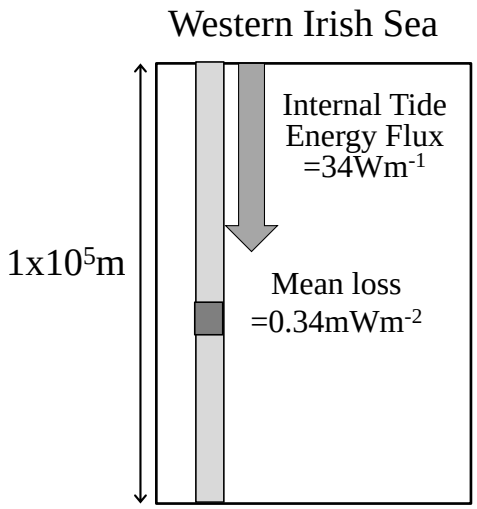

Figure 5.3: Assuming that the internal tide propagates from North to South [Green et al., 2008] and all energy is lost in the stratified region the maximum mean rate of energy which the internal tide can contribute to the TKE mixing budget is 0.34Wm^{-2}.

Another feature of the internal tide highlighted by the least squares fit of the velocities is the magnitude of shear it generates. Peak S^2 calculated from the fitted velocity profiles is $\mathrm{S}^2 = 4 \times 10^{-5} s^{-}2$, whereas the corresponding peak in N^2 is three times this, therefore the gradient Richardson number is over 3. This suggests that the internal tide at the mooring location falls far short of generating sufficient shear to drive instabilities and another process must be responsible for the instabilities which generate turbulence in this location.

5.2 Non-linear internal waves)

High frequency vertical motions of the isotherms were observed throughout the mooring deployment. During spring tides the amplitudes of the motions were largest (up to 12m) and non-linear internal waves (NLIWs) were observed in packets of 2-6 waves arriving once every semi-diurnal tidal cycle. Figure 5.4 shows the height of the 11.2°C isotherm plotted over the high resolution easterly currents (sampled at 30s interval with 0.5m vertical resolution) for a period of two days at spring tides (spanning sections L and M). Four packets of waves generated strong oscillating currents in the surface layer, which at times opposed the barotropic tide. Also plotted is the high frequency bulk shear calculated between the top to the bottom ADCP bin. During the largest waves the surface layer currents extend below the bottom bin so shear at these times is underestimated. However despite this limitation, the magnitude of shear measured during the passage of the waves is elevated by up to two orders of magnitude above the background level.

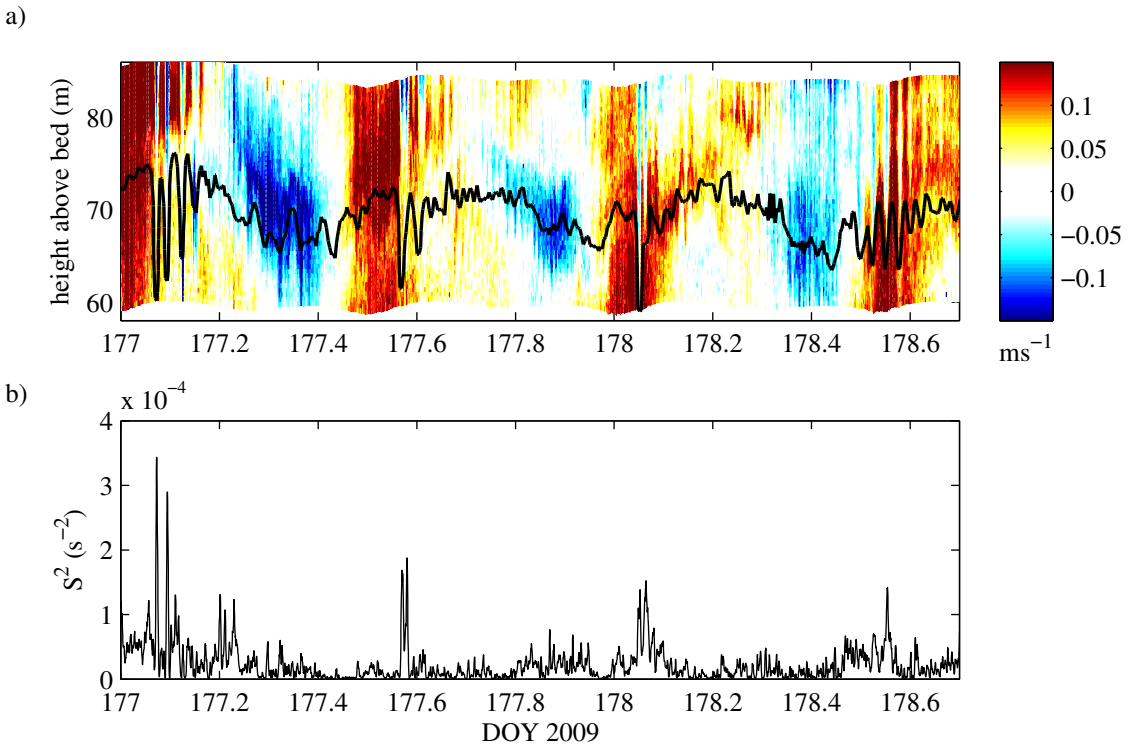

Figure 5.4: High frequency observations of four NLIW packets observed over a two day period during spring tides (sections L and M). a) Easterly component of the horizontal currents with 11.2°C isotherm overlaid. b) High resolution bulk shear calculated as the scaled difference between the top and bottom bins. The presence of the NLIWs is accompanied by elevated shears of up to an order of magnitude greater than the background levels.

5.2.1 Vertical structure of NLIWs

Figure 5.5 presents the vertical structure of the shear, stratification and dissipation for a NLIW packet observed during the VMP profiling on the July cruise. Three waves were observed on the morning of day 188 and high levels of mid-water dissipation were observed (discussed previously in chapter 4.3). Temperature contours measured by the mooring are plotted in pane a, while temperature contours from the VMP are plotted in pane b. The moored temperature data had to be shifted by 3 minutes to align with the velocity structure, due to the separation of the ADCP and temperature string. The VMP data had to be compressed in time by a factor of 3 and shifted by 20 minutes in order to correspond to the moored data. This was necessary due to changes in the position of the ship induced by the surface currents generated by the wave (discussed in further detail later in chapter 5.2.3).
The progression of shear, stratification and dissipation during the passage of the wave packets was as follows:

0 - 10 minutes - Shear was initially diffuse with approximately the same peak S^2 and N^2 magnitude.

10 - 15 minutes - Maximum S^2 descended with isotherms and increases to three times the peak magnitude of N^2.

15 - 20 minutes - In the wave trough ε was elevated by two orders of magnitude above background levels while spike as S^2 fragmented into a number spikes across the thermocline.

20 - 35 minutes - ε remains elevated by up to four orders of magnitude above background level through the second half of the first wave and the trough of the following wave.

40 - 55 minutes - During the third and smallest wave, ε returned close to background levels

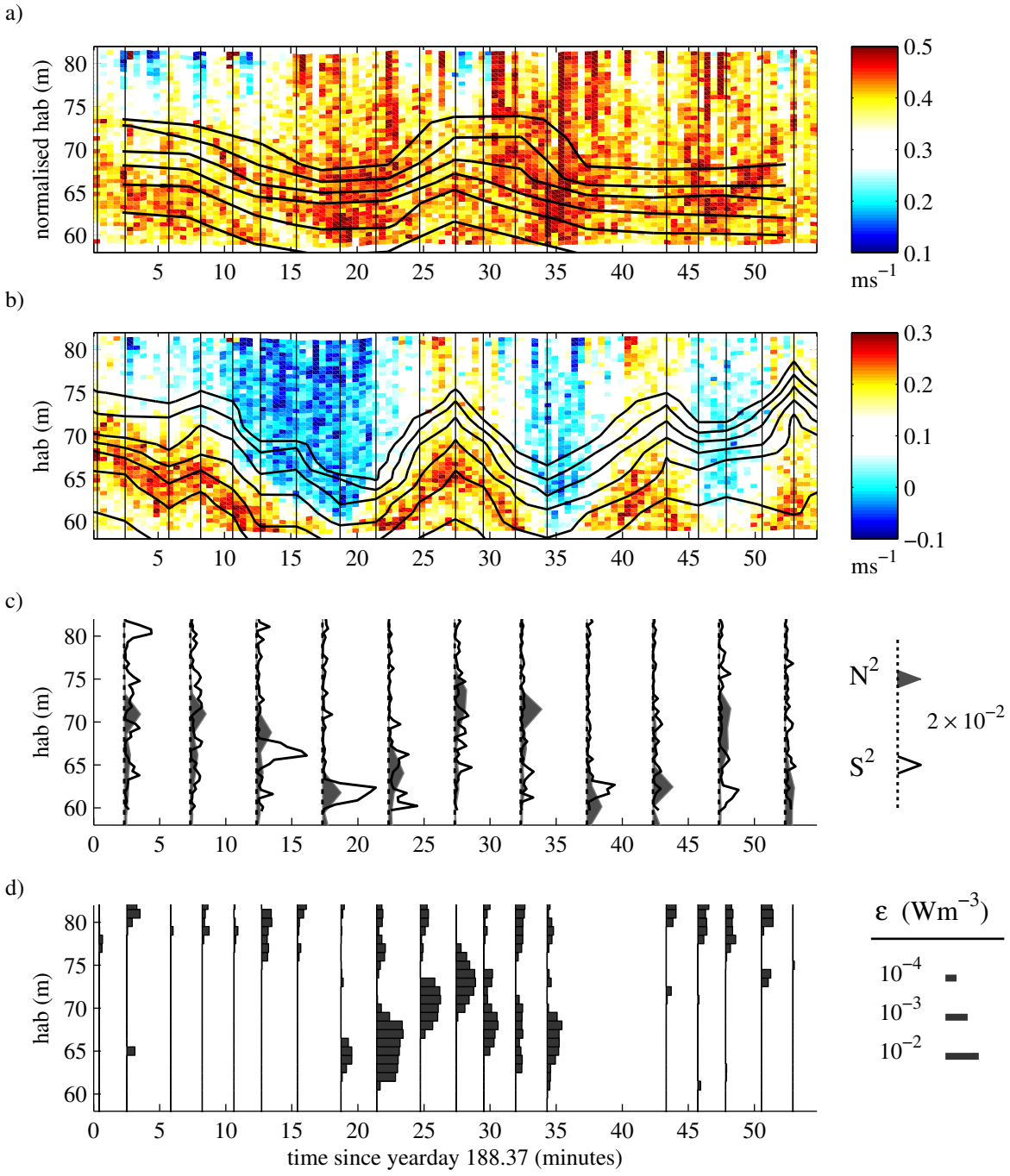

Figure 5.5: Plots of the vertical structure of shear, stratification and dissipation during the passage of NLIW packet. a) Northerly currents with overlaid moored data isotherms (12-15°C). b) Easterly currents with overlaid VMP measured isotherms (12-15°C). Vertical lines in a and b indicate the times of the VMP observations. c) 5 minute average vertical plots of N^2 and S^2 from the mooring. d) VMP observations of the rate of turbulent dissipation.

5.2.2 Generation zone

Measurement of the velocity and energy of internal waves in the Irish Sea is hindered by the presence of the strong barotropic tidal currents [Green et al., 2010], while this dataset is also limited by the limited vertical coverage of the current observations. However the distortion can be minimised by selecting a period when the barotropic tides are relatively weak. The first wave packet in figure 5.4 (day 177) occurs at a time of weakening easterly currents and spans a period when the dominant northerly currents were almost slack. The velocities and isotherms for this wave packet are plotted in figure 5.6.

Time mean profiles of the velocity for each component during the passage of the wave (indicated by vertical lines) are plotted next to the time series. The velocity vector is directed towards towards the WNW, suggesting that the waves propagate from the South East of the mooring location. The deeper Irish Sea channel is toward the South East as well as the tidal mixing front. The velocity vector has been plotted (figure 5.7) over a sea surface temperature satellite image from this time to indicate the position of the front and probable direction of wave propagation. Bathymetry for the region can be seen in figure 2.1.

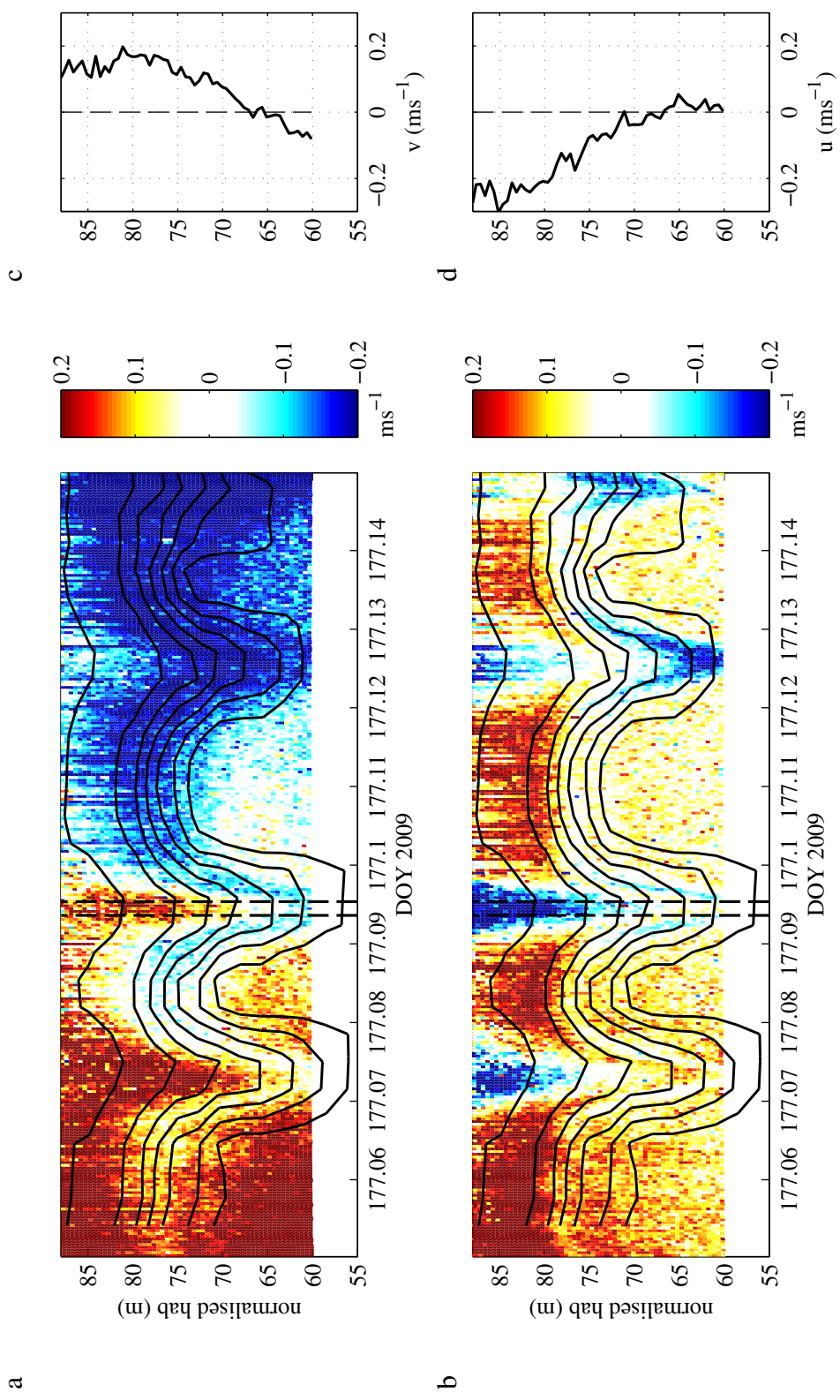

Figure 5.6: Observed velocity during a NLIW packet which occurred close to slack water. a and b) Northerly and Easterly currents with overlaid moored isotherms (10-14°C). c and d) mean velocity profiles (darkline)from the wave trough (region bounded by the dashed lines). Profiles corrected for the mean background flow (light lines) by subtracting the mean profile from before and after the wave (dotted lines).

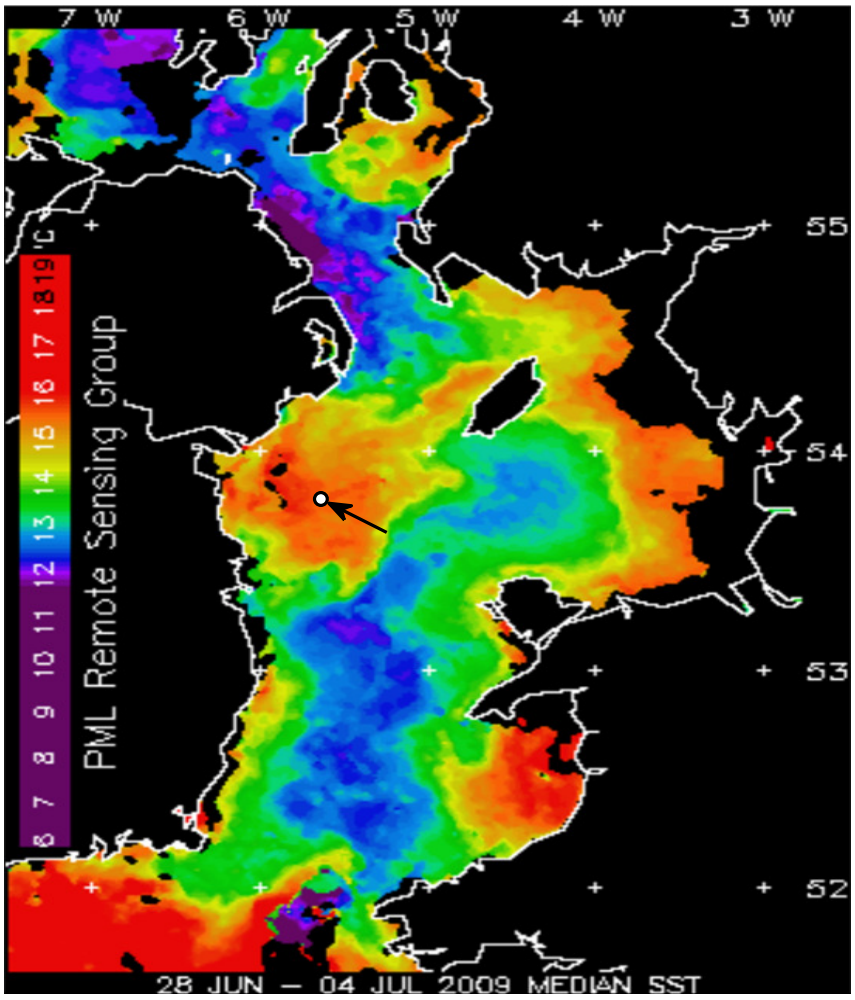

Figure 5.7: Map of SST indicating the possible origin of the observed NLIWs. Composite map of sea surface temperature for the period 28th of June to 4th of July (days 179 - 185). The stratified region is seen as the orange/red area close to the Irish coast. The circular mark indicates the position of the mooring. The arrow shows the direction of the NLIW propagation based on observed velocities measured in the wave trough. This suggests that the waves originate at the tidal mixing front to the south east of the mooring site which is 25 to 30km distant.

5.2.3 NLIW contribution to the thermcline mixing rate

The mean thermocline dissipation rate, ε_{th} (Wm^{-2}), was calculated by integrating the depth dependent TKE dissipation rate, ε (Wm^{-3}), between the heights of the 11°C and 15°C temperature contours. The time series of this is plotted on a linear scale as a bar graph in figure 5.8. The sum of this time series of dissipation divided by the total time over which it occurs ($\sim$ 48 hours) gives the $1\mathrm{mWm}^{-2}$ mean dissipation rate. The dissipation during the passage of the NLIW packet presented in chapter 5.2.1 is indicated by the darkly shaded bars and is responsible for approximately $0.35\mathrm{mWm}^{-2}$ of the total. There is also a suggestion that smaller spikes in the dissipation occur at times when thermocline motions due to NLIWs are present.

A serious issue which must be considered when the calculation of mean mixing rates collected from a floating platform was highlighted by the need to compress the VMP data to match the moored data (figure 5.6). This compression was required because the ships motion is affected by the passage of the waves as illustrated in figure 5.9. The position of the dots mark the ships position relative to the earth for each VMP cast while the color of the dot shows the depth of the 14°C isotherm. The position of the ship and the depth of the thermocline during the passage of the waves was as follows:

1. Initially the ship is drifting from the southeast to the northwest with the blue color of the dots indicating a shallow thermocline depth of 16m.

2. With the passage of the first wave the dots become red as the isotherms descend with a thermocline depth of over 30m. During this period the ships motion becomes westerly and the distance between casts increases as the ships drift speed increases and profiles take longer to complete.

3. As the isotherms ascend the dots become green the ships motion becomes more northerly and closer together due to reduced drift speed of the ship and compensation by the helm.

4. A similar pattern is observed for the second, smaller wave.

This distortion caused an over-sampling of this high dissipation event as the ship traveled in the same direction as the wave. Accounting for this over-sampling by compressing the data as before reduces the contribution of the wave by a factor 3 to $0.12\mathrm{mWm}^{-2}$. Applying this correction reduces the mean dissipation rate for the entire time series to $\varepsilon_{\mathrm{th}} = 0.8\mathrm{mWm}^{-2}$.

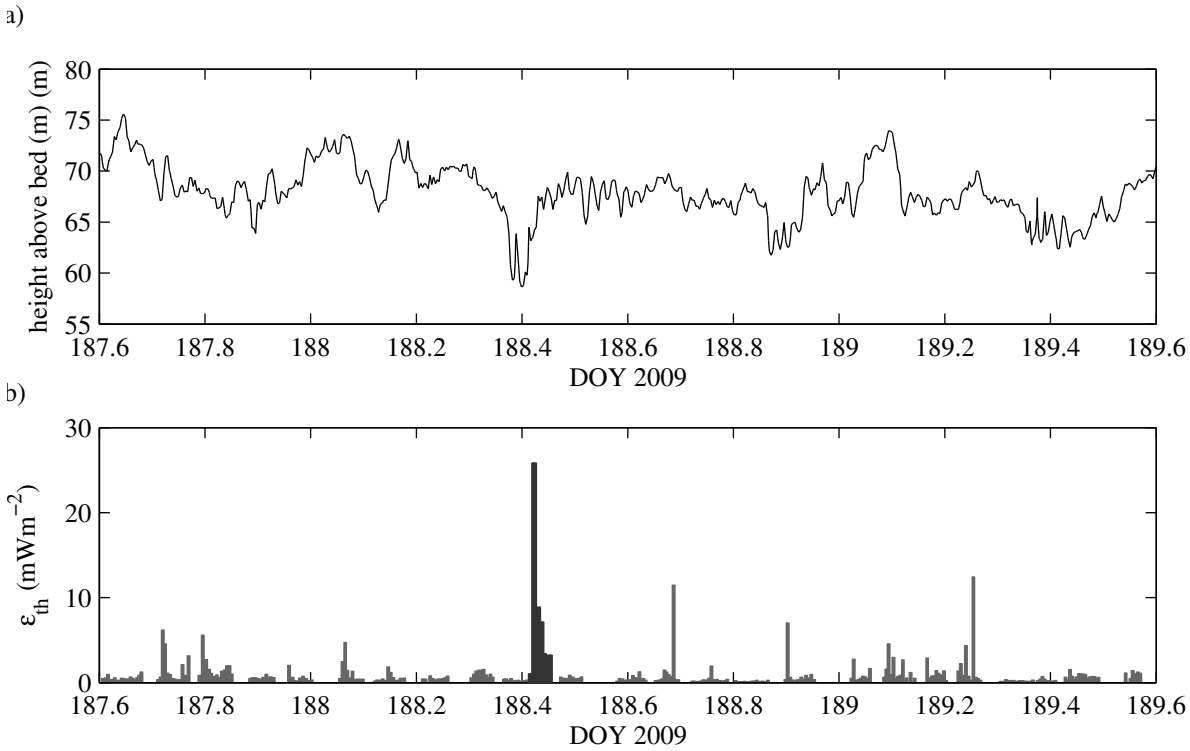

Figure 5.8: Plot showing the thermocline integrated dissipation rate and height of 12°C isotherm. a) plot of height of the 12°C isotherm. b) Time series of the integrated thermocline dissipation, darker bars indicate the dissipation generated by the NLIW presented in figure 5.5 which contributes ∼35% of the total dissipation.

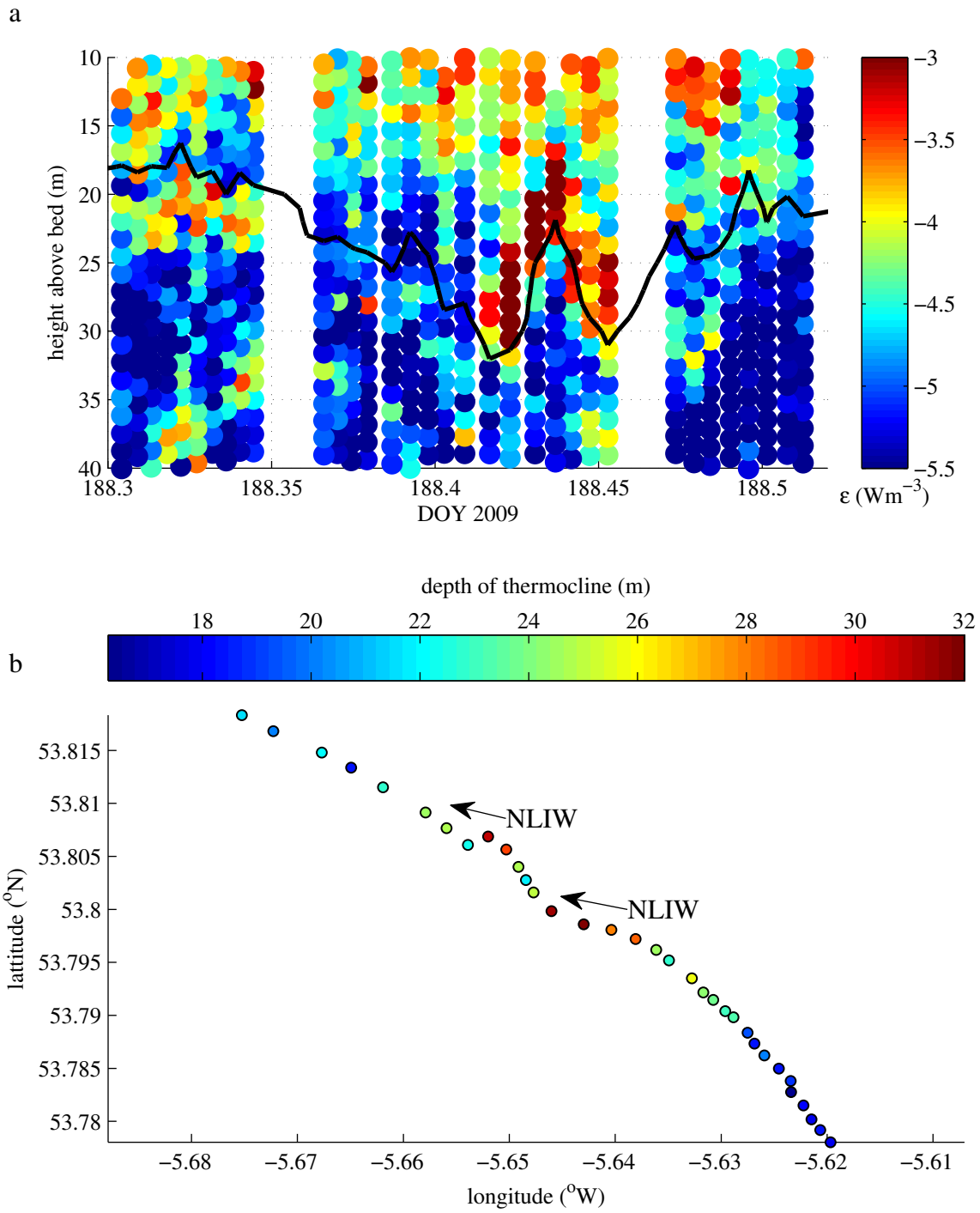

Figure 5.9: Plot showing the position of the ship during the passage of the NLIWs observed on day 188. a) scatter plot showing the rate of TKE dissipation and the height of the 14°C isotherm. b) position of the ship is shown by each dot while the colour of the dot indicates the depth of the 14°C isotherm plotted in pane a. The drift of the ship towards the northwest is interrupted by the passage of two NLIWs which caused the drift to the west to increase significantly, these are indicated by the arrows.

5.3 Summary

- The internal tide was predominantly mode one in structure at spring tides with velocity amplitude of 0.1ms^{-1} and isotherm amplitudes of 2.5m.
- After several days of strong mode one baroclinic tidal currents the vertical structure evolved to mode 2 and the associated baroclinic currents weakened.
- The mean energy flux calculated for the least squares fitted internal tide was only 15Wm^{-1}, but this increased to 34Wm^{-1} when the fitted first normal mode was used to generate a more realistic full water column velocity structure.
- The maximum energy available for mixing by the internal tide was estimated to be $\sim 0.3\text{mWm}^{-2}$ which is one third of the the total observed.
- Internal tidal shear alone was an order of magnitude too small to generate instabilities.
- Packets of NLIWs were observed once every tide and generated high frequency shear across the thermocline which was an order of magnitude above background levels
- The current velocities measured in the trough of the NLIWs were $\sim 0.5\text{ms}^{-1}$ directed towards the ENE.
- The likely generation zone for the NLIWs was tentatively identified as the tidal mixing front which lies $\sim 25-30$km ESE of the mooring site.
- A NLIW packet was observed to generate strong shear at the thermocline as the isotherms descended. This shear zone fragmented at the wave trough and high levels of turbulent dissipation were observed through the passage of the following wave.
- This single NLIW packet was responsible for approximately one third of the observed dissipation during the two days of observation. However this was exaggerated by the motion of the ship in the direction of wave propagation. Accounting for this Doppler shift reduced the proportion contributed by this NLIW packet by a factor of three.
- Internal waves in the Western Irish Sea have been seen to mix directly at the centre of the thermocline and are responsible for mid-water mixing which is absent from the models.

Chapter 6

$\Delta\Phi$ - Internal mixing from temperature structure

Two candidate mechanisms for mid-water mixing, inertial shear spikes and tidally generated internal waves, have been investigated in previous chapters and shown to bring about mixing in very different ways:

- Wind driven inertial motions were observed to be infrequent but energetic events which acted through shear spikes to generate shear instabilities which eroded the top of the thermocline. This form of boundary mixing rapidly deepened the surface mixed layer and generated a sharp density gradient and two layer density structure.
- Internal waves were less energetic but more persistent. They were present throughout the observations, and were strongest at spring tides. They have been shown to generate instabilities and elevated turbulent dissipation at the center of the thermocline. The density structure reflects the tendency of these internal waves to diffuse the thermocline with periods of strong internal wave activity accompanied by evolution of the vertical structure from two to three layered.

The presence of a diffuse thermocline has previously been cited as evidence for energetic mid-water mixing [Green et al., 2010; Rippeth, 2005]. This chapter intends to take this idea a step further by testing the hypothesis that the vertical structure can be treated as a record of the mixing history and may be used to estimate the rate of energy dissipated by internal waves through thermocline mixing.

6.1 Density structure

Four examples from the temperature record have been selected to illustrate the change in the vertical structure that occurred during the quiescent periods between wind-mixing episodes (Fig. 6.1). Profiles P1 and P3 immediately follow a wind-mixing event and have a two layer structure with a well mixed layer 20 to 25 m deep and a sharp thermocline (5m thick) separating the well mixed bottom layer. Profiles P2 and P4 show the typical stratification following a quiescent period some time after a wind event. The thermocline was then more diffuse (30 to 35m thick) with significant gradients in temperature extending from 50 mab to 85 mab. The diffusion of the thermocline between P1- P2 and P3 - P4 points to a source of interior mixing of which the most likely candidate is tidally generated internal waves. At times when the observed diffusion is primarily due to mixing by the internal waves then it may be possible to estimate the level of internal wave mixing using observations of the density structure alone.

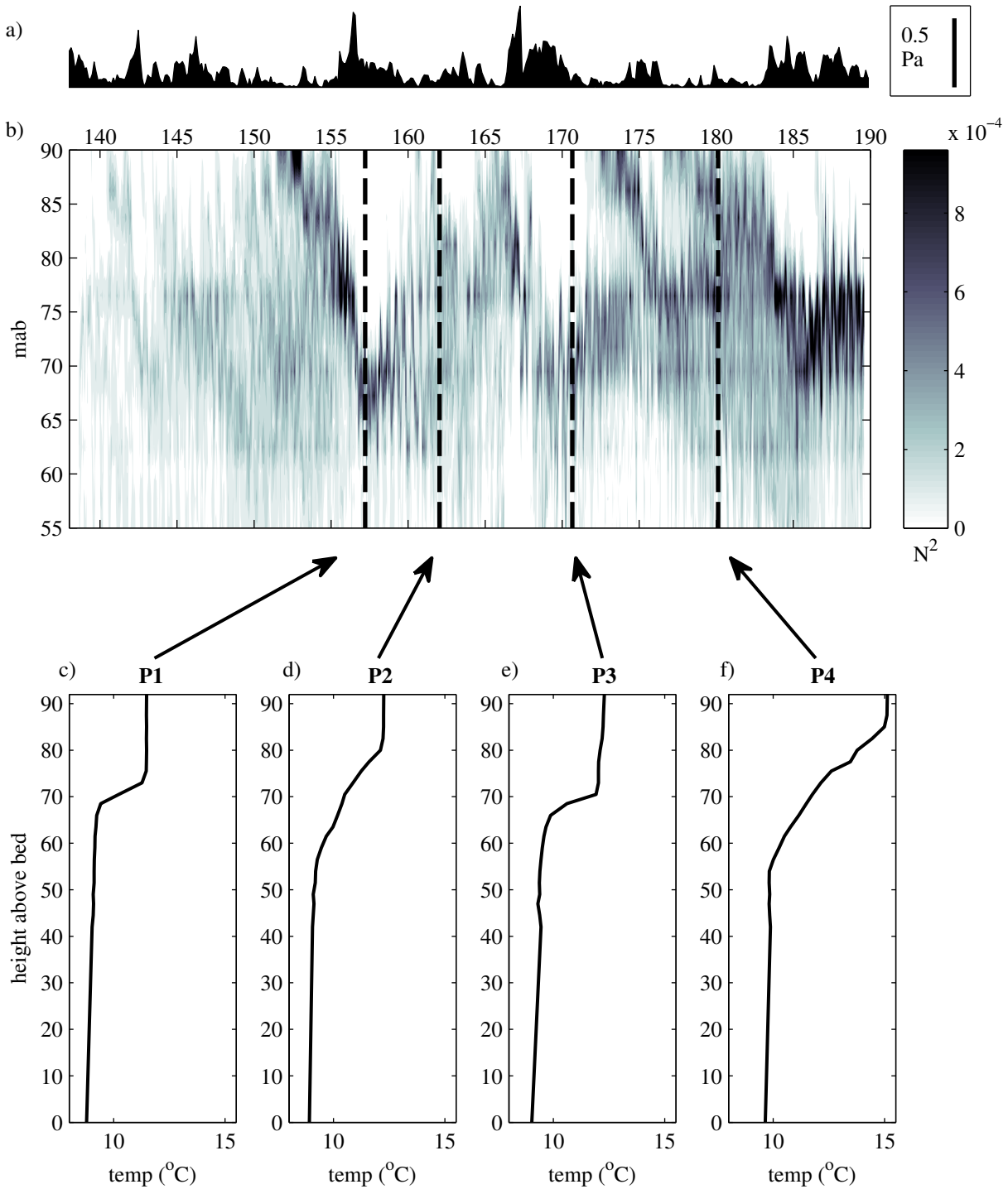

Figure 6.1: Examples of the vertical temperature structure through the mooring deployment. a) Wind stress calculated from the met office reanalysis model. b) Vertical structure of N^2 in the upper half of the water column. c/e) Examples of 2 layer structures observed after a wind driven inertial mixing event. d/f) Examples of diffuse thermocline observed after a quiescent period when internal wave mixing was dominant.

6.2 Quantifying diffusion of the thermocline

The strength of the vertical stratification at a location can be quantified using the potential energy anomaly [Simpson, 1981] but Φ alone tells us nothing of the vertical *structure* of the stratification. However if we assume that boundary mixing will tend to form a two-layer structure, then it is possible to use Φ to estimate energy dissipated through mid-water mixing by comparing with an equivalent two layer structure.

This method requires the construction of an two-layer density profile which has the same heat content (Q) as the observed density profile. The procedure for constructing the two layer profile is as follows: The temperature in the surface and bottom layers are calculated as the average temperature in the upper 10m of the water column, T_s, and in the lower 40m T_b. The depth of the thermocline in the two-layer case is then tuned to allow Q_{2layer} and Q_{obs} to match. If salinity is a significant contributor to stratification then surface and bottom densities may be used and a total mass balance used instead. The PE of such a two layer structure will be lower than for the observed structure since PE has been gained through the mid-water mixing, therefore Φ_{2layer} will be higher since more energy is required to fully mix the water column.

The essential idea is that the increase in water column potential energy due to mid-water mixing may be quantified by calculating the difference between the energy required to fully mix the observed and the two layer equivalent density structure. The potential energy added to the water column through mid-water mixing, $\Delta\Phi$, can therefore be estimated as the difference between the observed structure, Φ_{obs}, and the two layer equivalent, Φ_{2layer}:

$$\Delta\Phi = \Phi_{2layer} - \Phi_{obs} \tag{6.1}$$

As an illustration of the method, profiles P1 and P2 are plotted with their equivalent two layer structure in figure 6.2. The potential energy anomaly for each structure is indicated on each profile and as expected Φ_{2layer} is greater than Φ_{obs} with the difference between the two being equal to $\Delta\Phi$. Profile P1 is an example of a regime where boundary mixing by wind and tide predominate and so the two layer equivalent structure is similar to the observed profile resulting in a relatively small amplitude for $\Delta\Phi$ of 1.1Jm^{-3}. After a week of low wind stress the observed profile P2 was observed, Φ_{obs} increased by only 30% between the two profiles, however $\Delta\Phi$ increased by over 300% indicating an energy input of (3.8Jm^{-3}) due to mid-water mixing.

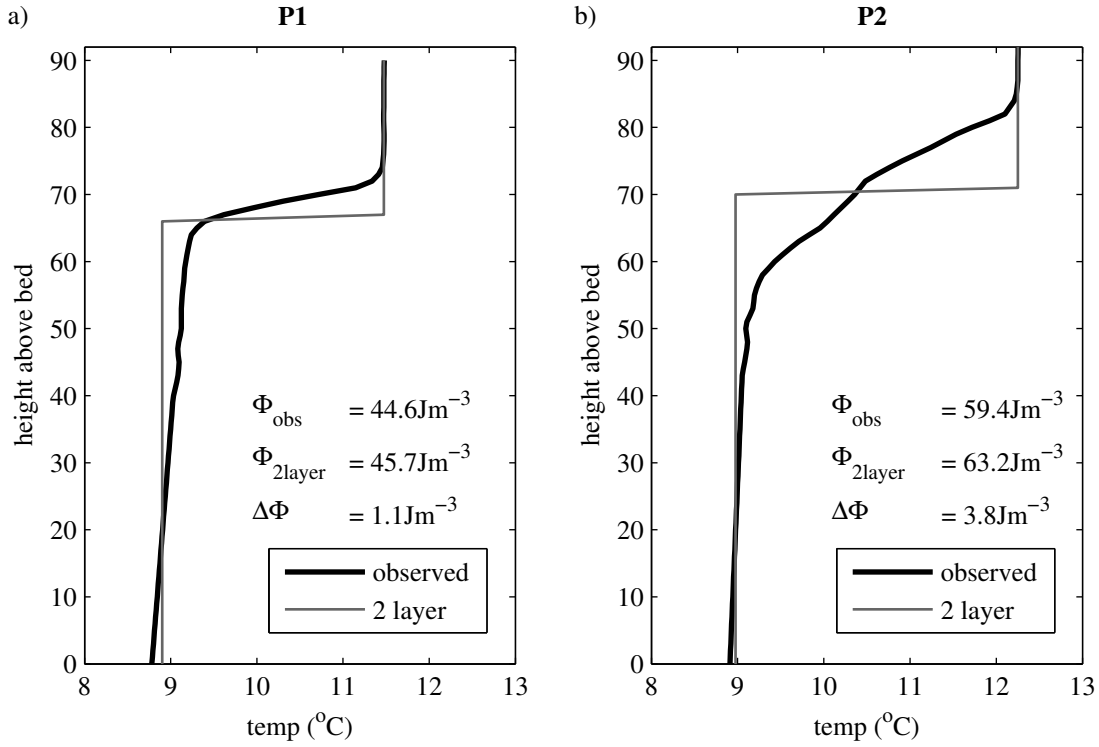

Figure 6.2: Examples of two layer and three layer temperature profiles and their two layer equivalent, heat balanced temperature profile. a) Example of an observed and two layer temperature profile after a wind mixing event (day 157). b) Example of an observed and two layer temperature profile after a quiescent period (day 162).

6.3 Application to a time series

In order to test the principle behind ΔΦ we applied it to the Irish Sea 2009 dataset explored in previous chapters. Thermocline broadening was evident during a period dominated by internal wave activity and we have direct measurements of the rate of diffusion to compare to.

An hourly time series of equivalent two layer density structures was constructed and Φ_{2layer} time series calculated from these. Φ_{obs}, Φ_{2layer} and ΔΦ are plotted along with the wind stress in figure 6.3. The pattern of Φ as described in chapter 3.1 is of a general increase with falls observed at times of high wind stress. Φ_{2layer} follows the same pattern as Φ_{obs} but increased faster during quiescent periods before converging again during wind mixing events. This pattern is quantified by ΔΦ which rises from day 138 to 155 before dropping close to zero with the first major mixing event. The wind mixed the surface layer to a uniform density and the difference between the observed structure and equivalent two-layer stratification was at a minimum. As winds stress declined the thermocline broadened again and Φ_{2layer} increased faster than Φ_{obs} so that ΔΦ increased again. On day 166 strong winds returned and the density structure became two layer and ΔΦ decreased rapidly again. This pattern of almost linear rise and abrupt drops in the value of ΔΦ was observed three times in the time-series. These rises relate to quiescent periods, when wind mixing allowed the diffusion of the thermcline to be recorded in the temperature structure, and have been labeled I, II and III.

If we assume that ΔΦ represents the energy contained in buoyancy which has been lost to mixing by internal waves then $d(\Delta\Phi)/dt$ is a measure of the effective rate of mid-water mixing by internal waves. i.e. the slope of ΔΦ during periods I - III represent the effective thermocline mixing rate. The rates for periods I - III were calculated as, 0.53mWm^{-2}, 0.69mWm^{-2} and 0.63mWm^{-2} respectively. These effective mixing rates can be related to the observed dissipation by a mixing factor which is generally accepted to be a maximum of ∼0.2 [Osborn 1980]. Therefore the thermocline dissipation rates required to generate this diffusion would be ε_{th} = 2.5 - 3.5 mWm^{-2}. This is an unexpected result because it is approximately 3 times the directly observed levels of dissipation obtained during the VMP measurements presented in chapter 4.3.

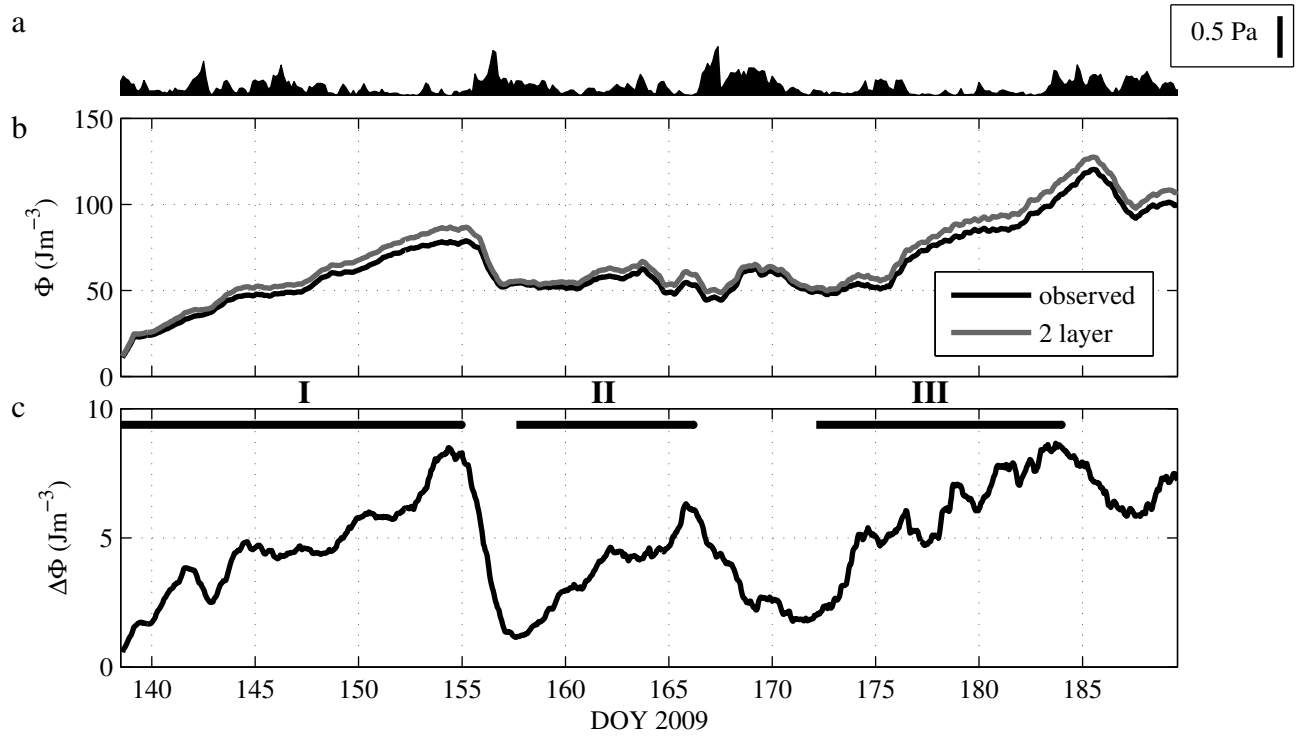

Figure 6.3: Time series of internal mixing rate, ΔΦ for the Irish Sea 2009. a) Met office reanalysis modeled wind stress. b) The potential energy anomaly Φ_{obs} (black line) and the two layered equivalent potential energy anomaly Φ_{2layer} (grey line). c) The internal mixing parameter ΔΦ calculated as the difference between the plots in pane b).

6.4 Testing using 3 layer model

The diffusion of the thermocline is greater than can be explained by the measured dissipation rate with a mixing efficiency of 0.2. So unless these measurements are lower than the mean thermocline levels (which seems unlikely since they come from a period of spring tides), some other process must be responsible for the observed thermocline broadening. In order to investigate the broadening effect a simple model has been adapted so that it can be used to test whether the record of vertical density structure is effective in recording the levels of vertical mixing.

The model is an adaptation of the Simpson and Bowers [1984] two layer model which uses basic energy considerations to generate a two layered density structure using seasonal winds and heat input and a constant tidal energy input. In its original form the model assumes that all the energy available for vertical mixing of heat is inputed at the surface and at the bed. Modifications were made to the model to introduce energy to the mid-water region to simulate the mixing action of internal waves. This energy was prescribed as a rate of TKE dissipation, ε_{th}, with 20% of this energy available for increasing the PE of the water column. An analytical approach to distributing this energy was taken and is outlined as follows:

- The store of energy available for diapycnal mixing (DPE) was calculated by multiplying the rate by the time-step and adding any residual energy from previous steps.
- The depth bin with the largest change in temperature was identified and chosen as the height to input the energy.
- The energy required to fully mix the bins either side of the chosen bin was calculated by estimating the change in Φ.
- If there was sufficient available energy in the DPE to mix this the calculation was repeated for additional bins either side of the chosen bin until there was insufficient energy to mix any further bins.
- The largest number of bins for which there was sufficient energy to mix were then mixed by setting them all to the mean temperature the chosen bins.
- Any additional energy left over after mixing these bins was added to the store of DPE for use in the following time step.

6.5 Simulation of temperature structure using seasonal winds

A seasonal simulation using smoothed seasonal winds and a constant tidal stream amplitude ($U = 0.41 ms^{-1}$) was generated by running the model with a mid-water energy input of $\varepsilon = 1 mWm^{-2}$. The effect of the mid-water mixing was to reduce the density gradient at the the interface between the well mixed upper and lower layers (see fig 6.4b). The broadening of the thermocline was greatest early and late in the year when stratification was weaker so that the mid-water energy was more effective. However the diffusion of the thermocline was limited to approximately 5m due to the uniformity of the prescribed seasonal winds. The constant wind mixing persistently eroded the top of the diffusing thermocline and limited the rate of effective mixing recorded by $\Delta\Phi$ to $0.04 Wm^{-2}$, just one fifth of the expected signal. Since the limiting factor on thermocline diffusion was the the wind mixing, $\Delta\Phi$ peaked at the time of minimum wind speed.

The model was modified to mix the surface layer using the met-office reanalysis winds (section 2.2.3) in order to replicate the observed quiescent periods. During such periods mid-water mixing is subject to less competition from wind mixing eroding the upper boundary of the thermocline. Likewise competition from tidal mixing erodes at the lower boundary of the thermocline and varies with a spring neap cycle. In order to replicate the variation in the tidal mixing the tidal stream velocity was varied using the tidal fit to the barotropic currents.

To test the effect of the mid-water mixing on the density structure the model was run first with no internal mixing and then with $\varepsilon_{th} = 1 mWm^{-2}$. The two resulting time series of temperature for the deployment period have been plotted in figure 6.5c and d along with the observations in pane b. The pattern of vertical temperature structure is well reproduced by the model, with periods of surface heating punctuated by high wind stress events and mixed layer deepening on days 155, 167 and 184. The magnitude of Φ (pane e) is broadly reproduced. Drops in the magnitude of Φ are reproduced although all changes are less pronounced in the model, presumably due to the use of seasonal values for cloud cover and air temperature. This is evident, for example, during the period from days 155 to 175 which may have been cooler and cloudy so the model overestimates the growth in Φ.

The staircase pattern observed in $\Delta\Phi$ is generally reproduced by the model although the magnitude is smaller. The surprising result is that running the model without any mid-water mixing produces the same pattern in $\Delta\Phi$ with only slightly reduced magnitude. Examining the vertical structure of temperature in more detail it becomes obvious why this is the case.

During quiescent periods, e.g days 157 to 167, there is a marked diffusion of the thermocline around 60mab due to the prescribed mid-water mixing. However at the same time surface heating generates a new shallow thermocline which has the effect of making the original thermocline appear broader than

it is due to the mid-water mixing alone. Later in the time series, (e.g. 183) the effect is significant with stratification extending from the surface down the the lower thermocline, which is a remnant of the last large wind mixing event. Figure 6.6 illustrates the effect by plotting vertical profiles for the observations and the two model outputs from day 180. The observed profile, P4, plotted in pane a is a good example of a diffuse thermocline with a single linear density gradient from 60mab up to 85mab. The temperature profile from the same day produced by the model running with $\varepsilon_{\text{th}} = 1\text{mWm}^{-2}$ is plotted in pane b and looks similar to the observed profile although without such a smooth gradient. The model running without any mid-water mixing produces three distinct thermocline's, two remnant thermocline's from previous wind mixing events and the shallowest recent thermocline. The magnitude of $\Delta\Phi$ for the model running with mid-water mixing and the observations are almost the same while $\Delta\Phi$ for the model without the mid-water mixing is only 5% lower.

The results from the model suggests that the dominant process in generation of a broad thermocline in the Irish Sea is not the level of mid-water mixing but the distribution of heat by variable wind mixing. With the constantly blowing seasonal winds, heat is always mixed down to meet the top of the bottom boundary layer, but with the quiescent periods present during realistic winds heat is retained close to the sea surface giving the illusion of thermocline broadening. This explains why the observed signal in $\Delta\Phi$ is much larger than can be explained by the observed dissipation levels. It also suggests that a diffuse thermocline cannot be used as definite evidence for energetic mid-water mixing.

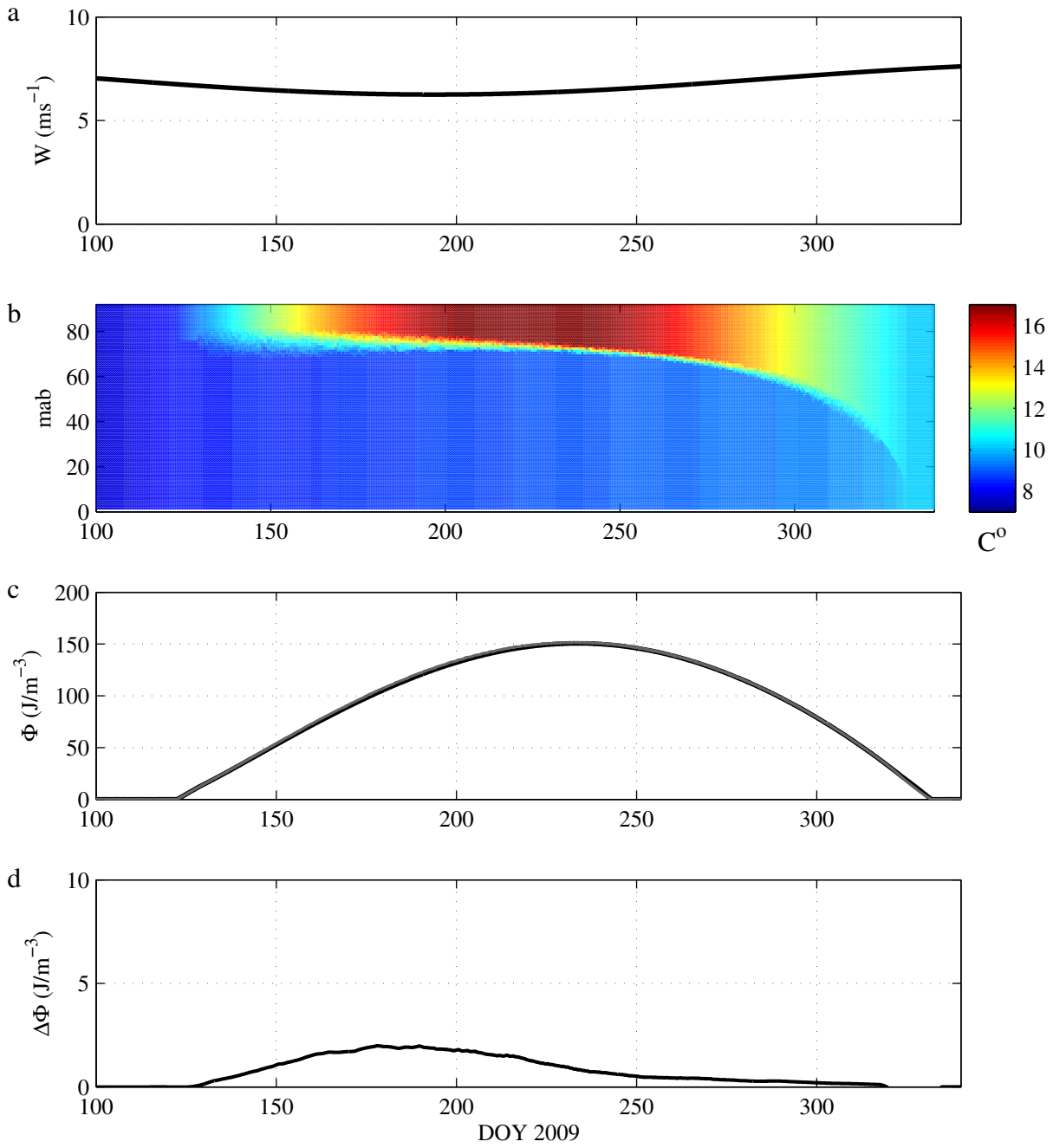

Figure 6.4: Irish Sea seasonal cycle modeled using heating stirring model with addition of mid-water mixing. a) seasonal average wind speed used to generate surface layer mixing. b) Temperature structure generated by running model with constant tidal mixing ($U = 0.41 ms^{-1}$), seasonal winds plotted in pane a, and mid-water mixing at a rate of $1 mWm^{-2}$. c) potential energy anomaly Φ calculated for the temperature output plotted in pane b. d) $\Delta\Phi$ calculated for the model output.

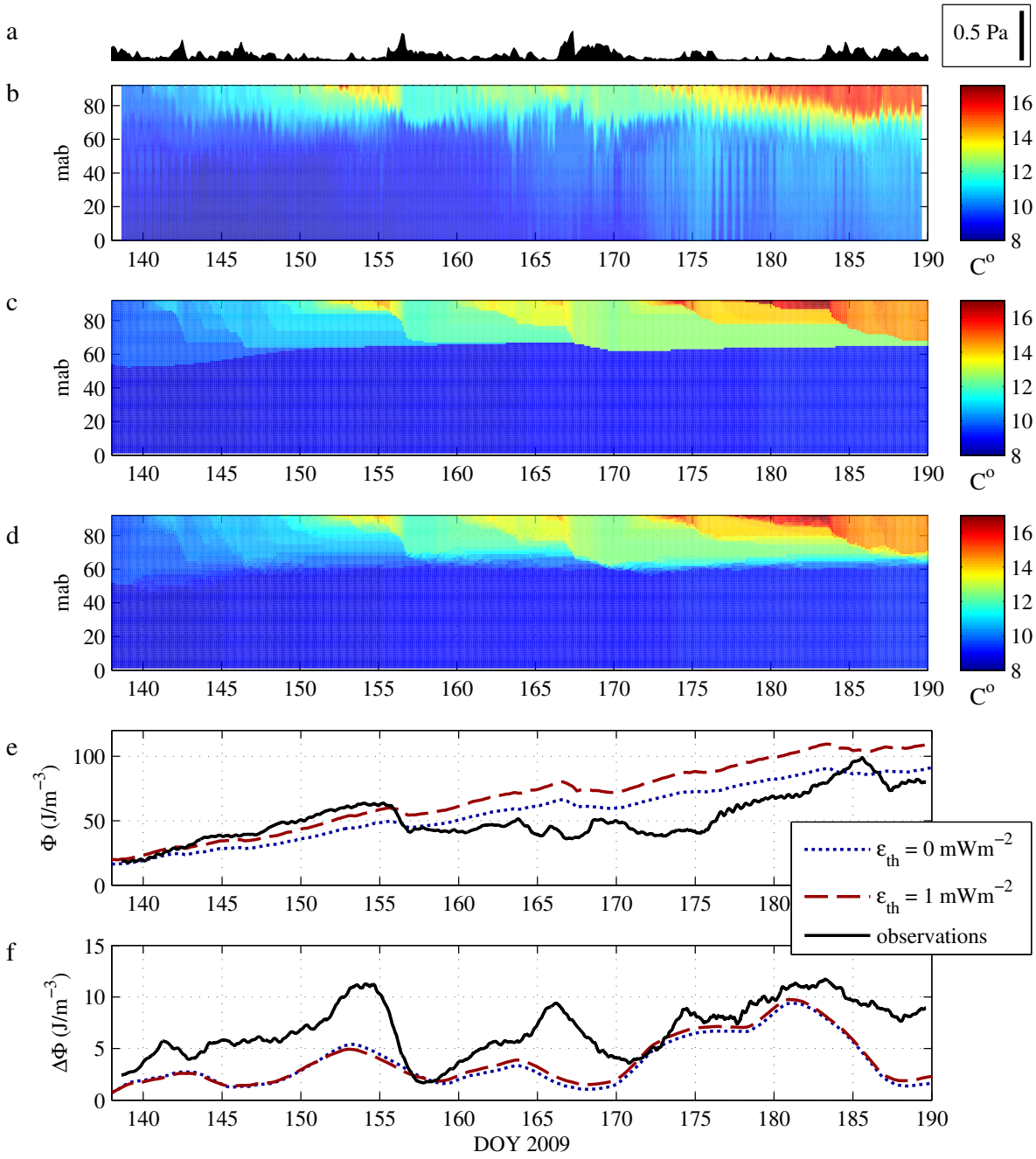

Figure 6.5: A comparison between the observed temperature structure and output from heating stirring model runs with realistic wind and tidal mixing and with mid-water mixing. a) met office reanalysis winds used to calculate the energy available for surface layer mixing. b) observed temperature structure for the entire mooring deployment. c) temperature structure from heating-stirring model with no mid-water mixing. d) temperature structure from heating-stirring model with $\varepsilon_{th} = 1\text{mWm}^{-2}$ mid-water mixing e) Φ calculated for the above three temperature structure time-series. f) $\Delta\Phi$ calculated for the above three temperature structure time-series.

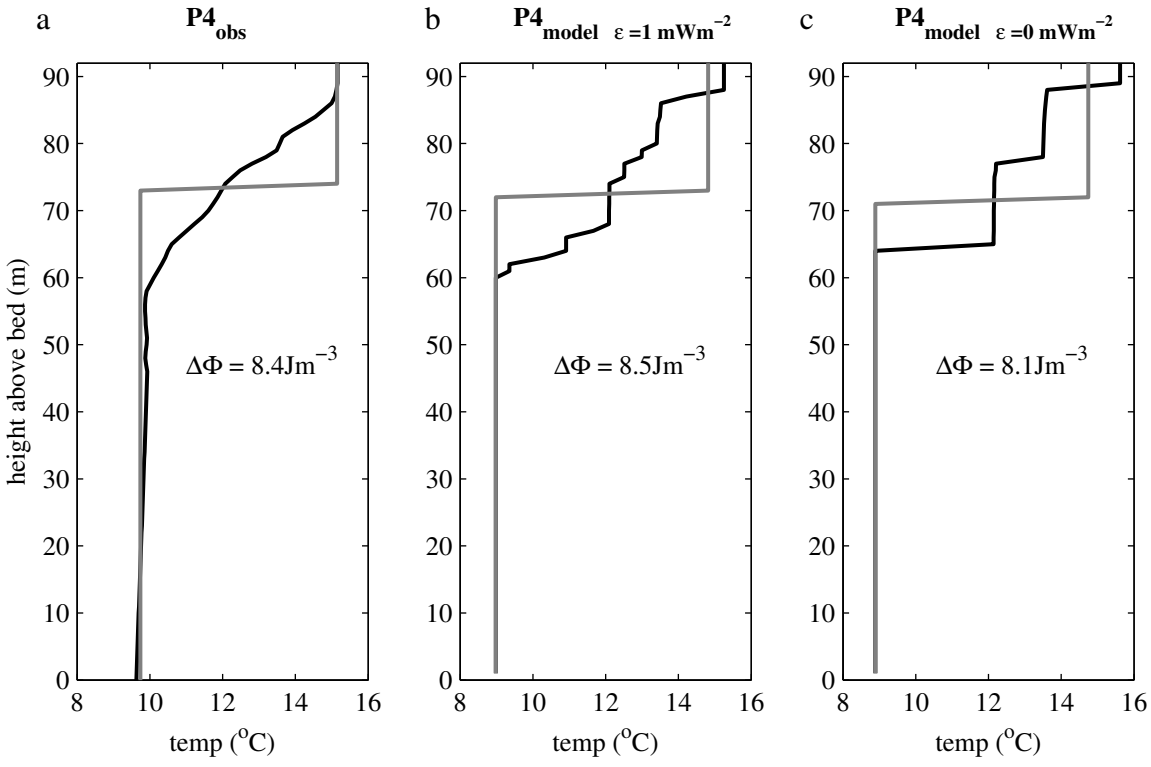

Figure 6.6: Examples of diffuse temperature structures and their two layer equivalent from observed and modeled time series on day 180. a) Observed temperature structure (black line) and its two layer equivalent (grey line). b) Modeled temperature structure with $\varepsilon_{th} = 1\text{mWm}^{-2}$ of mid-water mixing (black line) and its two layer equivalent (grey line). c) Modeled temperature structure with no mid-water mixing (black line) and its two layer equivalent (grey line).

6.6 Application of $\Delta\Phi$ to a spatial data-set

Strong surface heating limits the value of using $\Delta\Phi$ in time-series analysis but it may still be valid for use in certain spatial applications. The shelf break is recognised as a region of strong internal wave generation and direct measurements of dissipation by Green et al. [2010] showed that mid-water dissipation rates were two orders of magnitude higher there than they were on-shelf. There is therefore potential to use $\Delta\Phi$ to quantify the decay length scale of the waves and estimate their rate of mixing using the observed density structure. An example of such observations is presented in figure 6.7 which shows a transect of temperature data collected using a towed (undulator) CTD. The transect runs from the Celtic Sea shelf break over 100km onto the shelf. The vertical temperature structure is very diffuse close to the shelf break with density gradients occupying the observed part of the water column. On-shelf the vertical structure is strongly two layered. The transition from broad to narrow thermocline is reflected in $\Delta\Phi$ which falls from 30Jm^{-3} close to the shelf break down to 0Jm^{-3} 90km onto the shelf.

There are several reasons why $\Delta\Phi$ has greater validity in this scenario; The region covered by the data is likely to have experienced the same net meteorological forcing and since measurements were collected within a $\sim 24h$ period the data is essentially a snapshot of the temperature structure. This implies that the levels of surface heating and wind mixing which have acted upon the water column across the region are equal. The contribution to $\Delta\Phi$ from surface heating and wind mixing are therefore expected to be uniform across the transect and appear as a constant offset in the signal. This suggests that the observed variation in $\Delta\Phi$ may be attributable to variation in mixing by internal waves. However variation in the strength of barotropic tidal mixing may also be significant, so it is important to rule this out as a major contributor to the signal in $\Delta\Phi$.

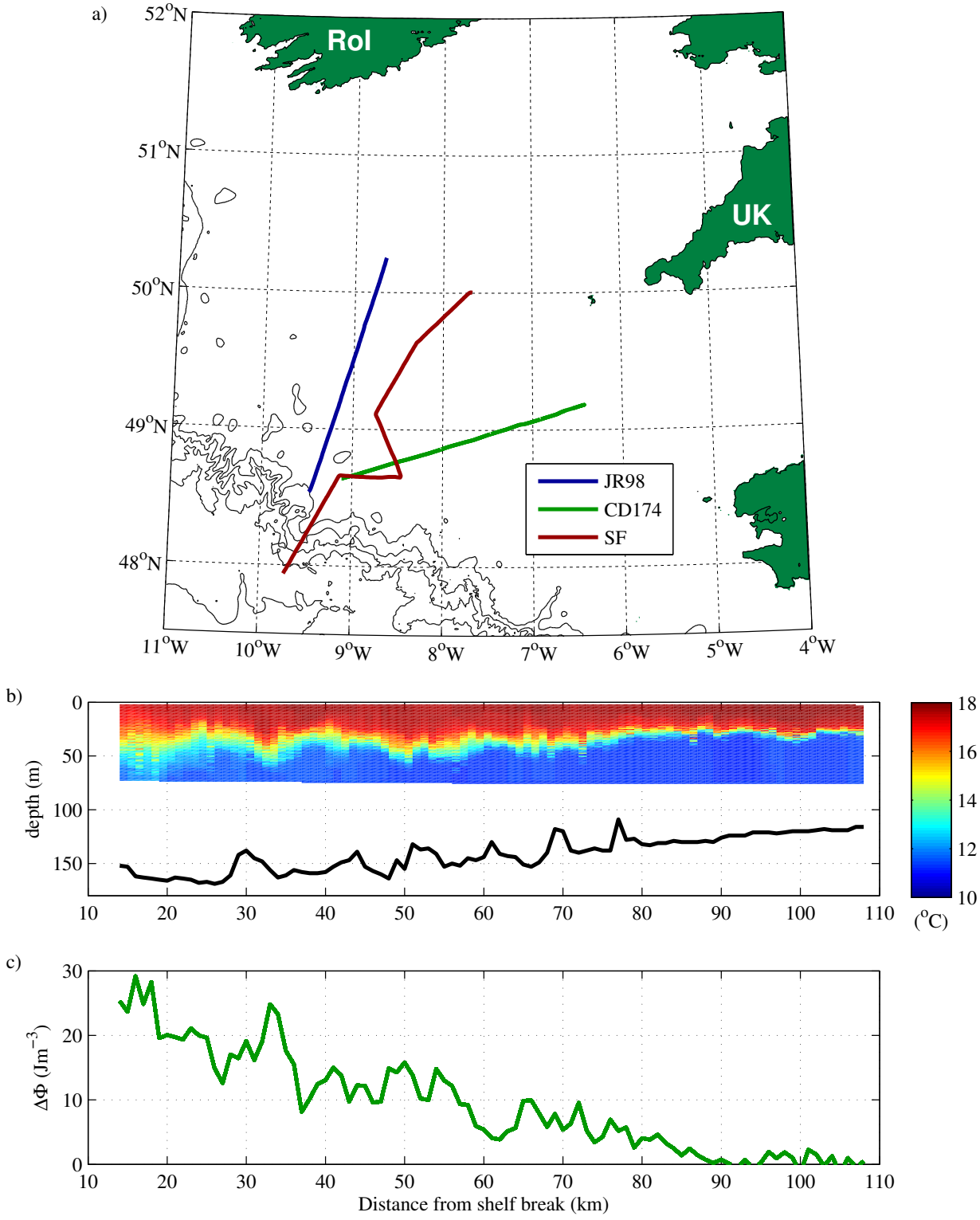

Figure 6.7: Towed (undulator) CTD transects in the Celtic Sea. a) The location of three transects in the Celtic Sea. b) Vertical temperature structure plotted as function of distance from the shelf break for transect CD174. Sea bed depth indicated by black line. c) ΔΦ as a function of distance from the shelf break for transect CD174.

6.6.1 Variation in barotropic tidal mixing

The M2 component of the barotropic tidal velocities along the transect were extracted from a simulation using the OSU Tidal Inversion Software [Egbert et al., 2010]. The resulting velocity profile was interpolated to 4km intervals and is plotted in the top panel of figure 6.8. The velocity is lower off-shelf, but once on-shelf it remains constant at 0.4ms^{-1}. This means that the variability in the strength of tidal mixing is dependent only on changes in the depth. The depth decreases almost linearly from 200m to 120m through the transect. The reduction in tidal mixing quantified by h/u^3 is therefore also linear, falling by approximately 25% over the transect (fig6.8b). The effect of this reduction in mixing was tested by running the heating-stirring model with a range of depths (200m to 120m every 4m) and using the modeled barotropic velocities. A uniform mid-water mixing rate of $\varepsilon_{\text{th}} = 1\text{mWm}^{-2}$ was used so that any variation in $\Delta\Phi$ resulted only from the changes in barotropic tidal mixing. A transect comparable to the observations was then generated by extracting the vertical temperature profile from each model run on the same day as the observations were made (day 220). The resulting transect of temperature and $\Delta\Phi$ calculated from it are plotted in figure 6.8c. Across the transect the thermocline was generally fairly narrow (10m) and this was reflected in the small magnitude $\Delta\Phi$. However there was a trend in $\Delta\Phi$ moving on-shelf, with a reduction from $\sim 5\text{Jm}^{-3}$ down to $\sim 2\text{Jm}^{-3}$ over 90km. However the trend in $\Delta\Phi$ represents only 10% of the observed variation implying that variation in barotropic tidal mixing is not responsible for the observed signal.

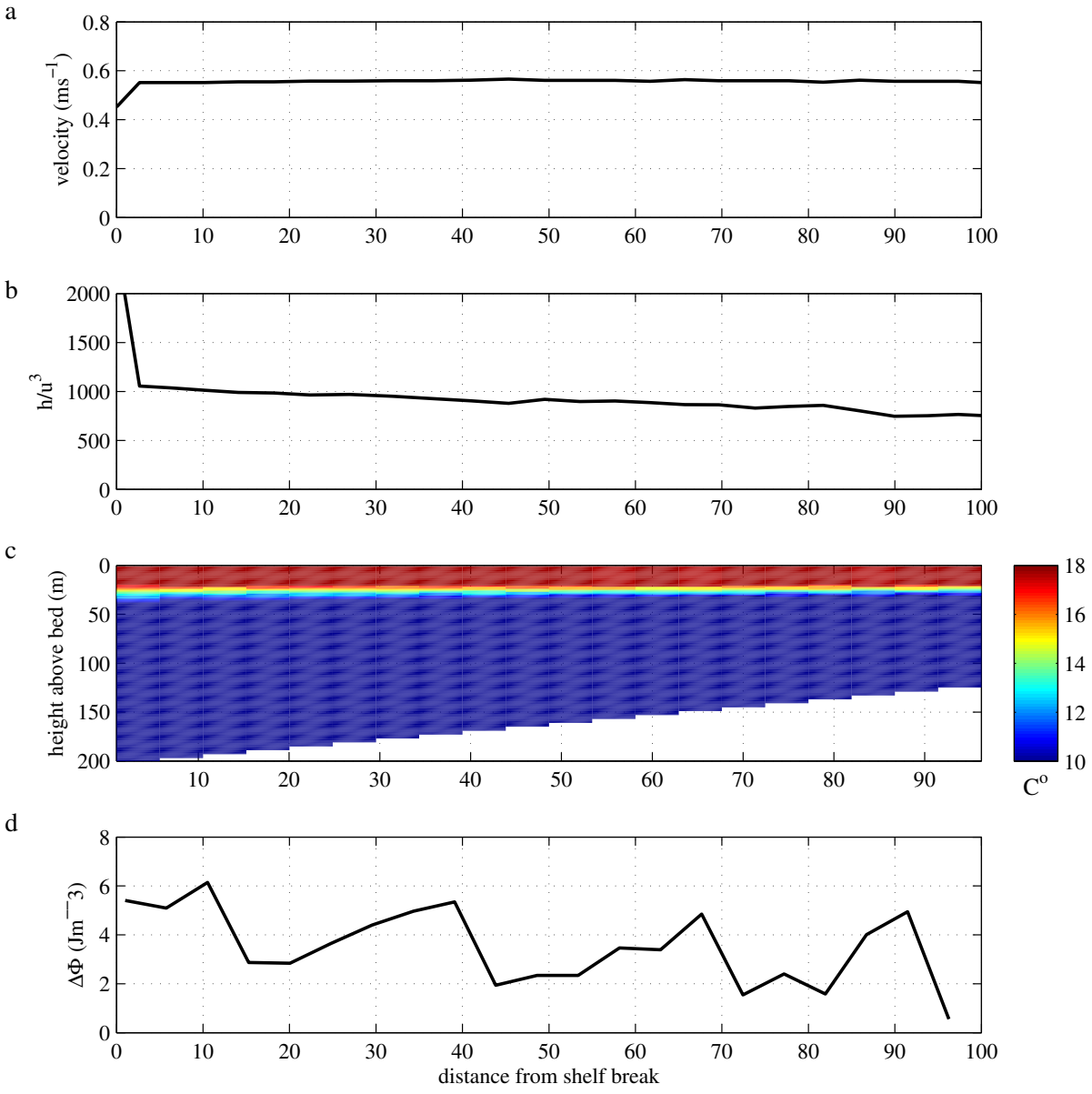

Figure 6.8: Modeled on-shelf transect of temperature structure with uniform mid-water dissipation rate of $\varepsilon_{th} = 1\text{mWm}^{-2}$. a) M2 component of barotropic tidal currents from OTIS model simulation. b) tidal mixing parameter h/u^3 c) temperature transect generated from 20 model simulations using heating stirring model with uniform mid-water mixing and variable tidal mixing. d) ΔΦ calculated from modeled temperature transect.

6.6.2 Variation in mid-water mixing

Baines [1982] estimates that the on-shelf propagation of internal wave energy flux in the Celtic Sea is $\sim 300-560\mathrm{Wm}^{-1}$. To test if this level of energy is sufficient to generate the observed pattern in $\Delta\Phi$ the model was run as in the previous example of an on-shelf transect. However, this time the level of mid-water dissipation was varied with distance from the shelf break. The dissipation profile used in the model was generated by using a quadratic decay law. As described in equations 5.1 - 5.2 the internal wave energy flux is, $E_f \propto \frac{1}{2}\rho u_{IW}^2$, is proportional to the square of the wave amplitude while the rate of mid-water TKE dissipation is proportional to the cube of the wave amplitude $\varepsilon_{th} \propto u_{IW}^3$. If it is assumed that internal wave energy is converted to dissipation at a constant rate λ then equation may be formed to relate the internal wave energy flux to the rate of thermocline dissipation:

$$\varepsilon_{th} = \lambda E_f^{\frac{3}{2}} \tag{6.2}$$

Making the assumption that all the internal wave energy is lost to mid-water dissipation then $\varepsilon_{\mathrm{th}} = -\mathrm{dE}/\mathrm{dx}$ we can form the following differential equation:

$$\frac{dE_f}{dx} = -\lambda E_f^{\frac{3}{2}} \tag{6.3}$$

Which may be solved as follows:

$$E_f^{-\frac{3}{2}}.dE_f = -\lambda.dx \tag{6.4}$$

Integrating gives:

$$-2E_f^{\frac{1}{2}} = -\lambda x + c \tag{6.5}$$

At the shelf break x=0 and $\mathrm{E_f} = \mathrm{E_0}$ therefore $\mathrm{c} = 2/\sqrt{\mathrm{E_0}}$. Rearranging equation 6.5 in terms of $\mathrm{E_f}$ gives an expression for the internal wave energy flux as a function of distance from the shelf break:

$$E_f = \left(\frac{2}{\lambda x + \frac{2}{\sqrt{E_0}}}\right)^2 \tag{6.6}$$

The rate of decay, λ, was calculated for a range of shelf break energy fluxes, $\mathrm{E_0} = 100\mathrm{Wm}^{-1}$, $200\mathrm{Wm}^{-1}$ and $400\mathrm{Wm}^{-1}$ by using an estimated value of $\varepsilon = 10\mathrm{mWm}^{-2}$ based on measurements of dissipation from the Celtic Sea shelf break [Green et al., 2010] and the Malin Shelf [Inall et al.,

2000]. Equation 6.6 was then used to calculate transects of E_f from 0 - 100km on-shelf for each level of energy input was then used with its corresponding decay rate. Equation 6.3 was then used to generate dissipation profiles from these flux profiles. The resulting transects of ε_{th} are plotted in pane a of figure 6.9. The lower energy flux profiles decrease faster due to higher λ required to generate the required level of mid-water dissipation at the shelf break.

The ε_{th} profiles were applied to the the model and a transect of temperature profiles generated in the same way as described in the previous section (chapter 6.6.1). The temperature transects are plotted in panes b-d of figure 6.9 and $\Delta\Phi$ is plotted for each modeled transect and for the observed transect in pane d. All three model runs generated close to 40Jm^{-2} at the shelf break with broadening of the thermocline which occupies the top third of the water column. Moving on-shelf the $E_0 = 100\text{Wm}^{-1}$ modeled transect rapidly loses energy and $\Delta\Phi$ falls to 10% of its peak after 40km with a profile which is essentially two layered. The $E_0 = 200\text{Wm}^{-1}$ modeled transect generated broadening and elevated $\Delta\Phi$ to 60km on-shelf. The $E_0 = 400\text{Wm}^{-1}$ modeled transect generated significantly elevated $\Delta\Phi$ to 80km on-shelf reaching the level of numerical noise after 95km. $E_0 = 400\text{Wm}^{-1}$ was most successful in reproducing the observed profile of $\Delta\Phi$. The decay rate of internal wave energy required to achieve this result gave an e-fold scale of $\sim 50km$.

The model was run with seasonal winds since observations were not available. This limitation tends to reduce the value of $\Delta\Phi$ as wind mixing erodes the top of the thermocline. However since the on-shelf observations have a well mixed surface layer with no evidence of elevated surface temperatures, like those observed in the Irish Sea time series (chapter 6.3), it is safe to assume that some level of wind mixing also occurred prior to the observations.

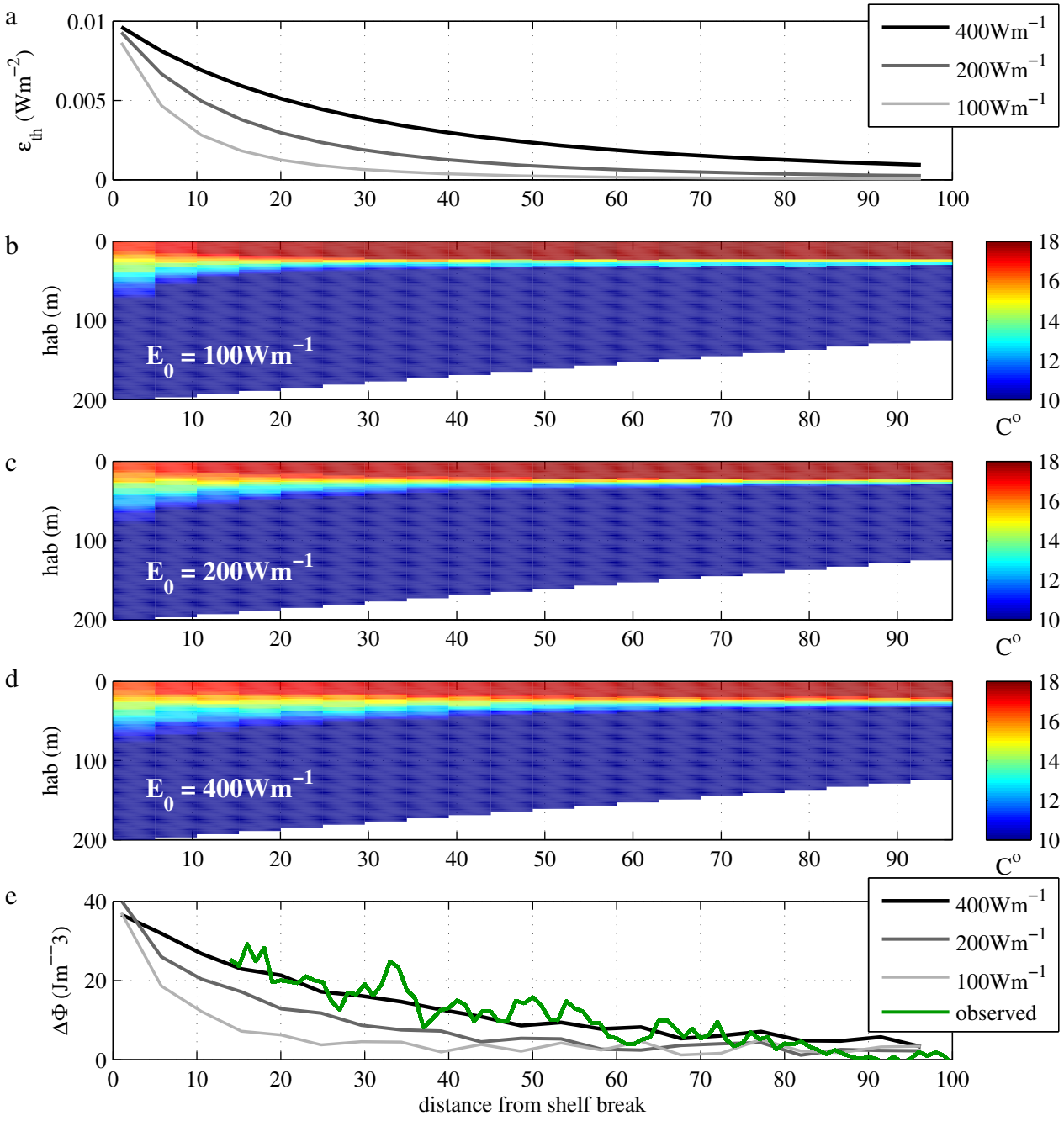

Figure 6.9: Comparison of the signal in ΔΦ for a range of different energy fluxes using heating stirring model with mid-water mixing. a) Profiles of ε_{th} for a range of energy fluxes generated using equations 6.3 & 6.6. b-d) Temperature structure transects generated with the heating stirring model with the ε_{th} profiles plotted in pane a. e) ΔΦ calculated from the observations (transect CD174) and the modeled transects plotted in panes b-d.

Other transects of vertical temperature structure do show evidence of strong surface heating during quiescent periods. The path of transects JR98 and SF (plotted on figure 6.7) display the same narrowing of the thermocline on-shelf (not plotted), however they do not have the perfect two layer profile of transect CD174. This is reflected in their profiles (fig6.10a) of ΔΦ which never reach zero, even far onto the shelf. This is due to the thermocline broadening effect of surface heating in the absence of wind stress (see chapter 6.5, an effect which will affect the entire transect. Removing the on-shelf constant removes the heating effect and brings the profiles of ΔΦ closer together (figure 6.10c). However, close to the shelf break ($<$ 20km) the signals do diverge from one another and also deviate from the general trend of increase due with proximity to the shelf break. Examining these transects and the ΔΦ calculation it becomes clear why this deviation occurs, strong mixing in this region mixes cool water right to the surface. The reduced surface temperature, T_s is used for construction of the equivalent 2 layer structure and is lower than a true two layer structure would be in the absence of mid-water mixing. The result is that $\Phi_{2layer}$is underestimated and so therefore is ΔΦ. The effect is greater the longer that broadening has been occurring for. eg. highest for transects with large ΔΦ magnitudes.

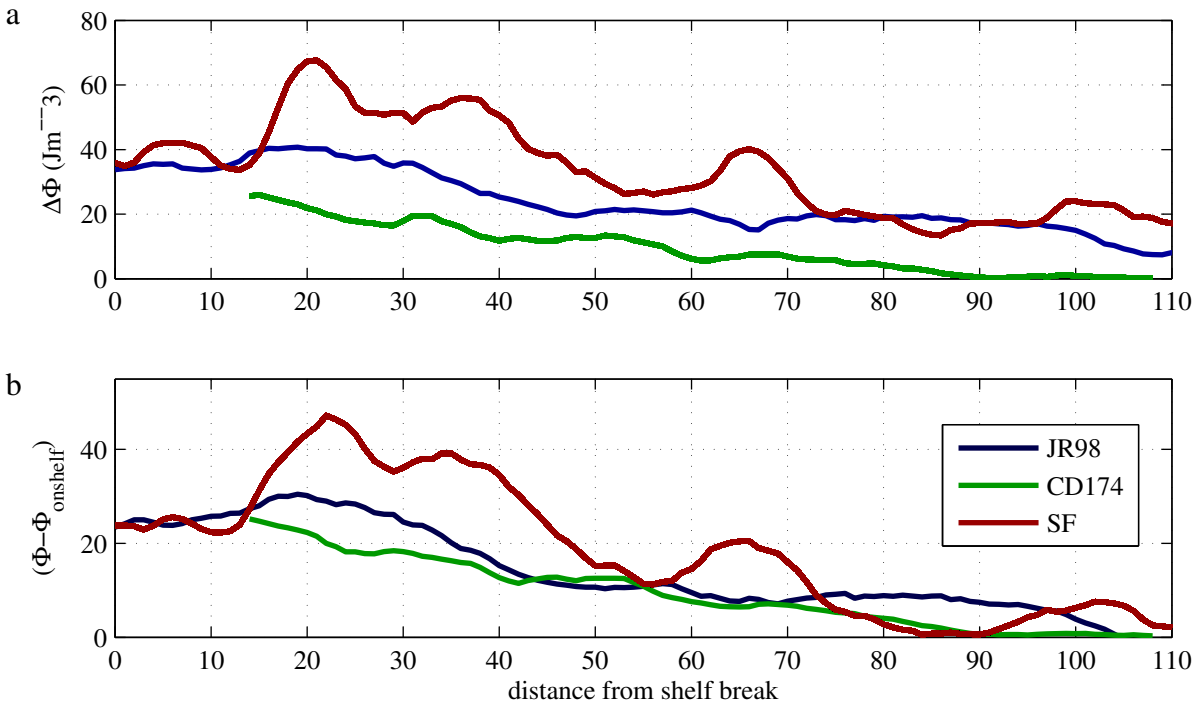

Figure 6.10: On-shelf profiles of ΔΦ calculated for the three transects plotted in figure 6.7. a) Unadjusted ΔΦ for the three transects. b)ΔΦ with on-shelf constant removed.

6.7 Application of $\Delta\Phi$ to CTD database

The use of $\Delta\Phi$ with transects of data overcomes the issue of surface heating on the assumption that meteorological conditions are the same across the region. For measurements separated in time by more than a few days the contribution to $\Delta\Phi$ due to wind mixing and surface heating may vary significantly. However if there is sufficient sampling spatially and temporally then these differences should average out to reveal a mean pattern in $\Delta\Phi$.

The BODC (British Oceanographic Data Centre), which has a large database of CTD profiles available online, was searched for a suitable region bounding the shelf break with intensive CTD sampling. The Celtic Sea was rather sparsely surveyed so the Malin shelf off the west coast of Scotland was chosen. The region is quite well surveyed and thermocline integrated dissipation rates at the shelf break are high ($14.6 - 28.3 \mathrm{Wm}^{-2}$ [Rippeth, 2005]). A total of 2010 CTD casts were extracted from the database for the region 55.5°N - 58°W, 10°W - 7°W but a number of steps were required to determine those which were suitable for calculating $\Delta\Phi$.

Removing measurements which were off-shelf (deeper than 200m) and those in less than 80m or in a sheltered location left a total of 720 CTD casts. Φ was calculated for these casts and profiles where $\Phi < 10 \mathrm{Jm}^{-3}$ were discarded leaving 360 usable profiles. There was significant variation from month to month between the $\Delta\Phi$ magnitudes so just a single month was examined. June was the most heavily sampled month with 80 CTD casts from 8 different years, however many observations are from the same location so the spatial distribution is rather poor. The position of these casts is plotted in figure 6.11a with the colour of each plot relating the the normalised $\Delta\Phi$ magnitude. Generally $\Delta\Phi$ is observed to have high magnitudes close to the shelf break and low magnitudes far onto the shelf. The minimum distance of each CTD cast from the shelf break was calculated and figure 6.11b presents a plot of $\Delta\Phi$ as a function of this. The relationship is similar to that observed for the Celtic Sea transects with $\Delta\Phi$ falling to close to zero 80km onto the shelf. There is considerable variability in the observations but 77% of these fall within one standard deviation.

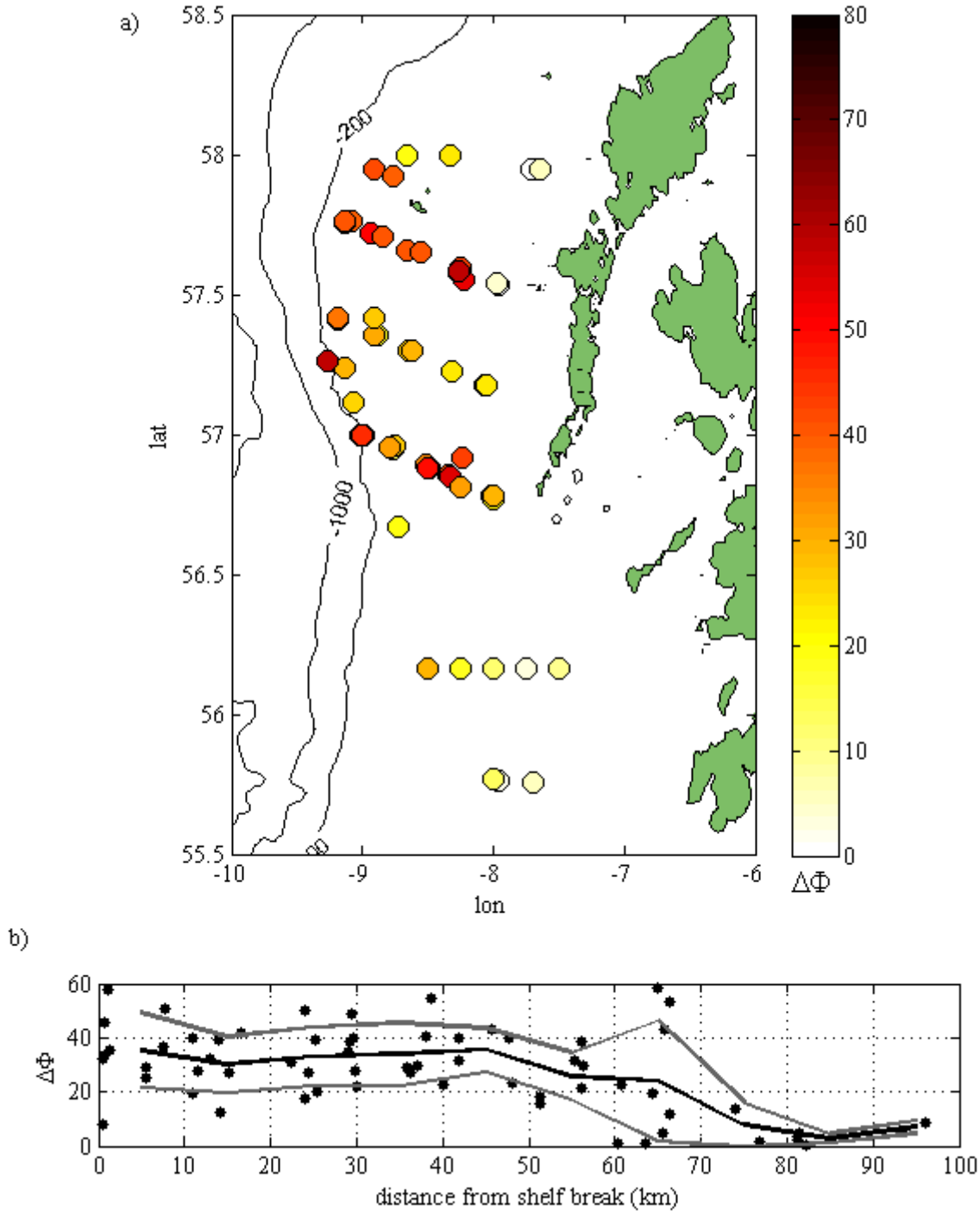

Figure 6.11: ΔΦ calculated from CTD data from data collected from a number of different years. a) Position and magnitude of CTD profiles. b) ΔΦ as a function of distance from the shelf break for the CTDs plotted in pane a. Average ΔΦ calculated every 10km is plotted (black line) along with one standard deviation above and below this (grey lines).

6.8 Summary

- Broadening of the thermocline was observed during quiescent periods between wind mixing events.
- Thermocline broadening was quantified using $\Delta\Phi$, which is calculated as the difference between the observed potential energy anomaly Φ_{obs} and the potential energy anomaly of an equivalent two layer structure Φ_{2layer} with the same heat content.
- The slope of $\Delta\Phi$ for the Irish Sea 2009 time series suggests that $2.5-3.5 mWm^{-2}$ of mid-water TKE dissipation is required to explain the thermocline broadening. This is approximately three times the measured rate of dissipation.
- Application of a simple mixing model demonstrated that the observed pattern in $\Delta\Phi$ could be reproduced without the addition of any mid-water dissipation. The broadening observed could be produced by using realistic wind forcing. During quiescent periods surface heat input formed new shallow thermoclines. This restratification is what generated the broad thermocline structure and the subsequent pattern in $\Delta\Phi$.
- To overcome the problems associated with heat input $\Delta\Phi$ was applied to a region where there were very high levels of dissipation due to internal waves. Synoptic datasets were used so that net meteorological forcing would be constant. Towed CTD transects from the Celtic Sea showed that close to the shelf break $\Delta\Phi$ was high but decreased rapidly with distance on-shelf, reaching zero within 80-100km on-shelf as vertical structure became 2 layered.
- A simple mixing model demonstrated that the on-shelf trend in $\Delta\Phi$ could not be explained by changes in tidal mixing strength due to the decreasing water depth.
- There were differences in magnitude and offset of $\Delta\Phi$ for different transects, but this could be reduced by subtracting the on-shelf constant. However, reduced surface temperatures within 20km of the shelf break due to strong mixing bringing cooler water up from below caused a reduction in $\Delta\Phi$ which makes it less reliable in this region.
- A modeled transect of temperature using a range of different energy flux inputs suggested that $400\mathrm{Wm}^{-1}$ was sufficient to explain the observed differences in vertical structure and the pattern in $\Delta\Phi$.

- Single CTD measurements from a number of years from the Malin shelf exhibited a reduction in $\Delta\Phi$ with distance from the shelf break. suggesting that despite variations due to different meteorology if sampling is sufficient then these variations can average out.

Chapter 7

Summary and Discussion

This thesis presents a time-series of velocity and temperature observations, accompanied by ship-bourne turbulence meaurements, from the seasonally stratified Western Irish Sea in the spring and early summer of 2009. The purpose of these measurements was to gain greater understanding of mixing in the thermocline by the wind, through inertial oscillations and by the tide, through internal waves. These two shear generation processes were candidates for the anomalous mid-water mixing which is absent in our best attempts at physical modelling.

Both candidates have previously been observed separately in the Irish Sea [Green et al., 2010; Rippeth et al., 2009]. However during this long time series the dominant process generating shear shifted from one to the other several times, revealing differences in the way each brings about mixing and the resulting changes they bring about in the vertical structure of temperature

7.1 Inertial oscillations and shear spikes

Inertial currents in the surface layer with a magnitude of $0.3ms^{-1}$ were generated by the wind on average every 2 weeks, which was $\sim 50\%$ more frequent than predicted for the Irish Sea in summer by Sherwin [1988]. Two of these wind driven events saw shear spikes generated by the interaction between wind stress and surface currents as observed by Burchard and Rippeth [2009] in the North Sea. The spikes we observed in the Irish Sea were equal in magnitude to the observations but less persistent, lasting only a few days. The Burchard Rippeth model was able to describe the generation of the spikes in the Irish Sea, with maximum shear production occurring when wind and bulk shear vectors aligned although the magnitudes were less than observed. One interesting feature of this interaction, revealed by plotting the motion of the surface layer, is that peak shear occurs when the surface layer is in motion 90° to the right of the wind. In the Irish Sea this translates to ~ 3.75

hours after wind and bulk shear vectors align. Another important consequence of the interaction is that peak shear magnitudes during the inertial events did not occur when the wind stress was at a maximum; instead the largest spikes were caused by changes in the wind direction or magnitude. This demonstrates that to predict the correct level of shear during wind driven mixing, the models must be able to replicate inertial shear spikes.
Despite being the most energetic low frequency baroclinic energy source we observed, and generating the strongest shear in the time-series, several pieces of evidence lead us to the conclusion that inertial shear spikes are not responsible for anomalous thermocline mixing:

- A 1D dynamical model with turbulence closure scheme reproduced the observed shear spikes without the need for any additional physics or high resolution winds (3 hourly was sufficient). However, the same model was incapable of reproducing the elevated levels of turbulent dissipation which were measured in the thermocline region.

- Shear spike episodes were accompanied by rapid mixed layer deepening. This deepening led to a change in the vertical structure of stratification from 3 layer, with a diffuse thermocline, to 2 layer with a sharp thermocline. This suggests that rather than mixing in the mid-water, shear spikes act as a form of boundary mixing as in the traditional shelf sea paradigm for wind driven mixing. The observations from the original study supports this view with a strongly 2 layered vertical temperature structure throughout the shear spiking period.

- The mooring recovery cruise was delayed due to high seas caused by the strong winds which generated shear spikes. Previous observations of anomalous mid-water mixing were also made from such ships (often in quiescent conditions) and so in these measurements the elevated mixing observed in the thermocline is unlikely to be caused by inertial shear spikes.

The way in which the shear spikes act to bring about mixing of the water column was well captured in detail thanks to the high vertical resolution mooring observations. Inertial motions were slab like with the surface mixed layer moving in phase, generating strong shear at the base of the mixed layer. At the beginning of shear spike episodes the strong shear generated by the spikes at the base of the mixed layer were sufficient to lower the gradient Richardson number to one quarter so that the top of the thermocline became unstable and mixing occurred. Each of these early spikes entrained fluid from the thermocline up into the mixed layer deepening it in a series of steps. However as the mixed layer deepened the interface became sharper and the buoyancy frequency increased, so that, despite having a larger magnitude, later spikes did not generate the instabilities or the associated deepening.

A search of the literature found that intermittent mixed layer deepening by inertial currents had been documented before, although in modelling rather than observational studies. Mellor [1975] applied a constant wind stress to a stationary water column and generated peaks in kinetic energy every inertial period which coincided with potential energy gains, due to entrainment of thermocline water into the mixed layer as it deepened. The paper study also noted, as hinted at in our observations, that there was zero turbulent mixing below the thermocline due to this process. Klein and Coste [1984] used a similar model setup and describes the entrainment of nutrients into the mixed layer every inertial period as the interaction between wind stress and surface currents generated shear instabilities which eroded the top of the thermocline. While these effects have been observed in models it is only recently that observations have become sophisticated enough to see them in the ocean.

7.2 Internal waves

With inertial shear spikes ruled out as the source of anomalous thermocline mixing, internal waves were investigated as the primary candidate. Tidal period internal waves were found to be the primary source of low frequency shear during spring tides when wind stress was low generating baroclinic currents of $0.1ms^{-1}$ and isotherm displacements of $\sim 5m$. The strongest currents were apparent during the early part of spring tides when a mode 1 structure was evident. Our estimates of the flux of internal tidal energy, 34 Wm^{-1} were considerably less than previous calculations [Green et al., 2010] and could be due to differences in method or in the location. Our estimate of the maximum energy flux leaves a shortfall in energy required to explain the 1mW of observed thermocline dissipation. After several days operating as a mode 1 wave the internal tide evolved into a mode 2 wave with characteristics of a three layered structure evident. The presence of higher modes is consistent with previous observations in the Irish Sea where considerable energy was found in modes other than the first [Green et al., 2010].

The shear associated with internal tide alone was insufficient to overcome stratification and generate instabilities in the thermocline. However, non-linear internal waves were also present in our observations. These also occurred at spring tides and arrived in packets of up to 6 waves. The shear associated with these NLIWs was up to two orders of magnitude greater than that from the internal tide and of sufficient magnitude as to generate instabilities in thermocline. One wave train observed during the July cruise generated strong shear which resulted in extreme rates of turbulent dissipation. This packet of waves was present for only half an hour out of 48 hours ($\sim$0.5%) but accounted for one third of the total thermocline dissipation. Our observations of the high frequency waves share many characteristics those observed in a number of different shelf seas [Moum et al., 2003; Mackinnon and

Gregg, 2001], although these are generally associated with generation at the continental shelf break. The Irish Sea does not border a shelf break but current velocities in the wave trough suggest that the solitary waves originate from the East of the region. Whether the generation of the waves is due to some topographic feature or the front itself is a question of interest. The small length scales and patchy, intermittently energetic nature of internal wave mixing which we have observed provides a challenge for both quantifying and reproducing them. These features are likely to continue to be sub grid scale in shelf sea models for some time and with this in mind an observational approach to the problem was explored, which may be of use in developing a parameterisation for internal mixing.

7.3 Internal mixing from temperature structure

The turbulent dissipation we observed that was generated by the NLIWs was centred on the thermocline acting to diffuse the vertical gradient in temperature and generating a broader thermocline. This led to the hypothesis that the transition in vertical structure from two to three layers, during a low wind stress period coinciding with spring tides, was caused by the tidal and solitary internal wave activity observed. The differing effects of wind and internal wave mixing meant that the vertical temperature structure could provide a record of the recent mixing history. The central idea for the calculation of internal mixing is that in the absence of mixing by internal waves, wind driven mixing would dominate and a two layer structure would form, whilst in the absence of wind driven mixing, internal waves would act to diffuse the thermocline. Based on this premise $\Delta\Phi$ was defined as the difference in energy required to fully mix the observed water column and the energy required to mix a 2 layer structure with the equivalent heat content, $\Delta\Phi = \Phi_2 layer - \Phi_{obs}$.

Quantifying the internal mixing rate was initially promising with constant increases in $\Delta\Phi$ during quiescent periods when internal waves were dominant. However the actual rate of energy input measured using $\Delta\Phi$ was three times greater than that which was measured directly. It seemed unlikely that our measurements could be unrepresentative of the average mixing rate, however previous observed rates [Green et al., 2010] were within 50% of ours. The alternative was that some other unknown process was causing the thermocline diffusion. In order to test the effect of different levels of internal mixing on vertical temperature structure we modified the [Simpson and Bowers, 1984] model of vertical heating and stirring. The model originally mixes only from the boundaries using wind and tidal energy but a third input of energy was added directly at the thermocline in order to simulate mixing by internal waves. The model showed that internal mixing was in constant competition with tidal and surface boundary mixing, which were both based on seasonal mean values. The seasonal values did not allow for quiescent periods when diffusion by internal waves could dominate, with the constant erosion of

the thermocline by wind mixing limiting the extent of thermocline diffusion. To remove this effect the model was run using realistic wind stress and tidal variation to allow the diffusion to be recorded in the absence of this competition. This allowed the thermocline to diffuse considerably more than with the seasonal wind, but it also illuminated the problem that heat input during periods of reduced wind stress would generate new shallower thermoclines. These shallow thermoclines give the impression of a single diffuse thermocline and more critically, are also taken into account in the calculation of $\Delta\Phi$. The result of this surface heating effect was that the majority of the signal in the $\Delta\Phi$ could be reproduced running the model without any internal mixing and that the excessive signal in $\Delta\Phi$ was not due to mixing by internal waves, but was in fact a result of low wind stress combined with surface heating. This result was disappointing in terms of the potential to use $\Delta\Phi$ to quantify rates of mixing over time. However it is an important result since studies in the past have used a broad thermocline in their arguments that strong mixing is taking place in a particular region [Rippeth, 2005; Green et al., 2008] and this is not necessarily true. A single temperature profile alone cannot be used as an indication of the level of internal mixing because as the model demonstrates; a broad thermocline can be produced in a region where no internal mixing exists, and a sharp thermocline may form in regions of strong internal mixing.

While $\Delta\Phi$ has been of limited use in time series measurements, the results of its application to transects of temperature near to the shelf break show promise for providing a quantitative link between the generation and dissipation of internal waves. The issue with surface heating is reduced in these measurements for 2 reasons. Firstly the dissipation rates are an order of magnitude higher close to the shelf break than in the Western Irish Sea. Secondly the observations are quasi-synoptic so that the meteorological forcing will be approximately the same across the region and so therefore will the surface heating effect. This allows the heating artefact to be removed by subtracting the constant value for $\Delta\Phi$ far onto the shelf where internal wave activity is expected to be zero. Transects of $\Delta\Phi$ from towed CTD data showed decaying internal mixing energy with distance from the shelf break. These transects suggest that internal mixing reaches zero at a distance of 80 to 100km from the shelf break with an e-folding of internal wave energy of 50km. This compares favourably with the 42km calculated by Inall et al. [2011]using velocity and hydrography observations from the same region.

7.4 Conclusions and questions for future research

The observations presented have improved our understanding of the processes of vertical mixing in shelf seas. Inertial shear spikes have been ruled out as a source of anomalous mid-water mixing, although we do not have direct observations of the dissipation generated as they deepen the sur-

face mixed layer. Technology may be of assistance with making such observations, with turbulence packages now available for both semi-autonomous gliders and automated underwater vehicles, these platforms have the potential to provide direct evidence of turbulent dissipation by shear spikes. Internal waves, particularly high frequency waves were found to be a source of strong mid-water mixing in the Western Irish Sea. Observing these features is complicated by strong barotropic tidal currents which distort them making estimating their wavelength and direction of propagation difficult. Using a drifting mooring to track the barotropic tide is one solution put forward to this problem, however the passage of the wave itself has been shown to disturb the motion of the ship and would also affect a mooring to a lesser extent. A triangular mooring would provide the required spatial information both about the propagation and wavelength of these waves, although would take additional resources to the observations presented here. The approach of quantifying the rate of internal mixing through its effect on the temperature structure has highlighted some issues but also some potential to map the spatial distribution of internal mixing. Aims for future work would be to develop a parameterisation for the rate of internal mixing by linking $\Delta\Phi$ to the internal wave generation potential at a given location, based on proximity to topographic features and forcing currents. Such a parameterisation which improves our modelling of thermocline mixing would be greatly appreciated in the field.

Bibliography

Baines, P., 1982. On internal tide generation models. Deep Sea Research Part A. Oceanographic Research 29 (3).

Baines, P. G., 1995. Topographic Effects in Stratified Flows. Cambridge.

Baumart Z, H., Simpson, J. H., Sundermann, J., 2005. Marine Turbulence, Theories Observations and Models. Cambridge University Press.

Burchard, H., Rippeth, T. P., Apr. 2009. Generation of Bulk Shear Spikes in Shallow Stratified Tidal Seas. Journal of Physical Oceanography 39 (4), 969–985.

Chang, M.-H., Lien, R.-C., Tang, T. Y., D'Asaro, E. A., Yang, Y. J., 2006. Energy flux of nonlinear internal waves in northern South China Sea. Geophysical Research Letters 33 (3), 1–5.

Craig, P. D., 1989. A model of diurnally forced vertical current structure near 30 latitude. October 9 (11), 965–980.

Egbert, G. D., Erofeeva, S. Y., Ray, R. D., 2010. Assimilation of altimetry data for nonlinear shallow-water tides: Quarter-diurnal tides of the Northwest European Shelf. Continental Shelf Research 30 (6), 668–679.

Egbert, G. D., Ray, R. D., 2000. Significant Dissipation of Tidal Energy in the Deep Ocean Inferred from Satellite Altimeter Data. Nature 405 (1993), 775–778.

Elliott, A., 1995. A model of the annual cycle of temperature in the north-west European shelf seas with stochastic wind forcing. Estuarine, Coastal and Shelf Science, 265–280.

Emery, W., Thomson, R., 2003. Data Analysis Methods in Physical Oceanography, 2nd Edition. Elsevier.

Garrett, C., Sep. 2003. Ocean science. Enhanced: internal tides and ocean mixing. Science (New York, N.Y.) 301 (5641), 1858–9.

Garrett, C. J. R., Keeley, J. R., Greenberg, D. A., 1978. Tidal mixing versus thermal stratification in the Bay of Fundy and Gulf of Maine. AtmosphereOcean 16 (4), 403–423.

Gill, A., 1982. Atmosphereocean dynamics, volume 30 Edition. International Geophysics Series.

Grant, H., Moilliet, A., Vogel, W., 1968. Some observations of the occurrence of turbulence in and above the thermocline. Journal of Fluid Mechanics 34 (November 1962), 443–448.

Green, J. A. M., Simpson, J. H., Legg, S., Palmer, M. R., Apr. 2008. Internal waves, baroclinic energy fluxes and mixing at the European shelf edge. Continental Shelf Research 28 (7), 937–950.

Green, J. A. M., Simpson, J. H., Thorpe, S., Rippeth, T., Feb. 2010. Observations of internal tidal waves in the isolated seasonally stratified region of the western Irish Sea. Continental Shelf Research 30 (2), 214–225.

Howard, L., 1961. Note on a paper of John W. Miles. Journal of Fluid Mechanics 2 (March), 2–5.

Inall, M., Aleynik, D., Boyd, T., Palmer, M., Sharples, J., Dec. 2011. Internal tide coherence and decay over a wide shelf sea. Geophysical Research Letters 38 (23), 3–8.

Inall, M. E., Rippeth, T. P., Sherwin, T. J., 2000. Impact of nonlinear waves on the dissipation of internal tidal energy at a shelf break 105, 8687–8705.

Klein, P., Coste, B., Jan. 1984. Effects of wind-stress variability on nutrient transport into the mixed layer. Deep Sea Research Part A. Oceanographic Research Papers 31 (1), 21–37.

Klink, J., 1999. dynmodes.m - oceanic dynamical vertical modes.

Knight, P., Howarth, M., Rippeth, T., Jun. 2002. Inertial currents in the northern North sea. Journal of Sea Research 47 (3-4), 269–284.

Kunze, E., Rosenfeld, L. K., Carter, G. S., Gregg, M. C., 2002. Internal Waves in Monterey Submarine Canyon. Energy, 1890–1913.

Lueck, R. G., 2005. Horizontal and vertical turbulence profilers. In: Marine Turbulence Theories Observations and Models. Cambridge University Press, pp. 89–100.

Luyten, P., Deleersnijder, E., Ozer, J., 1996. Presentation of a family of turbulence closure models for stratified shallow water flows and preliminary application to the Rhine outflow region. Continental Shelf 16 (1), 101–130.

Mackinnon, J. A., Gregg, M. C., 2001. Mixing on the Late-Summer New England Shelf Solibores , Shear and Stratification. Applied Physics.

Mellor, G., 1975. The structure and dynamics of the ocean surface mixed layer. J. Phys. Oceanogr.

Miles, J., 1961. On the stability of heterogeneous shear flows. Journal of Fluid Mechanics, 496–508.

Morgan, P. P., 1994. SEAWATER: A library of MATLAB registered computational routines for the properties of sea water. CSIRO Marine Laboratories Report, 222.

Moum, J. N., Farmer, D. M., Smyth, W. D., Armi, L., Vagle, S., 2003. Structure and Generation of Turbulence at Interfaces Strained by Internal Solitary Waves Propagating Shoreward over the Continental Shelf. Journal of Physical Oceanography 33 (10), 2093–2112.

Munk, W., 1998. Abyssal recipes II: energetics of tidal and wind mixing. Deep-Sea Research Part I.

Osborn, T., 1980. Estimates of the local rate of vertical diffusion from dissipation measurements. J. Phys. Oceanogr.

Osborn, T. R., Crawford, W. R., 1980. An airfoil probe for measuring velocity fluctuations in water. In: Dobson, F., Hasse, L., Davis, R. (Eds.), AirSea Interactions Instruments and Methods. Plenum, pp. 369–386.

Palmer, M. R., Rippeth, T. P., Simpson, J. H., Dec. 2008. An investigation of internal mixing in a seasonally stratified shelf sea. Journal of Geophysical Research 113 (C12), 1–14.

Pawlowicz, R., Beardsley, B., Lentz, S., Oct. 2002. Classical tidal harmonic analysis including error estimates in MATLAB using T_TIDE. Computers & Geosciences 28 (8), 929–937.

Pollard, R. T., Rhines, P. B., Thompson, R. O. R. Y., 1972. The deepening of the wind-Mixed layer. Geophys Fluid Dyn 4 (1), 381–404.

Richardson, K., 2000. Subsurface phytoplankton blooms fuel pelagic production in the North Sea. Journal of Plankton Research 22 (9), 1663–1671.

Rippeth, T. P., Dec. 2005. Mixing in seasonally stratified shelf seas: a shifting paradigm. Philosophical transactions. Series A, Mathematical, physical, and engineering sciences 363 (1837), 2837–54.

Rippeth, T. P., Palmer, M. R., Simpson, J. H., Fisher, N. R., Sharples, J., 2005. Thermocline mixing in summer stratified continental shelf seas. Geophysical Research Letters 32 (5), 10–13.

Rippeth, T. P., Simpson, J. H., Player, R. J., Garcia, M., 2002. Current oscillations in the diurnal-inertial band on the Catalonian shelf in spring. Continental Shelf Research 22 (2), 247–265.

Rippeth, T. P., Wiles, P., Palmer, M. R., Sharples, J., Tweddle, J., Jun. 2009. The diapcynal nutrient flux and shear-induced diapcynal mixing in the seasonally stratified western Irish Sea. Continental Shelf Research 29 (13), 1580–1587.

Rockland Scientific International, 2013. VMP 500 - Coastal Vertical Microstructure Profiler. URL `http://www.rocklandscientific.com/Portals/0/Products/VMP500.pdf`

Sharples, J., Moore, C., 2001. Internal tide dissipation, mixing, and vertical nitrate flux at the shelf edge of NE New Zealand. Journal of geophysical 106 (2000), 69–81.

Sharples, J., Moore, C. M., Rippeth, T. P., Holligan, P. M., Hydes, D. J., Fisher, N. R., Simpson, J. H., 2001. Phytoplankton distribution and survival in the thermocline. English 46 (3), 486–496.

Sharples, J., Tweddle, J., Green, J. A. M., 2007. Spring-neap modulation of internal tide mixing and vertical nitrate fluxes at a shelf edge in summer. Limnology and Oceanography.

Sherwin, T., Feb. 1987. Inertial oscillations in the Irish Sea. Continental Shelf Research 7 (2), 191–211.

Sherwin, T., 1988. Analysis of an internal tide observed on the Malin Shelf, north of Ireland. Journal of physical oceanography.

Simpson, J. H., 1981. The shelf-sea fronts: implications of their existence and behaviour. Society.

Simpson, J. H., Allen, C. M., Morris, N. C. G., 1978. Fronts on the continental shelf. Journal of Geophysical Research 83 (C9), 4607–4614.

Simpson, J. H., Bowers, D., 1984. The role of tidal stirring in controlling the seasonal heat cycle in shelf seas. Annales geophysicae 2 (4), 411–416.

Simpson, J. H., Brown, J., Matthews, J., Allen, G., 1990. Tidal Straining, Density Currents, and Stirring in the Control of Estuarine Stratification. Estuaries 13 (2), 125–132.

Simpson, J. H., Crawford, W., 1996. The vertical structure of turbulent dissipation in shelf seas. Journal of Physical Oceanography 26, 1579–1590.

Simpson, J. H., Hughes, D. G., Morris, N. C. G., 1977. The relation of seasonal stratification to tidal mixing on the continental shelf. DeepSea Research 24, 327–340.

Simpson, J. H., Hunter, J., 1974. Fronts in the Irish sea. Nature 250, 404 – 406.

Simpson, J. H., Hyder, P., Rippeth, T. P., Lucas, I. M., 2002. Forced oscillations near the critical latitude for diurnal-inertial resonance. Journal of Physical Oceanography 32 (1), 177–187.

Simpson, J. H., Sharples, J., 2012. Introduction to the Physical and Biological Oceanography of Shelf Seas. Cambridge University Press.

Stigebrandt, A., Aure, J., 1989. Vertical mixing in basin waters of fjords. Journal of Physical Oceanography 19 (7), 917–926.

Sverdrup, H. U., 1953. On conditions for the vernal blooming of phytoplankton. ICES Journal of Marine Science 18 (3), 287–295.

Thomas, H., Bozec, Y., Elkalay, K., De Baar, H. J. W., 2004. Enhanced open ocean storage of CO2 from shelf sea pumping. Science 304 (5673), 1005–1008.

Thorpe, S. A., 2009. An Introduction to Ocean Turbulence. Book 89 (52), 547.

Townsend, D. W., Cammen, L. M., Holligan, P. M., Campbell, D. E., Pettigrew, N. R., 1994. Causes and consequences of variability in the timing of spring phytoplankton blooms. DeepSea Research Part IOceanographic Research Papers 41 (5-6), 747–765.

Tsunogai, S., Watanabe, S., Sato, T., 1999. Is there a "continental shelf pump" for the absorption of atmospheric CO2? Tellus Series B Chemical And Physical Meteorology 51 (3), 701–712.

Van Haren, H., Maas, L., Zimmerman, J. T. F., Ridderinkhof, H., Malschaert, H., 1999. Strong inertial currents and marginal internal wave stability in the central North Sea. Geophysical Research Letters 26 (19), 2993–2996.